Copyright
by
Braulio Gutiérrez-Medina
2004

The Dissertation Committee for Braulio Gutiérrez-Medina
certifies that this is the approved version of the following dissertation:

Quantum Transport and Control of Atomic Motion with Light

Committee:

Mark G. Raizen, Supervisor

Joe C. Campbell

Duane A. Dicus

Manfred Fink

Greg O. Sitz

Quantum Transport and Control of Atomic Motion with Light

by

Braulio Gutiérrez-Medina, B.S.

DISSERTATION

Presented to the Faculty of the Graduate School of

The University of Texas at Austin

in Partial Fulfillment

of the Requirements

for the Degree of

DOCTOR OF PHILOSOPHY

THE UNIVERSITY OF TEXAS AT AUSTIN

August 2004

To my family

§

Dicen que en el riñón de Andalucía hubo una escuela de médicos. El maestro preguntaba:

-¿Qué hay con este enfermo, Pepillo?

-Para mí –respondía el discípulo– que se trae una cefalalgia entre pecho y espalda que lo tiene frito.

-¿Y por qué lo dices, salado?

-Señor maestro: porque me sale del alma.

Alfonso Reyes

Acknowledgments

I would like to thank my advisor Mark Raizen, for giving me the opportunity to work in such an exceptional lab. Mark is an extraordinary physicist always developing new ideas, which he shares with his students with contagious enthusiasm. It has been an invaluable learning experience working together with him over the past six years.

When I joined the lab in the summer of 1998, I started working with Martin Fischer. Since then, until he graduated, I never stopped asking him questions, which he answered always with patience and an effort to make things clear. It was him who introduced me into the complexities and secrets of top experimental physics. Most importantly, he offered his friendship. The latter is an element absolutely necessary to enjoy our daily activities, and I am very happy to have counted on him for that. Together, we worked on the experiments of references [1, 2].

In early 2001, Kevin Henderson arrived in the lab to join the sodium experiment. The Zeno and Anti-Zeno studies had just concluded, and we decided to start working on a new vacuum chamber, designed to produce a Bose-Einstein condensate. From the beginning of this enterprise, Kevin has worked enormously towards its success. He has an amazing source of energy, and an invariable willingness to help, which I truly appreciate. The organization Kevin has implemented in the lab has helped us to become more efficient.

The newest member of the sodium team is Hrishikesh Kelkar, who started working with us in the summer of 2003. Hrishi has proved to be a valuable addition to the lab, and I have enjoyed discussions with him over a large number of subjects, ranging from hidden variable theories to the physical and culinary properties of turmeric. With Kevin and Hrishi working together, the experiment will be in good hands.

Our postdoc Florian Schreck has provided essential contributions to the experiment. Florian has been focused mainly on the rubidium BEC efforts, where he has developed a very generic software program that controls the timing of our experiments. Florian is always full of ideas and is ready to help whenever needed. I have learned a lot from him, and enjoyed his friendship as well.

Several other students have helped in the advancement of the experiment. Artëm Dudarev worked with Martin and me on the recoil-induced resonances studies and later made significant contributions during the early stages of the BEC apparatus. Master's student Artur Widera designed and constructed our Zeeman slower. Robert Morgan worked in the construction of the cloverleaf magnetic trap. Finally, undergraduate students Patrick Bloom and Greg Henry implemented a number of necessary small projects.

I have enjoyed over the years the atmosphere of friendship existing in our lab, developed with the workers of the *other* experiment. The previous generation of students in the cesium setup included Dan Steck and Windell Oskay, and our former postdoc Valery Milner. More recently, I have shared the pains and magnificence of transforming a simple MOT experiment into a BEC machine with fellow graduate students Jay Hanssen, Todd Meyrath, and

Chih-sung Chuu; all of them good friends. In particular, I would like to thank Todd for providing help with a number of electronics projects. Using their computational and electronics expertise, Todd and Florian have developed tools which the lab as a whole has benefitted from.

I would like to thank several people that helped me in one way or another during my stay in the Physics Department: the CNLD group; the personnel of the machine shop and cryo-lab, in particular, Allan Schroeder and Jack Clifford; the administrative staff on the fifth floor: Glenn Suchan, Olga Vorloou, and Dorothy Walker; former graduate coordinator Norma Kotz; the CNLD administrative staff: Rosamaria Tovar, Olga Vera, and Elena Simmons.

I was fortunate to meet many good friends among fellow physics students, with whom I enjoyed miraculous days of soccer every Friday afternoon. Also, it is always nice to find people sharing the same circumstance of studying abroad, and I was happy to find a small Mexican crew within RLM: Eva, Francisco, Nacho, and Ramón.

There is a life outside physics, and so I went to meet her. I rejoiced taking a few literature courses at the Spanish and Portuguese Department, where I met several friends. I want to thank Professor Enrique Fierro, from whom I have learned a lot and was generous enough to offer a poetry workshop during the spring of 2002. Shortly after I came to Austin, I made one of the best decisions ever, which was to take dance lessons. I would like to thank the friends at the UT Ballroom Dance Club; it has been a lot of fun.

I want to thank two very special physicists and friends, both gifted human beings: Luis Orozco and Kirk Madison. Luis has helped me constantly since I met him in the summer of 1996, when I visited his lab. Kirk has been

a comrade with whom I enjoyed playing soccer or discussing physics. I have learned much from both, from their compassionate attitude towards life.

I would like to thank Jay Hanssen, Kevin Henderson, Hrishikesh Kelkar, Todd Meyrath, Florian Schreck, and Greg Sitz for valuable comments and corrections that have helped improve this dissertation.

I want to acknowledge financial support from a Mexican Center Fellowship, UT Austin, during the academic year 2001-2002.

Finally, I would like to thank all the friends and family in Mexico that supported me during these years. Thank you.

Quantum Transport and Control of Atomic Motion with Light

Publication No. _____

Braulio Gutiérrez-Medina, Ph.D.
The University of Texas at Austin, 2004

Supervisor: Mark G. Raizen

This dissertation describes our experimental investigations of quantum transport and atomic motion control using optical potentials. The system we study consists of ultracold sodium atoms under the influence of light forces.

First, we introduce the dynamics of neutral atoms in a periodic optical potential. The system resembles the textbook problem of an electron inside the crystalline lattice, and we review the main characteristics of the interaction for the atom optics case. In particular, atoms trapped in a lattice subject to large accelerations undergo Landau-Zener tunneling, process which makes the system unstable. The number of atoms trapped in the potential shows the characteristic exponential decay over time. However, deviations from this law are predicted by quantum mechanics. We use the experimental access to the non-exponential time to demonstrate the Quantum Zeno and Anti-Zeno effects. These effects show the influence of frequent observations on the decay rate of a quantum unstable system.

The second part of the dissertation introduces a new system we plan to study, namely, the quantum interaction between sodium atoms in the ground

state and a conductive surface. We are interested in the measurement of the Casimir-Polder potential with a precision of better than 1%. In order to do this, we have chosen to launch the atoms towards the surfaces at very small incident velocities (a few mm/s), and measure the influence of the interaction on the reflection probability. Atoms reflect from the purely attractive potential due to quantum reflection, an effect with no classical analogy.

The experimental observation of quantum reflection requires atomic distributions with temperatures below 1 μK. For this purpose, we have produced and studied a Bose-Einstein condensate (BEC) with sodium atoms. The region where the BEC is created is separated spatially form the surfaces by a distance of 10 cm, vertically. In order to bring the atoms close to the surfaces prior to their launching, we have developed an optical elevator. The elevator uses a moving optical lattice in the regime where tunneling is negligible. Results of the macroscopic optical transport technique, and current progress towards a measurement of the Casimir-Polder interaction, are reported.

Table of Contents

Acknowledgments **v**

Abstract **ix**

List of Tables **xv**

List of Figures **xvi**

Chapter 1. Quantum Transport **1**

1.1 Introduction 2

1.1.1 Light forces 2

1.1.2 Atoms in an optical lattice 4

1.1.3 Scattering rate 6

1.2 Quantum dynamics of atoms in an optical lattice 7

1.2.1 Band structure 7

1.2.2 An accelerating lattice 9

1.2.3 Bloch oscillations 12

1.2.4 Landau-Zener tunneling 14

1.2.5 Non-exponential decay 17

1.3 The Zeno and Anti-Zeno effects 19

Chapter 2. Experimental techniques I **22**

2.1 Laser cooling 22

2.1.1 The use of two level atom theory 23

2.1.2 Transversal heating 24

2.1.3 Optical molasses 24

2.1.4 The magneto-optical trap 26

2.2 The earlier sodium experiment 28

2.2.1 The laser system 28

2.2.2 Vacuum chamber 30

2.3 Observation of the Quantum Zeno and Anti-Zeno effects 31

2.3.1 The optical lattice 31

2.3.2 Experimental sequence 33
2.3.3 The Zeno and Anti-Zeno effects: results 34
2.4 Properties and limitations of cooling and transport methods using near resonance light 46
2.4.1 The Type II MOT 47
2.4.2 Lattice cooling 49
2.5 A double MOT system in the new chamber 54
2.5.1 Magnetic launch 55
2.5.2 Continuous and pulsed resonant push 58
2.5.3 On why double MOT systems work better with rubidium than sodium 58
2.5.4 The lattice launch method 59

Chapter 3. The Casimir-Polder problem 63
3.1 The atom-atom van der Waals forces 63
3.2 The atom-wall potential. Semiclassical picture 70
3.3 The Casimir-Polder potential 73
3.4 A review of experimental progress 77
3.4.1 Hydrogen on helium 77
3.4.2 The Yale experiment 78
3.4.3 Cold atoms on a prism 79
3.4.4 Shimizu's experiment 81
3.4.5 Recent developments 82
3.5 Quantum Reflection 84
3.5.1 The reflection effect 85
3.6 Calculation of the reflection probability 86
3.6.1 The method 87
3.6.2 Solution in the van der Waals limit 89
3.6.3 Solution for the Casimir-Polder potential 94
3.6.4 An experimental concern 98

Chapter 4. Experimental techniques II 100
4.1 A new experimental system 100
4.2 The oven 101
4.2.1 The design 102
4.2.2 Vacuum considerations 106

4.2.3 Operation of the oven chamber . . . 107
4.2.4 Final numbers . . . 109
4.3 The Zeeman slower . . . 110
4.3.1 Spin-Flip slower . . . 112
4.3.2 The design . . . 113
4.3.3 Construction . . . 117
4.3.4 Results . . . 119
4.3.5 Addendum. 2D Molasses . . . 124
4.4 The main chamber . . . 126
4.5 Bakeout . . . 133
4.6 The laser system . . . 135
4.7 The Magneto Optical Trap . . . 136
4.7.1 The dark spot MOT . . . 136
4.7.2 Compressed MOT and Polarization Gradient Cooling . . 138
4.8 Magnetic Trapping . . . 139
4.8.1 Introduction . . . 139
4.8.2 Principles . . . 139
4.8.3 The Ioffe-Pritchard trap . . . 142
4.8.4 Adiabatic following . . . 144
4.8.5 The cloverleaf coil . . . 144
4.8.6 Design and construction . . . 149
4.8.7 Connections and cooling . . . 152
4.8.8 Control electronics . . . 155
4.9 The transfer of atoms to the magnetic trap . . . 159
4.10 Evaporative cooling . . . 160
4.10.1 RF evaporation . . . 162
4.10.2 Gravitational sag . . . 166

Chapter 5. Bose-Einstein condensation of sodium 168
5.1 A brief introduction to Bose-Einstein condensation . . . 168
5.2 Absorption Imaging . . . 170
5.3 Computer control system . . . 172
5.4 A summary of the experimental sequence . . . 174
5.5 Characterization of the magnetic trap and BEC . . . 179
5.5.1 Frequency . . . 179
5.5.2 The Bose distribution . . . 181

5.5.3 The BEC distribution 184
5.5.4 Adiabatic decompression 186
5.5.5 An interesting effect 188

Chapter 6. An optical elevator for ultracold atoms 192
6.1 Introduction 192
6.2 The dipole force revisited 192
6.3 Optical potentials: A single focused beam 194
6.4 Optical potentials: A moving lattice 196
6.5 The atomic elevator and its experimental implementation . . . 197
6.5.1 A 'stationary' lattice 199
6.5.2 Loading 202
6.5.3 Bloch oscillations in the vertical lattice 203
6.5.4 The moving lattice 207
6.5.5 Results 209
6.6 Towards a measurement of the Casimir-Polder interaction . . . 210

Bibliography 214

Vita 236

List of Tables

4.1 Summary of properties for the magnetic trap coils 154

5.1 Currents in the magnetic trap coils during transfer and evaporation 176

List of Figures

1.1 Band structure for neutral atoms in a stationary optical lattice 10
1.2 Schematic of Bloch oscillations and tunneling, illustrated within the repeated-zone scheme 15

2.1 Term diagram for the D2 line of sodium 27
2.2 Laser setup 29
2.3 Experimental setup for the accelerating optical lattice 32
2.4 A schematic of the experimental sequence followed in the quantum transport experiments 35
2.5 A picture of the detected atomic distribution after a tunneling sequence 36
2.6 The acceleration sequence during a simple tunneling experiment 38
2.7 The acceleration sequence used for the observation of the Zeno, and Anti-Zeno effects 39
2.8 Probability of survival in the accelerated potential as a function of duration of the tunneling acceleration. Observation of the Zeno effect. 42
2.9 Survival probability as a function of the tunneling acceleration time for the Anti-Zeno case. 44
2.10 Evolution of the Anti-Zeno effect as a function of the interruption time 45
2.11 Type I and Type II MOT frequency detuning 48
2.12 The lattice launch method 61

3.1 Interaction of the instantaneous atomic dipole with a metallic wall 70
3.2 Change of the de Broglie wavelength as an incident particle travels along the potential 91
3.3 Real and imaginary parts of the incident wavefunction 92
3.4 The evolution of the WKB reflection probability 93
3.5 Results of the fit to the calculated QED potential between a sodium atom and a metallic wall 96
3.6 The reflection probability for sodium atoms on a metallic surface as a function of incident velocity 97

4.1 A drawing of the effusive oven 104
4.2 The evolution of the atomic spin in a spin-flip Zeeman slower . 114
4.3 A picture of the a Zeeman slower coil assembly 118
4.4 The field of the spin-flip Zeeman slower 122
4.5 The evolution of the atomic velocity in the Zeeman slower . . 124
4.6 A schematic view of the main vacuum chamber 127
4.7 A schematic view of the full chamber assembled 132
4.8 Bakeout of the main chamber 134
4.9 Origin of the quadrupole field created by the cloverleaf coils . 147
4.10 Arrangement of coils for the cloverleaf magnetic trap 148
4.11 A schematic of the electrical circuit used for the magnetic trap coils 157
4.12 A contour plot for the magnitude of the trap magnetic field . . 159
4.13 The dressed-picture of the potential experienced by a sodium atom in a magnetic trap under the presence of a rf field 165

5.1 Formation of a Bose-Einstein condensate 177
5.2 Lineshape of the density distribution during the formation of a Bose-Einstein condensate 178
5.3 Measurement of the magnetic trap radial frequency 180
5.4 Fit to the atomic density distribution using Gauss and Bose functions 183
5.5 Relevant data points for the Gauss and Bose fits to the atomic distribution after time of flight 184
5.6 Topological effects in the decompressed BEC 189

6.1 A schematic of the setup used for the optical elevator 201
6.2 Bloch oscillations in a vertical standing wave 204
6.3 A pulsed atom laser resulting from tunneling during Bloch oscillations 206
6.4 The elastic collision of two coherent atomic clouds 206
6.5 Timing of atomic motion as the motorized slide moves 209
6.6 Transported atoms by the optical elevator 211

Chapter 1

Quantum Transport

The mechanical action of light on atoms constitutes the basis of powerful methods and tools developed in recent years to control atomic motion. The classical theory of electromagnetism, in the form given by Maxwell, assigns a well defined momentum to radiation[1]. Early quantum mechanics introduced the concept of photons, and in 1933 Frisch observed the recoil of atoms as they scattered resonant light. Today, light forces (coherent and incoherent) are used routinely to trap and cool atoms to the point of quantum degeneracy. The field of Atom Optics uses basic systems involving ultracold atoms and laser light to study paradigmatic problems in the fields of solid state, nonlinear dynamics, and condensed matter physics in general. In particular, the study of atomic motion in optical lattices offers a unique testing ground for quantum transport in periodic potentials.

[1] In his *Treatise of Electricity and Magnetism* [3], Maxwell writes:

> A flat body exposed to sunlight would experience this pressure on its illuminated side only, and would therefore be repelled from the side on which the light falls. It is probable that a much greater energy of radiation may be obtained by the concentrated rays of the electric lamp. Such rays falling on a thin metallic disk, delicately suspended in a vacuum, might perhaps produce a mechanical effect.

This is of course the problem of the radiometer, a subject of great interest for him.

We divide this thesis in two parts. The first one introduces the physics of cold atoms in an optical lattice, and culminates with the observation of the Quantum Zeno and Anti-Zeno effects in an unstable system. The second part develops further experimental atom optics tools, aimed at the study of interactions between atoms and surfaces (Casimir-Polder potential). In particular, we present the obtainment of a Bose-Einstein condensate in sodium, and the implementation of an 'optical elevator' to transport sub-recoil atoms over distances of 10 cm using a moving optical lattice. The division between the two sections is natural, as for in the quantum transport experiments we used atoms with temperatures of 85 μK, while the atom-surface studies require sub-recoil atoms, with temperatures below 1 μK.

1.1 Introduction

1.1.1 Light forces

We begin by discussing absorptive and dispersive forces on an atom due to its interaction with laser light of frequency $\omega_{\rm L}$ and wavevector $k_{\rm L}$ [4]. The Hamiltonian for a two-level atom in the presence of an electric field $\mathbf{E}(\mathbf{R})$ is:

$$H = \hbar\omega_0|{\rm e}\rangle\langle{\rm e}| + \frac{\mathbf{p}^2}{2M} - \mathbf{d}\cdot\mathbf{E}(\mathbf{R}), \tag{1.1}$$

where $\mathbf{p}$ is the atomic center of mass momentum, and $\mathbf{d}$ the atomic dipole moment. The frequency ω_0 corresponds to the resonance between levels $|{\rm g}\rangle$ and $|{\rm e}\rangle$. The atomic momentum follows the Heisenberg equation of motion:

$$\begin{aligned}\dot{\mathbf{p}} &= \frac{i}{\hbar}[H,\mathbf{p}] = \frac{i}{\hbar}[H,\mathbf{p}] \\ &= \mathbf{d}\cdot\nabla\mathbf{E}(\mathbf{R}).\end{aligned} \tag{1.2}$$

In the semiclassical approximation the dipole moment operator can be replaced by its average value $\langle \mathbf{d} \rangle$, and the electric field is considered classical. Assuming a linear polarization along $\hat{\epsilon}$, we have:

$$\begin{aligned} \mathbf{E} &= \mathrm{Re}[\mathrm{E}_0(\mathbf{R}) \exp\{\mathrm{i}(\omega_\mathrm{L}\mathrm{t} + \phi(\mathbf{R}))\}]\hat{\epsilon}, \quad \text{and} \qquad (1.3) \\ \langle \mathbf{d} \rangle &= \mathrm{Re}[\alpha \mathrm{E}_0(\mathbf{R}) \exp\{\mathrm{i}(\omega_\mathrm{L}\mathrm{t} + \phi(\mathbf{R}))\}]\hat{\epsilon}, \qquad (1.4) \end{aligned}$$

where $\alpha = \alpha' + i\alpha''$ is the complex atomic polarizability, and the field amplitude E_0 is real. After substitution into Eq. (1.2), the time averaged values are

$$\dot{\mathbf{p}} = \mathbf{F}_{\mathrm{dip}} + \mathbf{F}_{\mathrm{sp}}, \qquad (1.5)$$

where

$$\begin{aligned} \mathbf{F}_{\mathrm{dip}} &= \frac{1}{4}\alpha' \nabla E_0^2, \quad \text{and} \\ \mathbf{F}_{\mathrm{sp}} &= \frac{1}{2}\alpha'' E_0^2 \nabla \phi(\mathbf{R}). \qquad (1.6) \end{aligned}$$

The first term corresponds to the in-phase, dispersive part of the atomic dipole, and is called the *dipole force*. The second comes from the 90^o out of phase, absorptive part of the dipole, and it is termed the *spontaneous force*.

This simple derivation of the light forces on an atom provide an excellent insight for the understanding of their origin and dependance. We note the form of the complex polarizability, as a function of laser detuning $\Delta_\mathrm{L} = \omega_\mathrm{L} - \omega_0$, the atomic velocity $\mathbf{v}$, and the expectation value of the atomic dipole moment projected along the electric field $d_{\mathrm{eg}} = |\langle \mathrm{e}|e\mathbf{r} \cdot \hat{\epsilon}|\mathrm{g}\rangle|$:

$$\alpha = \frac{d_{\mathrm{eg}}^2}{\hbar} \frac{(\Delta_\mathrm{L} - \mathbf{k} \cdot \mathbf{v}) - i(\Gamma/2)}{(\Delta_\mathrm{L} - \mathbf{k} \cdot \mathbf{v})^2 + ((\Gamma/2)^2 + \Omega^2/2)}, \qquad (1.7)$$

where Γ is the natural linewidth of the excited state, and $\Omega = d_{\rm eg}E_0/\hbar$ the Rabi frequency. In the limit of large detuning, the forces behave like

$$\begin{aligned} \mathbf{F}_{\rm dip} &\propto \frac{\nabla I(\mathbf{R})}{\Delta_{\rm L}}, \quad \text{and} \\ \mathbf{F}_{\rm sp} &\propto \frac{I(\mathbf{R})}{\Delta_{\rm L}^2}. \end{aligned} \tag{1.8}$$

It is immediately recognized that the dipole force can be used to construct atom traps which are (for large enough detunings) conservative. On the other hand, the spontaneous force is extremely useful in the cooling of atoms from a thermal gas. As we will see shortly, absorptive forces enable us to cool and trap atoms, while dispersive forces are used to manipulate them.

1.1.2 Atoms in an optical lattice

Consider the electric field of two counter-propagating beams along the x direction of wave numbers $k_{1,2} = 2\pi/\lambda_{1,2}$ and possessing field amplitudes $E_{1,2}$

$$\mathbf{E}(x,t) = \hat{\epsilon}[E_1\cos(\omega_1 t + k_1 x) + E_2\cos(\omega_2 t - k_2 x)]. \tag{1.9}$$

In general, the two beams will have a difference in their frequencies of $\delta = \omega_2 - \omega_1$. The simple reasoning of last section cannot be followed here, as the total field cannot be cast in the form of Eq. (1.3). A rigorous analysis can be done by considering the Bloch equations under adiabatic elimination of the excited state [5, 6]. In the large detuning from resonance limit, the result for the potential is:

$$V(x) = V_0\cos(2k_{\rm L}x - \delta t), \tag{1.10}$$

where $k_{\rm L}$ is the average wave number. This derivation neglects the beam divergence, and assumes that the typical size of the atomic cloud is much

less than the typical beam waist w_0; conditions valid in our experiment. The potential amplitude is given by

$$V_0 = \frac{E_1 E_2 d^2}{2\hbar\Delta_{\rm L}} = \frac{\Omega_1\Omega_2}{2\Delta_{\rm L}}. \tag{1.11}$$

The Rabi frequency was used in the last step, and is defined in terms of the electric field and the dipole moment as

$$\Omega = \frac{\mathbf{d}\cdot\mathbf{E}_0}{\hbar}. \tag{1.12}$$

The potential thus formed is a standing wave when the frequency of the beams is the same. The period in this configuration is equal to $\lambda_{\rm L}/2$. In the more general case when the wave vectors of the two interfering beams make an angle θ, the period is equal to

$$a = \frac{\lambda_{\rm L}}{2\sin(\theta/2)}. \tag{1.13}$$

When the frequency difference δ is not zero, the wave will be traveling (respect to the lab frame) at a speed

$$v = \frac{\lambda_{\rm L}}{2}\frac{\delta}{2\pi}. \tag{1.14}$$

The assumption of a two-level atom is not correct in general. However, in the case of the alkalis it is an excellent approximation, as the atom can be prepared in a well defined hyperfine ground state by optical pumping. Since the excitation to upper states is negligible in far detuned light, the dynamics is determined solely by the ground state amplitude.

In order to obtain an expression for the potential amplitude in terms of measurable quantities, we consider the relationship between electric field and

power in a gaussian beam. The intensity of a beam is related to its electric field amplitude by the relation

$$I_0 = \frac{1}{2} c\epsilon_0 E^2. \tag{1.15}$$

In turn, the integrated power in a gaussian beam is related to the peak intensity by

$$P = 2\pi \int_0^\infty I_0 e^{-2r^2/w^2} r dr = \frac{\pi w_0^2}{2} I_0. \tag{1.16}$$

In the case of the sodium D2 line the effective dipole moment in SI units is [6]

$$d_{\text{eff}} = \sqrt{\frac{\epsilon_0 \hbar \lambda_{\text{L}}^3}{4\pi^2 \tau}} = 1.71 \times 10^{-29}\,\text{Cm}, \tag{1.17}$$

where $\tau = 16.237(35)$ ns is the radiative lifetime of the $3p\,^2P_{3/2}$ state [7, 8]. A substitution of Eqs. (1.15), (1.16), and (1.17) in (1.11) provides us with an useful expression for the potential amplitude in terms of power and waist of the beams, and the detuning from resonance

$$V_0 = \frac{4c^2}{\tau \omega_0^3} \frac{\sqrt{P_1 P_2}}{w_1 w_2 \Delta_{\text{L}}}. \tag{1.18}$$

1.1.3 Scattering rate

The main source of decoherence in quantum transport experiments is the spontaneous scattering of photons. The scattering rate will depend on the frequency, polarization, and direction of propagation (with respect to an external reference magnetic field) of the involved light source. From the optical Bloch equations [9], the rate is:

$$R_{\text{sc}} = \frac{\Gamma}{2} \frac{S_0}{(1 + S_0 + 4(\Delta_{\text{L}}/\Gamma)^2)}, \tag{1.19}$$

where the *saturation parameter* is given by

$$S_0 = \frac{I}{I_{\text{s}}} = 2\left(\frac{\Omega}{\Gamma}\right)^2, \tag{1.20}$$

and the saturation intensity is

$$I_{\rm s} = \frac{c\epsilon_0\Gamma^2\hbar^2}{4{d^2}_{\rm eff}}. \tag{1.21}$$

In the case of linearly polarized light in the far detuning limit, Eq. (1.17) is valid. Substitution in the last equation yields

$$I_{\rm s} = \frac{\pi\hbar c\Gamma}{\lambda^3} = 9.39\,{\rm mW/cm^2}. \tag{1.22}$$

It is convenient to leave the scattering rate in terms of the Rabi frequency. In the limit of large detuning ($\Delta_{\rm L} \gg \Gamma$),

$$R_{\rm sc} \simeq \frac{\Gamma}{4}\left(\frac{\Omega}{\Delta_{\rm L}}\right)^2. \tag{1.23}$$

Using Eq. (1.11) for the case of two beams with equal intensity, we express R_{sc} in terms of the potential amplitude V_0:

$$R_{\rm sc} \simeq \frac{\pi\Gamma}{\Delta_{\rm L}}\frac{V_0}{h}. \tag{1.24}$$

In our quantum transport experiments typical parameters used are V_0/h=80 kHz and $\Delta_{\rm L} = 2\pi\,40$ GHz = 4000 Γ. This gives a scattering rate of 60 Hz, or one scattered photon every 17 ms. In contrast, the relevant interaction time of atoms in an accelerating lattice is at most 100 μs. Fewer than 1% of the atoms scatter a photon during the experiment.

1.2 Quantum dynamics of atoms in an optical lattice

1.2.1 Band structure

We begin by considering an atom in a stationary lattice. According to Eq. (1.10), the Hamiltonian for this problem is

$$H = \frac{p^2}{2M} + V_0\cos(2k_{\rm L}x). \tag{1.25}$$

The form is a textbook example for electrons moving in the spatially periodic potential provided by a crystal lattice, that results in a band structure energy spectrum [10]. This connection imparts an extraordinary importance for the system of a neutral atom in an optical lattice [11]. Effects from solid state physics that had been difficult to observe in real solids have been experimentally realized using optical lattices, such as Bloch oscillations [12] and Wannier-Stark ladders [13]. The atom optics system offers enormous advantages because the light induced potential is free of defects or impurities, and its strength can be easily varied. Also, the relevant time scales are orders of magnitude longer, and are well within experimental reach. In this section we review some of the most important properties of a particle in a periodic potential.

The quantum mechanical treatment of a particle moving in a periodic potential is based on a very general statement known as Bloch's theorem, which reflects a symmetry of the problem. The theorem states that if the potential is periodic with period d, then the wave function ψ that solves the time-independent Schrödinger equation, can be written as a plane wave times a function with the same periodicity as the potential:

$$\psi(x) = e^{ikx} u_{n,k}(x), \tag{1.26}$$

where $u_{n,k}(x+d) = u_{n,k}(x)$. Such wave function is called a Bloch state. The quantity k is a quantum number called the quasimomentum, and is restricted to the interval $[-\pi/d, \pi/d]$. We have assumed the framework of the reduced-zone scheme, within the first Brillouin zone [10, 14, 15]. The other quantum number is n, the band index. For an optical lattice in the counter-propagating beams configuration, the width of the first Brillouin zone is equal to $2k_{\mathrm{L}}$. We

must note that it is possible to work in the repeated-zone picture as well, when the band index is retained, but the quasimomentum is allowed to range over all reciprocal space. An illustration of this point of view is found in Fig. 1.2.

The eigenvalues for the energies can be found by reducing the Schrödinger equation to Mathieu's equation, for which solutions can be found in most handbooks of mathematical functions [16]. A plot for the energy bands of potential in Eq. (1.25) is shown in Fig. 1.1. For reference, in the same plot the potential depth was included. We use the term 'well depth' to refer to the quantity $2V_0$, that is, the energy height of individual wells of the lattice. On the contrary, the 'potential amplitude' is used for V_0. From the band structure we observe that energy gaps between bands decrease very rapidly as the energy increases. This fact will be very important when we discuss our application of an accelerated lattice to construct an unstable system. We should note that for very large well depths the energy levels flatten out and become equally spaced, in similarity to the harmonic oscillator. We will return to this point when we discuss lattice cooling in Section 2.4.2.

1.2.2 An accelerating lattice

The success of condensed matter physics in understanding the electrical properties of solids has its origin in ideas developed to explain the dynamics of electrons in the lattice potential under the influence of external magnetic or electric fields [14]. The study of an atom moving in an accelerated optical lattice contributes to this understanding, because the system mimics a crystal electron with an electric field present.

We begin by considering the Hamiltonian corresponding to an atom

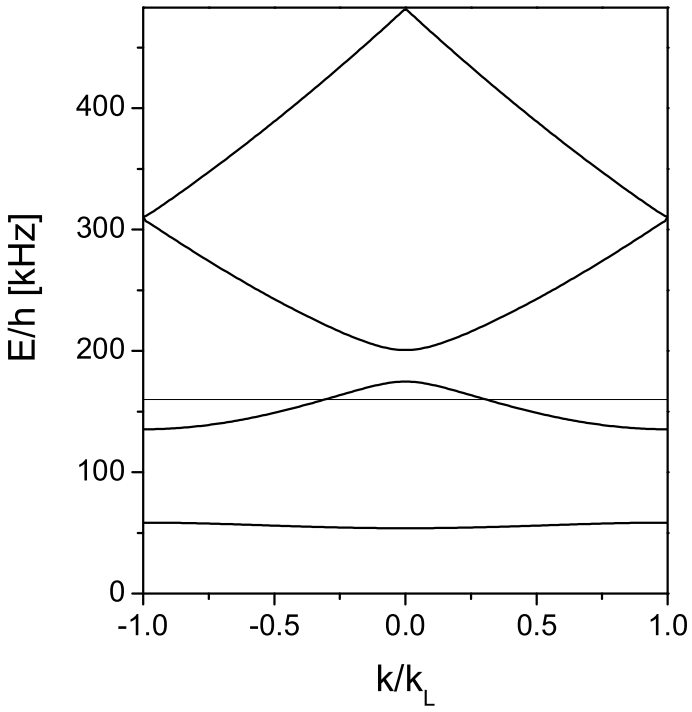

Figure 1.1: Band structure for the potential of Eq. (1.25), illustrated within the reduced-zone scheme. Thick lines correspond to the energy bands, while the thin horizontal line marks the energy well depth ($2V_0$). The width of the first Brillouin zone is equal to $2k_{\mathrm{L}}$. For this plot $V_0/h = 80$ kHz.

inside the potential of Eq. (1.10),

$$H = \frac{p^2}{2M} + V_0 \cos(2k_{\mathrm{L}}x - \delta(t)t), \tag{1.27}$$

where we have allowed for a time-dependent frequency difference of the counter-propagating beams. A constant acceleration can be imposed on the lattice if $\delta(t) = k_{\mathrm{L}}at$, where a is the acceleration. The Hamiltonian is then

$$H = \frac{p^2}{2M} + V_0 \cos\left[2k_{\mathrm{L}}\left(x - \frac{1}{2}at^2\right)\right]. \tag{1.28}$$

The connection to the solid state system can be made by applying a unitary transformation to the accelerated frame of reference [17]. The unitary transformation performs a translation of the position, momentum, and overall energy:

$$U(t) = e^{i\alpha(t)p/\hbar}e^{-i\beta(t)x/\hbar}e^{i\gamma(t)/\hbar}. \tag{1.29}$$

For a time dependent unitary transform the Hamiltonian will be transformed as

$$\tilde{H} = UHU^{\dagger} + i\hbar\frac{\partial U}{\partial t}U^{\dagger}. \tag{1.30}$$

A transformation to the accelerating frame is achieved by choosing

$$\alpha(t) = \frac{1}{2}at^2 \tag{1.31}$$

$$\beta(t) = Mat \tag{1.32}$$

$$\dot{\gamma}(t) = \frac{\beta^2}{2M} + \dot{\beta}\alpha. \tag{1.33}$$

Applying this transformation yields

$$\tilde{H} = \frac{p^2}{2M} + V_0 \cos(2k_{\mathrm{L}}x) + Ma\,x. \tag{1.34}$$

The last term containing the mass M of the atom is an inertial term, resulting from the transformation to an accelerating frame of reference. It has a correspondence with the interaction potential between an electric field $\mathcal{E}$ and the electron

$$U_{el} = \mathcal{E} e\, x, \tag{1.35}$$

where e is the electric charge of the electron.

1.2.3 Bloch oscillations

The dynamics rules for electrons in periodic solids can be applied to the accelerated lattice system. These rules are the semiclassical equations of motion, which we now state without proof [10, 14]. The equations express the relationship of the state's quasimomentum (k), band index (n), energy ($E_n(k)$), and mean velocity ($v_n(k)$):

1. The band index n is a constant of motion.

2. The evolution of the system is described by

$$v_n(k) = \frac{1}{\hbar}\frac{\partial E_n(k)}{\partial k} \tag{1.36}$$

$$\dot{k}_n(t) = -\frac{1}{\hbar} M a. \tag{1.37}$$

3. The form of the band structure $E_{n,k}$ is unchanged.

The validity of these laws is limited to weak external forces. In the case of a solid system, its application gives rise to the striking prediction that a static electric field induces an oscillatory motion of the electrons in space, rather than uniformly accelerate them. The result is found by a simple integration

of Eq. (1.37):

$$k(t) = k_0 - \frac{Mat}{\hbar}. \tag{1.38}$$

The quasimomentum grows without bounds in the extended zone scheme. However, in the reduced zone point of view, the quasimomentum increases until it reaches the edge of the Brillouin zone, at which point the motion continues from the other side in the same band. The velocity of the particle will oscillate around zero, as a consequence of Eq. (1.36), as the quasimomentum evolves linearly in time. This oscillatory motion is known as *Bloch oscillations*, and they were observed for the first time using cesium atoms in an accelerating lattice [12].

The time it takes for the quasimomentum to transverse the Brillouin zone is called the Bloch period. It is equal to

$$\tau_{\mathrm{B}} = \frac{2\hbar k_{\mathrm{L}}}{Ma} \tag{1.39}$$

Also, the amplitude of the oscillations in position space is given by $\Delta_n/(2Ma)$, where Δ_n is the width of the n^{th} energy band on which the atom moves [12].

It is important to note that for strong electric fields in the case of a crystal electron, and for strong accelerations of the atom in an optical lattice, the band index will change. This constitutes interband transitions, a subject playing a central role in the preparation of an unstable system, as we will show shortly. To have an idea of the magnitude of accelerations necessary to induce transitions to higher bands, we consider the fact that the probability for this to happen is highest when the quasimomentum k reaches the edges of the Brillouin zone, where the band gap is minimum. A criterion for the

adiabatic following of the band at $k = \pm k_{\rm L}$ is given by Dahan et. al. [12],

$$|Ma\lambda_{\rm L}/2| \ll (\pi/2)V_0^2/E_{\rm r}, \tag{1.40}$$

where $E_{\rm r} = h\,25.002$ kHz is the recoil energy of the sodium atom. Using this criterion, the critical acceleration for interband transitions is

$$a_{\rm c,ad} \simeq \pi \frac{(V_0/h)^2}{E_r/h} v_{\rm r} \tag{1.41}$$

where $v_{\rm r} = 2.946$ cm/s is the recoil velocity. We have made the approximation $\lambda_{\rm L} = \lambda_0$. Typical well depths used in our experiments have $V_0/h = 80$ kHz, which gives $a_{\rm c,ad} \simeq 24 \times 10^3$ m/s^2. We have performed experiments well below and in this limit. Accelerations of several thousands of meters per second squared were used to create the unstable system to observe non-exponential decay and the quantum Zeno and Anti-Zeno effects. On the other hand, we have observed Bloch oscillations using much colder atomic samples, with an acceleration of 9.81 m/s^2 (Chapter 6).

1.2.4 Landau-Zener tunneling

We are interested in the problem of a particle subject to the Hamiltonian of Eq. (1.34), in the limit where the inertial term is large. Classically, the particle ceases to be confined by the accelerated lattice when the following condition is met

$$\frac{dV(x)}{dx} = -2k_{\rm L}V_0 \sin(2k_{\rm L}x) - Ma = 0. \tag{1.42}$$

The local potential minima disappear for the acceleration

$$a_{\rm c,class} = \frac{2k_{\rm L}V_0}{M} = 4\pi v_{\rm r}\frac{V_0}{h}. \tag{1.43}$$

Using again our typical value of $V_0/h = 80$ kHz, we obtain $a_{\rm c,class} \simeq 30 \times 10^3$ m/s^2.

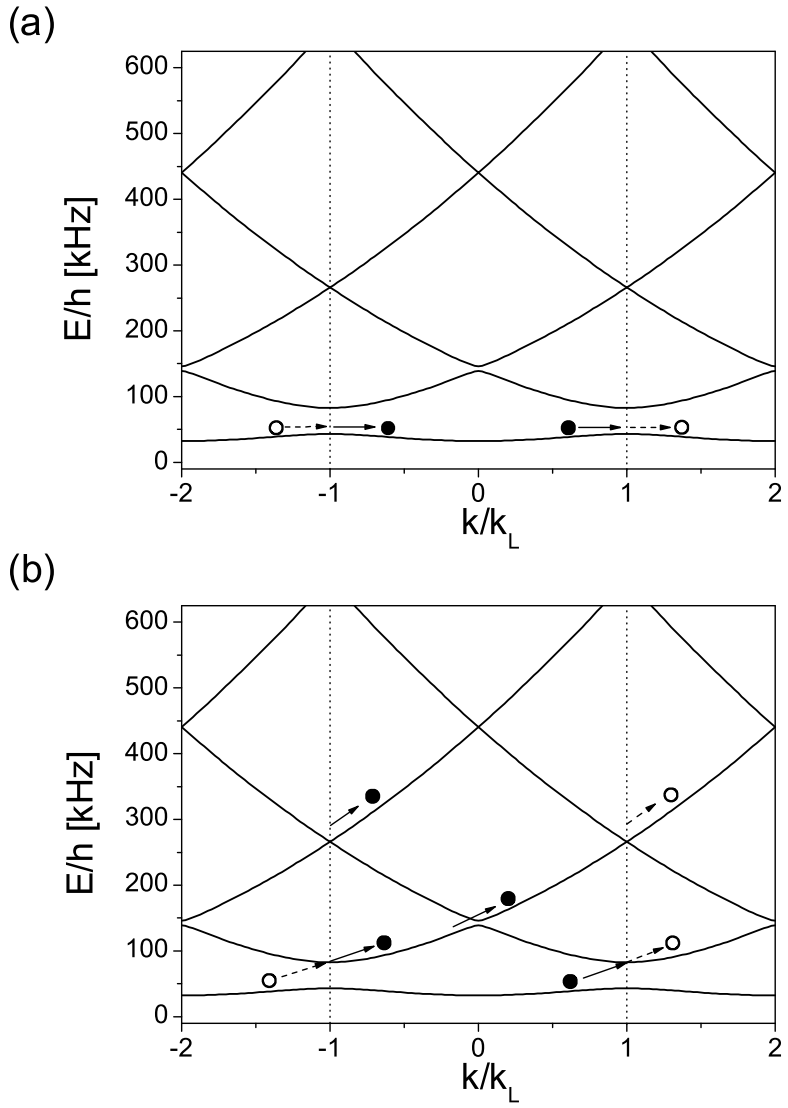

Figure 1.2: Schematic of Bloch oscillations and tunneling in reciprocal space, illustrated within the repeated-zone scheme. In part (a), a particle moves across the first energy band due to a small acceleration. At the edge of the corresponding first Brillouin zone it continues traveling along the same band. In the reduced-zone picture, however, the particle disappears, emerging at the opposite edge to complete a Bloch oscillation. Panel (b) presents a similar picture for the case of large accelerations. The particle cannot follow the dispersion curve and tunnels to a higher band. For this plot $V_0/h = 40$ kHz.

The problem of atoms in an accelerated optical lattice can be treated quantum mechanically using a Landau-Zener tunneling process based on diabatic transitions in momentum space [18]. An alternative description can be derived in the position representation [19].

As stated before, a particle approaching an avoided level crossing between energy bands might not be able to follow the dispersion curve adiabatically, in which case it continues its motion and diabatically changes levels across the energy gap (Fig. 1.2). The expression for the probability P of diabatic transfer between two repelled levels [20] is

$$P = \exp\left(-\frac{\pi}{2\hbar}\,\frac{E_{\rm g}^2}{\frac{d}{dt}(\epsilon_1-\epsilon_2)}\right), \tag{1.44}$$

where $E_{\rm g}$ is the minimum energy separation of the perturbed levels and $\epsilon_{1,2}$ are the unperturbed energy eigenvalues of level 1 and 2, respectively. In our case, for atoms in the lowest band, the unperturbed levels correspond to the free particle curves

$$\epsilon_1 = \frac{p_1^2}{2M}, \text{ where } p_1 = taM \tag{1.45}$$

$$\epsilon_2 = \frac{p_2^2}{2M}, \text{ where } p_2 = 2\hbar k_{\rm L} - taM, \tag{1.46}$$

which gives the following:

$$\left|\frac{d}{dt}(\epsilon_1-\epsilon_2)\right| = (2\hbar k_{\rm L})a. \tag{1.47}$$

Substitution into Eq. (1.44) yields for the probability of transfer

$$P = e^{-a_{\rm c}/a}, \tag{1.48}$$

where the critical acceleration $a_{\rm c}$ is given by

$$a_{\rm c} = \frac{\pi}{4}\,\frac{E_{\rm g}^2}{\hbar^2 k_{\rm L}} = \frac{\pi^2}{4}\frac{(V_0/h)^2}{E_{\rm r}/h}v_{\rm r}. \tag{1.49}$$

This formula can be compared with our previous two encounters with critical acceleration, Eqs. (1.41) and (1.43).

Let N denote the number of particles populating the lowest band within the first Brillouin zone. Since the atom is performing Bloch oscillations, it encounters the edge of the Brillouin zone every Bloch period. The probability for an interband transition per unit time is

$$\Gamma_{\mathrm{LZ}} = \frac{a}{2v_{\mathrm{r}}}\, e^{-a_{\mathrm{c}}/a}. \tag{1.50}$$

The population N decays exponentially

$$N = N_0\, e^{-\Gamma_{\mathrm{LZ}}\, t}. \tag{1.51}$$

What we have just presented constitutes a *bona fide* unstable system. Experimental studies of the tunneling rates out of the lowest band were performed in our group and the decay rates were compared to the Landau-Zener prediction [21, 22].

1.2.5 Non-exponential decay

An exponential decay law can be derived for systems which are describable in terms of perturbation theory [23]. In this context an unstable system is known to be in an initial discrete state at time t, only to decay randomly at time $t' > t$ to a quasi continuum of final states. The paradigm of a decaying system is a radioactive nucleus, and the exponential decay may well be used to define an unstable system. However, this law is not fully consistent with quantum mechanics. From a few basic arguments it can be shown that deviations at both short and long times must be expected [24, 25, 26, 27].

For very short times the time evolution of the survival probability can be determined explicitly. Given that the mean energy of the decaying state is finite, it can be shown that [27]

$$\left.\frac{dP(t)}{dt}\right|_{t\to 0} = 0. \tag{1.52}$$

While this is a very general statement for any unstable system, it does not specify the times at which decay settles into an exponential. Greenland and Lane point out a number of time scales which are relevant [28]. The first time scale τ_{e} is given by the time that it takes the decay products to leave the bound state region. This time can be estimated as

$$\tau_{\mathrm{e}} = \frac{\hbar}{E_0}, \tag{1.53}$$

where E_0 is the energy released in the decay. For nuclear systems this time is of the order of 10^{-21} seconds. The second time scale τ_{w} is related to the bandwidth ΔE of the continuum to which the state is coupled

$$\tau_{\mathrm{w}} = \frac{\hbar}{\Delta E}. \tag{1.54}$$

Deviations from exponential decay have been searched for unsuccessfully in the decay of radioactive isotopes, with measured times in the range of 10^{-4} to 45 half-lives [29]. However, deviations from exponential decay are expected in our system which are well within experimental reach. By using a two-band model for the accelerated lattice, Niu and Raizen [30] found an initial non-exponential regime that starts with a quadratic time dependence, and then becomes oscillatory. The oscillations damp out after a time

$$t_{\mathrm{c}} = \frac{E_{\mathrm{g}}}{a}\,\frac{1}{2\hbar k_{\mathrm{L}}}. \tag{1.55}$$

For a typical value of acceleration $a = 10,000\,\mathrm{m/s^2}$ and a band gap of $E_g/h =$ 80 kHz, the crossover time is $t_c = 2\,\mu$s. This time is accessible experimentally, and is the key feature which allowed the observation of non-exponential decay in our group [31]. Access to the non-exponential time in our system also made possible the observation of both Zeno and Anti-Zeno effects. By repeatedly resetting the evolution while the system was decaying we managed to alter the dynamics and show the existence of these remarkable quantum effects.

1.3 The Zeno and Anti-Zeno effects

From its foundations, quantum mechanics assigns a special role to the observer of any physical system. The fact that any measurement of a quantum system projects it to one particular eigenstate has counter-intuitive consequences. One of such effects is the prediction by Misra and Sudarshan that repeated observations on an unstable system can slow down its evolution to the point that, for frequent enough observations, decay can be completely inhibited [32, 33]. This is known as the Zeno effect. More recently, it was predicted that under more general conditions repeated measurement can enhance the decay [34, 35, 36], a phenomenon which was called Anti-Zeno (or Inverse-Zeno) effect. The experimental observation of these effects relies on the ability to reset the evolution of the system during the non-exponential time of the decay. Unstable systems like a radioactive nucleus or an atom in an excited state possess non-exponential times so short that are currently inaccessible to experiment. This is why the observation of these effects has been elusive until now.

A review of the Quantum Zeno effect can be found in reference [24]. The idea of the effect is to use the condition stated in Eq. (1.52) to slow decay.

Following general arguments, it can be shown [15, 37] that the probability for decay of a system known to be in state $|\psi_0\rangle$ at $t = 0$ under the action of Hamiltonian H is

$$P(t) = 1 - \frac{t^2}{\hbar^2}\langle\psi_0|(H - \bar{E})^2|\psi_0\rangle = 1 - \frac{t^2}{\hbar^2}\langle\Delta H^2\rangle, \tag{1.56}$$

for very short times. The initial energy is $\bar{E} = \langle\psi_0|H|\psi_0\rangle$. If a measurement is performed on the system at time $t = \tau$ the probability for finding the particle in the same state will be $P(\tau)$. The repeated action of n measurements at equal time intervals will give for the probability after time $t = n\tau$:

$$P(n\tau) = \left(1 - \frac{\tau^2}{\hbar^2}\langle\Delta H^2\rangle\right)^n. \tag{1.57}$$

The expected time scales for non-exponential decay are given by Eqs. (1.53) and (1.53). Setting $\tau \ll \hbar/\Delta H$:

$$P(t) \simeq \left(1 - \frac{n\tau^2}{\hbar^2}\langle\Delta H^2\rangle\right), \tag{1.58}$$

which in the limit of a large number of observations made at very short time intervals gives

$$\lim_{\substack{\tau\to 0 \\ n\to\infty}} P(t) = 1. \tag{1.59}$$

The system is found never to decay! Facing such result, Misra and Sudarshan ask themselves [32]: "Is it a curious but innocent mathematical result or does it have something to say about the foundation of quantum theory?" While the discussion still continues [36], experimental efforts have been scarce. In the past, measurement-induced suppression of the dynamics of a two-state driven system has been observed [38, 39], but no such effect was ever measured on an unstable system.

The original prediction of the quantum Zeno effect has been recently revisited [34, 35, 36]. The studies focused on the frequency of observations, and on the decay of an unstable system as a consequence of a reservoir of possible states. The result was the prediction of the opposite effect. It was found that, under more general conditions, repeated observations must shorten the lifetime of the unstable system, which was called 'Anti-Zeno' or 'Inverse-Zeno' effect. Because of the characteristic features of decay of our system, we were able to observe both effects just by adjusting the interruption interval, as it will be described later.

Chapter 2

Experimental techniques I

In this chapter we begin the description of the experimental techniques implemented to observe the Quantum Zeno and Ani-Zeno effects. We start by giving a review of the most basic concepts used in our research, namely, spontaneous processes involved in the dissipative forces used to cool and trap atoms. We then turn to the description of quantum transport experiment and its results. Finally, an account of a few techniques implemented to cool and transport atoms is given. Information regarding the cooling limits for sodium atoms using resonant or near resonance light was found.

2.1 Laser cooling

When an atom is subject to light in resonance with an atomic transition, it will spontaneously absorb and emit a photon. In this interaction conservation of momentum plays an extremely important role. Upon absorption, the atom carries its initial momentum plus that of the incoming photon. Upon emission, momentum is again conserved, as the atom experiences a recoil in the opposite direction to that of the outgoing photon. Because spontaneous processes are dominated by dipole transitions, they are spherically symmetric. This means that atoms will emit photons with the same probability in any direction, and, on the average, the momentum of the atomic center of mass will not change during emission. After many cycles, the net effect on the atom due to absorbing

photons with the same wave vector will be a push in that same direction.

On the average, a single absorbed photon causes the atom to recoil, acquiring a momentum equal to $p_{\mathrm{r}} = \hbar k_{\mathrm{L}} = M v_{\mathrm{r}}$, where M is the atomic mass, k_{L} the wavevector of the light beam, and v_{r} the *recoil velocity*.

The mechanical action of light on atoms is at the basis of the field of experimental atom optics. In particular, the dissipative process of spontaneous absorption and emission is routinely used to produce very cold atomic samples. The velocity acquired by the atom in the recoil process is extremely small, 3 cm/s in the case of sodium. It is the repeated action of millions of scattering events that brings the atoms from velocities of 700 m/s to 20 m/s in the case of a Zeeman slower, and further down to 20 cm/s in the case of a regular magneto-optical trap.

It is of interest to note that the mechanical action of light is not limited to linear momentum, but angular momentum can be transferred as well. The first experimental proof for the spin of the photon was done by C. V. Raman in 1932 [40]. An accurate measurement was later performed by R. Beth in 1936, by measuring the torque on a waveplate due to incident polarized light [41].

2.1.1 The use of two level atom theory

Two level atom theory describes very well the interaction of light and the alkali elements of the periodic table, and is the model we use every day to understand the processes involved in our tools and experiments. However, further knowledge is needed in the presence of electromagnetic fields that shift the energy of atomic levels and, more importantly, remove degeneracies between

hyperfine sublevels. The polarization of the light determines selection rules and optical pumping rates by means of transition strengths that reflect the matrix elements of electric dipole transitions. All this ignores, as mentioned before, relaxation processes due to collisions.

2.1.2 Transversal heating

As discussed earlier, the probability for spontaneous emission is the same in any direction, this as a result of the spherical symmetry of dipole radiation. Therefore, after the atom has scattered N photons from a beam with wavevector $\mathbf{k}_{\mathrm{L}}$, on the average it will recoil with a momentum equal to $\langle \mathbf{p} \rangle = NMv_{\mathrm{r}}\hat{k}_{\mathrm{L}}$. An important side effect is the heating of the atomic sample in the direction transverse to $\mathbf{k}_{\mathrm{L}}$, due to the random nature of the spontaneous absorption and emission process. As in any random walk effect, the root mean square (rms) increase in momentum is proportional to $\sqrt{N}$. We therefore write the momentum increase of the sample after N spontaneous absorption-emission cycles as $\sigma^{p}{}_{\mathrm{heating}} = \sqrt{N}Mv_{\mathrm{r}}$.

2.1.3 Optical molasses

Soon after experimental demonstrations of light forces on atoms were made, it seemed feasible to achieve cooling in three dimensions of an atomic gas. This experiment was first made in 1985 by Steven Chu and coworkers, using sodium atoms [42]. Laser cooling involving resonant transitions is a dissipative process that uses the Doppler effect to lower the temperature of the gas. Given light propagating in direction $\hat{k_{\mathrm{L}}}$ with frequency ω_{L}, and a collection of atoms with certain velocity distribution, the Doppler effect brings in or out of resonance a particular velocity class of the distribution. In one dimension, a beam of light

tuned to the red of the atomic transition induces many scattering cycles in an atom that moves towards the beam as the light frequency gets blue shifted in the moving frame of the atom. The expression for the scattering rate in Eq. (6.5) transforms to

$$R_{\rm sc} = \frac{\Gamma}{2}\frac{S_0}{(1+S_0+4(\Delta/\Gamma)^2)}, \tag{2.1}$$

where the detuning now takes into account the Doppler effect and a Zeeman term due to the interaction with a weak external magnetic field $\mathbf{B}$:

$$\Delta = \Delta_{\rm L} + \bar{k}_{\rm L}\cdot\mathbf{v} - \bar{\mu}\cdot\mathbf{B}, \tag{2.2}$$

with $\bar{\mu}$ being the atomic magnetic dipole moment.

Cooling in one dimension can be achieved by employing two counter propagating beams, a configuration known as *optical molasses*. The cooling comes at the expense of transversal heating as discussed before. Three dimensional molasses uses an arrangement of three mutually orthogonal pairs of counter propagating beams tuned to the red of resonance (with respect to atoms of zero velocity in the lab frame). A natural cooling limit to this technique is reached when the Doppler shift is comparable to the natural linewidth of the excited state: $M{v_{\rm D}}^2/2 = \hbar\Gamma/4$ [43]. For sodium $v_{\rm D} = 29$ cm/sec.

Soon after the first optical molasses was implemented, observations of temperatures below this limit were reported and explained afterwards [44]. The basis of the effect is a selective optical pumping that uses the light shifts provided by changes in polarization and gradients in intensity to dissipate energy once the atom has climbed a part of the potential. Using the polarization gradient cooling technique (PGC), atomic samples with velocity spread of a few recoils can now be routinely achieved [45, 46, 47].

2.1.4 The magneto-optical trap

The Magneto Optical Trap (MOT) is the work horse of our lab, providing a solid and robust source of cold atoms ready for experiments or further cooling. After 1985, some physicists started to think ways not only to cool but to trap atoms. Magnetic traps were experimentally demonstrated with atomic sodium that year [48], but it was not clear how to combine the two techniques to trap and cool atoms at the same time. Two years later, based on an idea by Jean Dalibard, Steven Chu's group achieved the first magneto-optical trap (MOT) [49]. The idea was to use the Zeeman shift of a magnetic field gradient to achieve a position dependent force. Since a magnetic field lifts degeneracies in the hyperfine sublevels of the atom, it is possible to use molasses beams that have different circular polarizations to increase the radiation pressure as atoms move away from the center of the trap. The magnetic field configuration chosen was a quadrupole field (created by two identical coils in the anti-Helmholtz configuration), which provides cylindrical symmetry and linear gradients.

The trapping and cooling of neutral atoms relies on the existence of cycling transitions, as hundreds of thousands of spontaneous scattering events are needed to slow atoms from thermal sources. This is why the alkali atoms were the first elements to be chosen for laser cooling. In sodium, we use the transition $3S_{1/2}(F = 2) \longrightarrow 3P_{3/2}(F' = 3)$ to cool and trap the atoms, see Fig. 2.1. However, as mentioned before, the two level atom picture is incomplete, and the hyperfine structure has allowed dipole transitions to other states that permit the atom falling into a dark state. To solve this, light is needed to pump the atoms back into the cycling transition. This light is called the *repump*, and in the case of sodium is tuned resonantly between the states

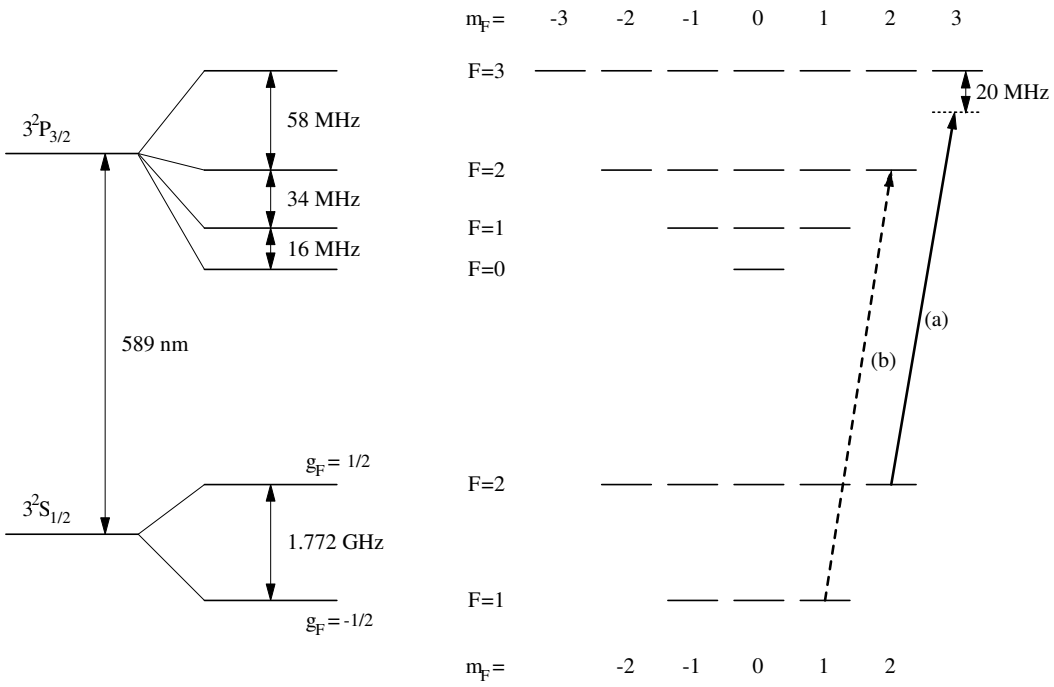

Figure 2.1: A structure diagram for the D2 line in sodium. The cycling transition used to cool and trap atoms occurs between the $3S_{1/2}(F = 2) \longrightarrow 3P_{3/2}(F' = 3)$ hyperfine levels (a). Scattering due to excitation of the $(F' = 2)$ state sends the atom to a ground dark state $(F = 1)$. The repump light (b), pumps the atom back into the cycle.

$3S_{1/2}(F = 1) \longrightarrow 3P_{3/2}(F' = 2)$. When the hyperfine structure levels of the excited state are far apart compared to the natural linewidth of the transition, as in the case of rubidium or cesium, the repump is not as important. However, in lighter atoms like lithium or sodium the repump is key. In our experiment, we have learned to have due respect for this light that protects us from the dark state.

Using a MOT in our lab, we trap up to 5×10^7 sodium atoms from a vapor cell and 3×10^9 atoms from a slowed atomic beam (Chapter 4). The

velocity distributions of the samples have rms values on the order of $\sigma_{\rm v} = 10\, v_{\rm r} = 30$ cm/s, ($\sigma_{\rm v}$ equal to the rms of a gaussian fit). Application of polarization gradient cooling produces distributions having $\sigma_{\rm v} = 6\, v_{\rm r}$.

2.2 The earlier sodium experiment

2.2.1 The laser system

The laser system used to trap and cool atoms in our MOT is essentially the same setup implemented and discussed by former members of our lab [6, 50].

The light necessary to form the MOT in sodium is obtained from a dye laser (Coherent 899-21). The laser is pumped by an Argon ion laser with 7 W of power (Coherent Sabre). The output from the Coherent 899 is 1 W typically, frequency locked +60 MHz respect to the $3S_{1/2}(F = 2) \longrightarrow 3P_{3/2}(F' = 3)$ atomic transition. The frequency locking is done by a saturation spectroscopy FM scheme, that provides the feedback signal to the dye laser frequency control electronics [50]. The use of a dye laser requires care and patience, but it works very reliably over periods of 3 months, which is the time that signals a change of dye (Rhodamine 6G). An advantage of this type of laser is the power available. On the other hand, it has several disadvantages as it requires regular maintenance and alignment. Also, the output beam naturally presents imperfections like pointing instability and position drifts over the period of few hours. In the past, we tried to compensate for pointing instability by using polarization preserving optical fibers, which we presently do not use because they present losses on the order of 25% or more. In order to obtain good quality beams, we spatially filter both cycling and repump light for the MOT.

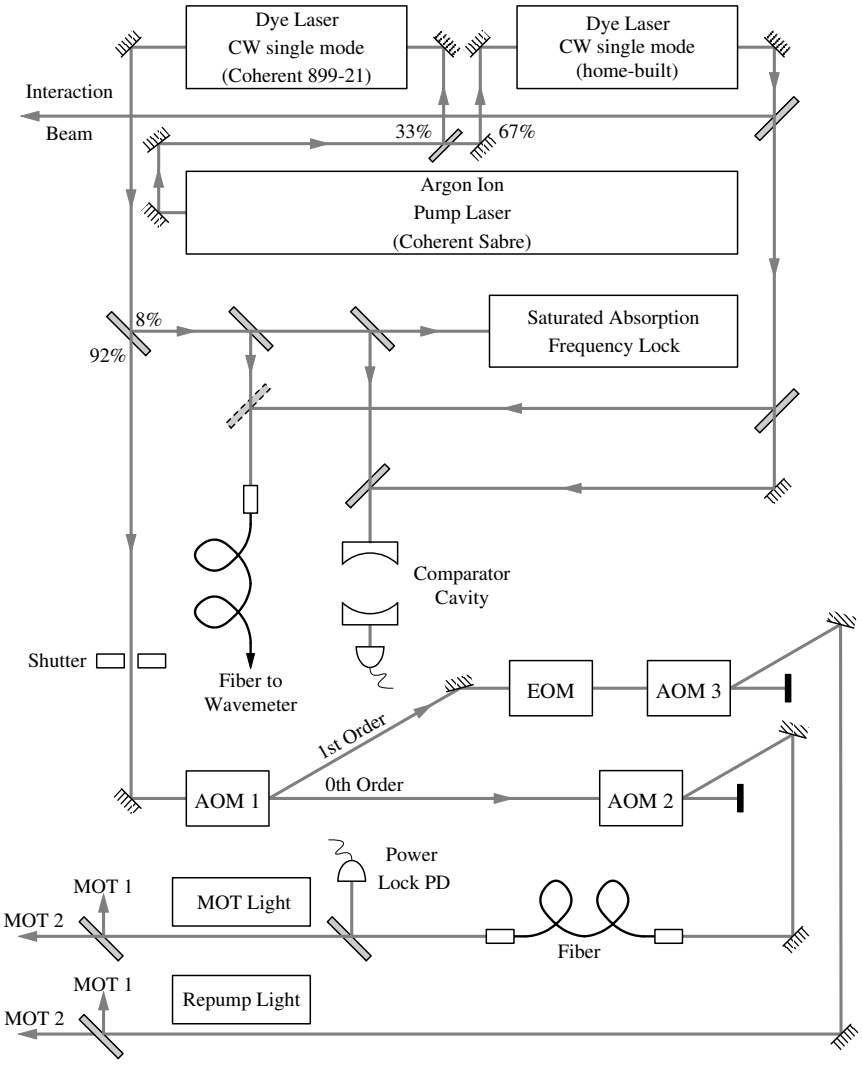

Figure 2.2: A schematic of the laser setup producing the light necessary for cooling, trapping and imaging sodium atoms. A second dye laser provides the light for the optical lattice used in the quantum transport experiments.

As stated before, the power available from the Coherent 899 is about 1 W. A 270 MHz AOM splits the power, sending 60% in its zeroth order to the cycling light, and the rest to the repumper in the +1st diffracted order (Fig. 2.2). The cycling beam then passes through another AOM, that shifts its frequency by -80 MHz, leaving a final detuning of -20 MHz respect to the $3S_{1/2}(F = 2) \longrightarrow 3P_{3/2}(F' = 3)$ transition. The last AOM is used to lock the intensity of the beam by feeding back an error signal obtained from the output of a monitor photodetector to the AOM rf amplitude driver.

The repump passes through a 1.442 GHz electro-optical modulator (EOM), that creates sidebands at ± 1.442 GHz. Only the upper sideband is relevant for repumping, carrying about 30% of the total beam power. For switching purposes another -80 MHz AOM is used in its path, which shifts its frequency to bring it to a final detuning of +1.732 GHz respect to the cycling light. The repump is therefore resonant with the $3S_{1/2}(F = 1) \longrightarrow 3P_{3/2}(F' = 2)$ transition. The total power used for the MOT light is about 100 mW, and 70 mW for the repumper, both measured after spatial filtering.

2.2.2 Vacuum chamber

In this section we mention the most important parts of the experimental apparatus used in the observation of the Zeno and Anti-Zeno effects. A full description can be found in reference [15].

Our system made use of a double MOT: atoms from a vapor cell were collected in a MOT inside a region of relatively low vacuum (10^{-9} Torr), and then transferred to a lower MOT by pushing them with a light pulse. The two regions were 25 cm apart, with their centers displaced horizontally forming a

45° configuration. They connected using low conductance tubing to allow for ultra-high vacuum in the lower MOT region.

The transfer method chosen was a short pulse of light, that imparted the highest velocity possible to the atoms while still below or equal to the capture velocity of the lower MOT (20 m/s). Magnetic guiding along the connecting tube was used to maximize the transfer. After optimization, the maximum transfer efficiency in this system was about 10%. For the quantum transport experiments, having a large atom number is not necessary, and this small transfer efficiency was therefore not a problem. For quantum reflection studies however, the requirements are much stringent and the low efficiency was a limiting factor. We will come back to this point when we discuss several techniques implemented in order to compensate for the low number of atoms.

2.3 Observation of the Quantum Zeno and Anti-Zeno effects

2.3.1 The optical lattice

The laser light used to create the optical lattice was provided by a home-built dye laser [15], which was pumped by the argon ion laser with 10 W of power. Typical output power was 1 W, locked to an external reference cavity which drifted less than 100 MHz per hour, much smaller than the detunings used (typically 40 GHz).

Light from the dye laser was sent to an AOM for overall intensity control. The first diffracted order was split in two beams of equal intensity. The first beam went through an AOM in the double pass configuration, Fig. 2.3. This is the beam that changes its frequency as the experiment takes place.

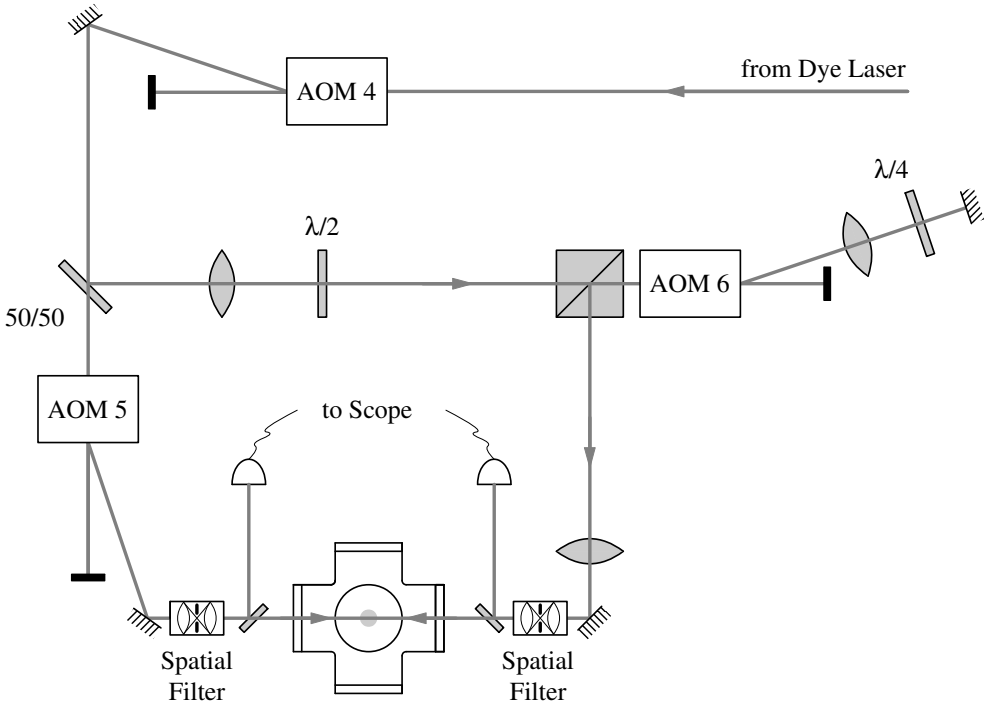

Figure 2.3: Experimental setup used to create the accelerating optical lattice. Overall intensity control is provided by AOM4. The frequency chirped beam is produced by AOM6 ($40 \pm \delta/2\pi$ MHz). To compensate for the offset in the frequency, AOM5 is used in the second lattice beam (40 MHz).

Because a change in the frequency due to the AOM modifies the diffraction angle, a misalignment is avoided by using the first diffracted order and retro reflecting it back for a second pass. The overall shift in frequency is then equal to twice the driving frequency of the AOM. In order to extract the beam, a pair of waveplates and a polarizing cube beam splitter are used. The second beam was sent through another AOM, to compensate for the frequency shift of the double pass. Having the beams with the same frequency is important initially when loading atoms into the lattice.

After passing through the AOM's the beams are cleaned using a spatial filter, and collimated to their final sizes. A typical value for the beam waist w_0 in the quantum transport experiments was about 2 mm. Since the power in the laser fluctuates constantly, a small fraction of the power in each beam was picked off for monitoring purposes. Only those runs having beam intensities within a certain window were accepted, and the rest either discarded or repeated.

2.3.2 Experimental sequence

A schematic of the experimental sequence followed is depicted in Fig. 2.4. Typically, 3×10^5 atoms were collected in the MOT for a few seconds. A polarization gradient cooling stage left a cloud with a typical width $\sigma_{\mathrm{x}} = 0.3$ mm in position and $\sigma_{\mathrm{p}} = 6\,\hbar k_{\mathrm{L}}$ in momentum. At this point all the trapping fields were switched off, and the interacting beams turned on. An acceleration sequence was imposed, and it will be discussed in detail shortly. After acceleration, the lattice beams were switched off, and the atoms were left to expand freely for a few milliseconds. During this period of ballistic

expansion the atoms moved a distance proportional to their velocity. This allowed us to measure the momentum distribution of the atomic sample after the acceleration sequence by recording a spatial profile of the distribution.

The imaging of the atoms was done by turning all MOT and repump beams back on, without the magnetic field from the MOT. This configuration is known as *freezing molasses*, as it stops atomic motion for tens of milliseconds, enough time to record a picture. As the atoms scatter the resonant light from molasses, a picture is taken recording fluorescence using a CCD camera. The pictures are then integrated along the direction perpendicular to transport (Fig. 2.5). From these lineshapes we calculate the number of atoms that survived the entire sequence and we divide over the total number of atoms that were trapped in the lattice. This gives us the survival probability, which is the quantity we measure in our experiments.

2.3.3 The Zeno and Anti-Zeno effects: results

The light used for the lattice had typical detunings ranging from 40 to 60 GHz from the $(3S_{1/2}) \leftrightarrow (3P_{3/2})$ transition. The power in each of the beams was adjusted up to 150 mW. Due to the larger initial momentum spread of the atomic distribution, switching on the interaction potential populated several of the lower energy bands. Atoms projected into the lowest band are trapped within the potential wells whereas atoms in the second band are only partially trapped. Atoms in even higher bands have energies well above the potential and hence are effectively free.

In order to have a well defined initial condition, we emptied all but the lowest band. We achieved this by accelerating the standing wave with an

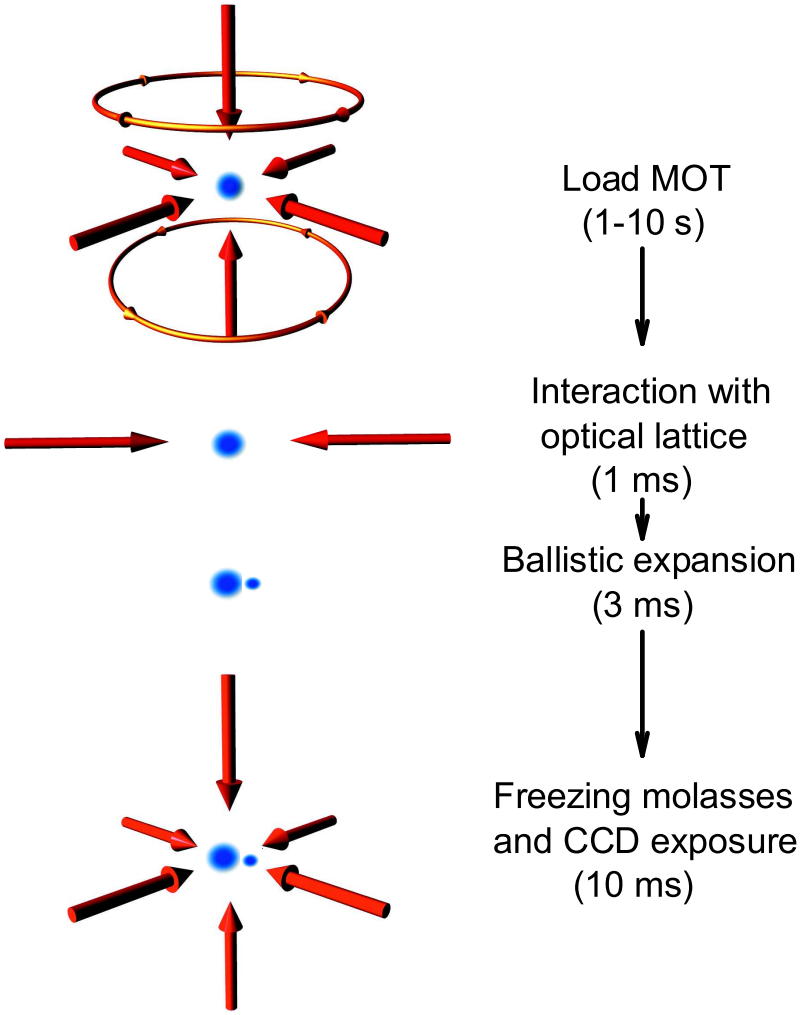

Figure 2.4: A schematic of the experimental sequence followed in the quantum transport experiments. Atoms are collected in a MOT during a few seconds. Next, all trapping and cooling fields are turned off, and the interacting lattice is turned on and accelerated appropriately. After the interaction the lattice beams are turned off, followed by a few milliseconds of ballistic expansion. Finally, the atoms are imaged using freezing molasses.

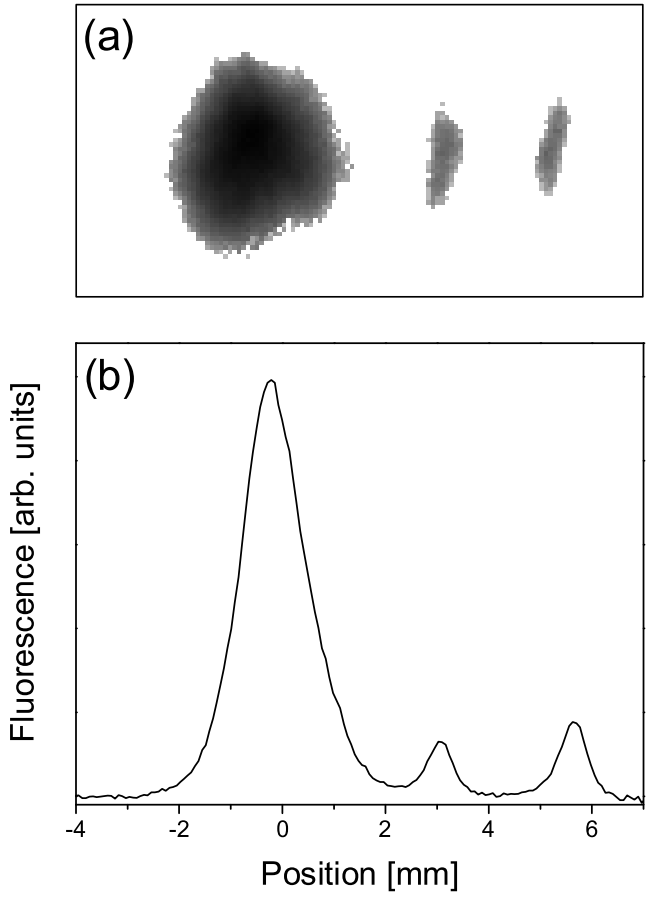

Figure 2.5: (a) A picture of the atomic distribution after time of flight. The bigger spot corresponds to atoms that were never trapped by the lattice. The central distribution corresponds to those atoms that were loaded into the lattice but escaped confinement during tunneling. Finally, the rightmost peak corresponds to atoms that remained trapped during the entire sequence. Part (b) shows an integrated lineshape along the direction perpendicular to the lattice. This allows us to quantify the survival probability.

acceleration a_{trans} to a velocity of $v_0 = 35\, v_{\text{r}}$ by linearly chirping the frequency of one of the counter-propagating beams while keeping the frequency of the other beam fixed. The acceleration of the potential leads to a loss of population in the lower bands due to Landau-Zener tunneling of atoms into higher un-trapped bands. Energy gaps between successive energy bands decrease rapidly. Therefore, the transport acceleration a_{trans} was chosen to maximize tunneling out of the second band while minimizing losses from the first trapped band. This ensured that after the initial acceleration only the first band still contained a significant number of atoms.

After reaching the velocity v_0 the acceleration was suddenly increased to a value a_{tunnel}, where appreciable tunneling out of the first band occurred. The beginning of this large acceleration period determined the start of the experiment, or $t = 0$, and was maintained for a period of time t_{tunnel}. At the end of this tunneling period we continued the frequency chirping at the decreased rate corresponding to a_{trans}. During this segment atoms that escaped the potential were left behind while atoms still trapped at the end of tunneling were taken to higher velocities. This allowed us detection of 'stable' and 'decayed' atoms. After reaching a final velocity of $75\, v_{\text{rec}}$ the interaction beams were switched off suddenly. A diagram of the velocity profile versus time is shown in Fig. 2.6 (a).

The quantity to be measured in our experiment was the fractional number of atoms that remained trapped in the first band after the tunneling time. At the end of the acceleration sequence the atoms were separated in momentum space but overlapped in position space. To distinguish between the two classes of atoms, a period of ballistic expansion was implemented. After an

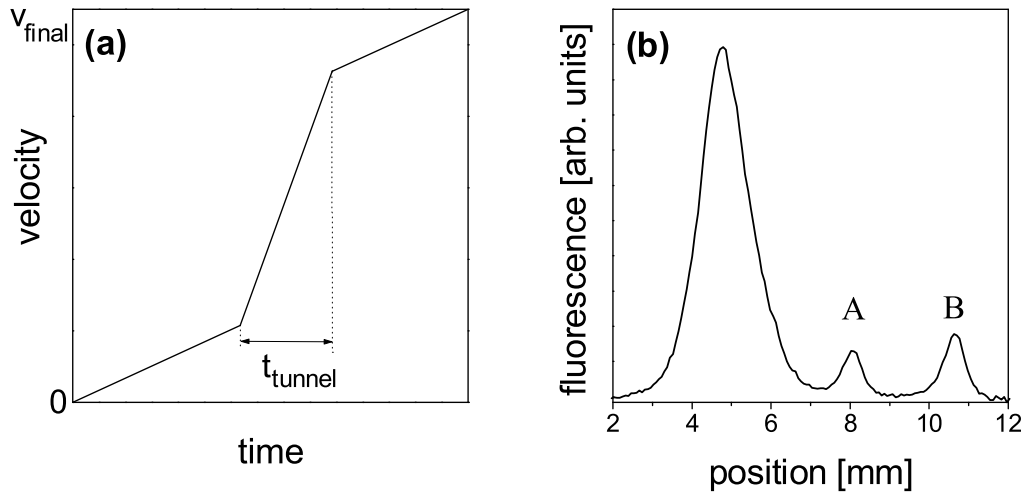

Figure 2.6: Part (a) shows a diagram of the acceleration sequence. Part (b) displays a typical integrated spatial distribution of atoms after the time of ballistic expansion. The large peak on the left shows atoms that were lost during the preparation of the initial condition, first segment of the acceleration sequence. The peak with label A indicates the atoms that escaped the potential during the tunneling time. The atoms that remained trapped the entire sequence correspond to label B. The survival probability is therefore equal to A/(A + B).

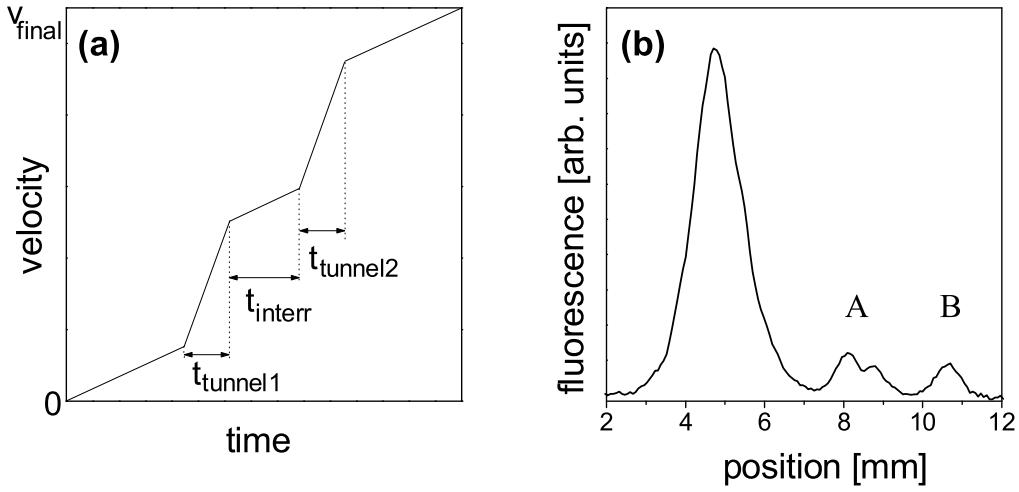

Figure 2.7: Part (a) shows a diagram of the interrupted acceleration sequence. The total tunneling time is the sum of all the tunneling segments. Part (b) shows a typical integrated spatial distribution of atoms after the time of ballistic expansion. One interruption was implemented in this case. The peaks can be identified as in Fig. 2.6. However, the area A containing the tunneled fraction of the atoms is now composed of two peaks. Atoms that left the well during the first tunneling segment are offset in velocity from the ones having left during the second period of tunneling. The amount of separation is equal to the velocity increase of the well during the interruption segment.

atom tunneled out of the potential during the sequence, it maintains the velocity it had at the moment of tunneling. Turning off the light beams allowed the atoms to expand freely. During this period each atom moved a distance proportional to its velocity. Due to the difference in final velocities, trapped and tunneled atoms separated and could be spatially resolved (Fig. 2.6). A typical integrated distribution is shown in Fig. 2.6 (b). For this trace, about one third of the initially trapped atoms have tunneled out of the well during the fast acceleration period.

We measured the decay of the unstable system by repeating the exper-

iment for various tunneling durations t_{tunnel}, holding the other parameters of the sequence fixed. In the past, our group observed deviations from exponential decay following a similar procedure [31]. In our case, we focused on the effect of measurements on the system decay rate.

There are two key facts used towards the observation of both Zeno and Anti-Zeno effects. The first one corresponds to the possibility of having experimental access to the non-exponential time of decay. The second concerns the resetting of the evolution during the non-exponential region. As mentioned before, the quantity to be measured is the fraction of atoms remaining trapped in the potential after some tunneling time. This measurement could be realized, as before, by suddenly interrupting the tunneling duration by a period of reduced acceleration a_{interr}, as indicated in Fig. 2.7(a). During this interruption tunneling was negligible and the atoms were therefore transported to a higher velocity without being lost out of the well. This separation in velocity space enabled us to distinguish the remaining atoms from the ones having tunneled out up to the point of interruption, as can be seen in Fig. 2.7(b). At the end of the measurement the acceleration is switched back to a_{tunnel}, and the system can then be returned to its unstable state where it continues the decay. This procedure defined a new initial state with the remaining number of atoms as the initial condition. Since the 'clock' was reset, the system starts its evolution again with the same non-exponential decay features. It is important to note that the requirements for this interruption section were very similar to those during the transport section, namely, the largest possible acceleration while maintaining negligible losses for atoms in the first band. This ensured that the only effect of the measurement was the separation in velocity space of trapped

and untrapped atoms. This is why a_{interr} was chosen to be the same as a_{trans}.

The sequence tunneling-measurement-tunneling can be repeated many times, and only the short tunneling segments contribute to the total tunneling time. The result of such a series of frequent measurements can be seen in Fig. 2.8. The hollow squares indicate the decay curve without interruption, where a non-exponential features are observed during the first 10 ms. The solid circles depict the measurement of the survival probability in which after each tunneling segment of 1 μs an interruption of 50 μs duration was inserted. The survival probability clearly shows a much slower decay than the corresponding system measured without interruption. This constitutes the first observation of the Zeno effect in an unstable system [1, 51], following the spirit of the original proposal by Misra and Sudarshan.

It is important to note that our experimental setup had a limited time response, and care was taken to include this into the analysis of the data. The response time was limited by electronic and electro-optic devices used in the experiment. The frequency response was measured and the resulting transfer function was used to calibrate the response of the optical potential to a desired change in acceleration. This ensured that only sections were included for which tunneling was substantial and established a lower bound for the actual tunneling duration. This effect was taken into account for the curves in Fig. 2.8. Quantum mechanical simulations of the decay were performed by numerically integrating Schrödinger's equation for the experimental sequence and determining the survival probability numerically [15]. The results are indicated as solid lines in Fig. 2.8. This simulations contained no adjustable parameters and are in good agreement with the experimental data. The seemingly larger

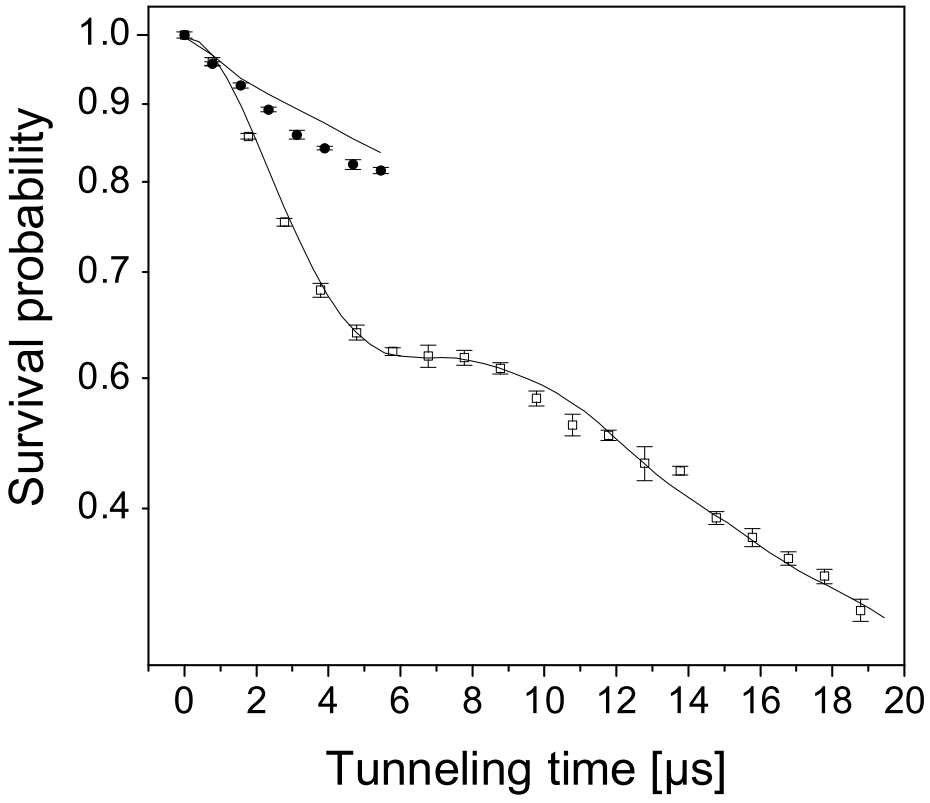

Figure 2.8: Probability of survival in the accelerated potential as a function of duration of the tunneling acceleration. The hollow squares show the non-interrupted sequence, the solid circles show the sequence with interruptions of 50 μs duration every 1 μs. The error bars denote the error of the mean. The data have been normalized to unity at $t_{\mathrm{tunnel}} = 0$ in order to compare to the simulations. The solid lines are quantum mechanical simulations of the experimental sequence with no adjustable parameters. For these data the parameters were: $a_{\mathrm{tunnel}} = 15,000\,\mathrm{m/s^2}$, $a_{\mathrm{interr}} = 2,000\,\mathrm{m/s^2}$, $t_{\mathrm{interr}} = 50\,\mu$s and $V_0/h = 91$ kHz.

decay rate for the Zeno experiment as compared to the simulation may be attributed to an under-estimate of the actual tunneling time.

During the non-exponential time, the uninterrupted decay curve shows two very distinct features. For acceleration times less than one microsecond the decay is much slower than the exponential decay. As just described, this was used in observing the Zeno effect by realizing the observations after such short times of tunneling. The other feature, however, is the completely opposite. After the initial period of slow decay the curve shows a steep drop as part of an oscillatory feature, which for longer times damps away to show the well-known exponential decay. Therefore, interrupting the decay right after the steep drop would lead the system to an overall decay that is faster than the uninterrupted decay [35]. This is the predicted Anti-Zeno effect.

The solid circles in Fig. 2.9 show such a decay sequence, where after every 5 μs of tunneling the decay was interrupted by a slow acceleration period. The length of the tunneling segments between the measurements are chosen in such a way as to include the periods exhibiting fast decay. As in the Zeno case, these interruption segments force the system to repeat the initial non-exponential decay behavior after every step. The interrupted curve of Fig. 2.9, indicated by hollow squares, clearly shows such a reproduction. The result is a dramatic decay that is much faster than for the uninterrupted case, namely the Anti-Zeno effect.

In our experiment, the ability to restart the quantum evolution translates to the ability to separate the two classes of atoms in momentum space. However, atoms trapped in the lowest band of the optical lattice have some distribution, which in our case is the width of the first Brillouin zone, $\delta p = 2Mv_{\mathrm{r}}$.

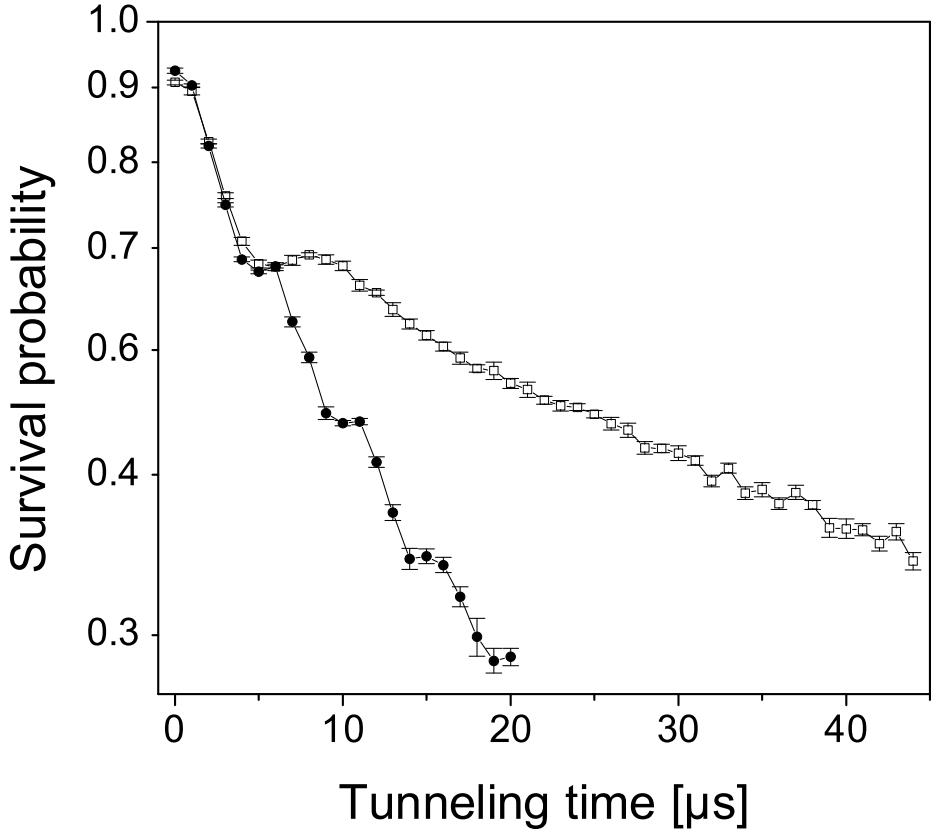

Figure 2.9: Survival probability as a function of duration of the tunneling acceleration. The hollow squares show the non-interrupted sequence, the solid circles show the sequence with interruptions of 40 μs duration every 5 μs. The error bars denote the error of the mean. The experimental data points have been connected by solid lines for clarity. For these data the parameters were: $a_{\mathrm{tunnel}} = 15,000\,\mathrm{m/s^2}$, $a_{\mathrm{interr}} = 2,800\,\mathrm{m/s^2}$, $t_{\mathrm{interr}} = 40\,\mu$s and $V_0/h = 116$ kHz.

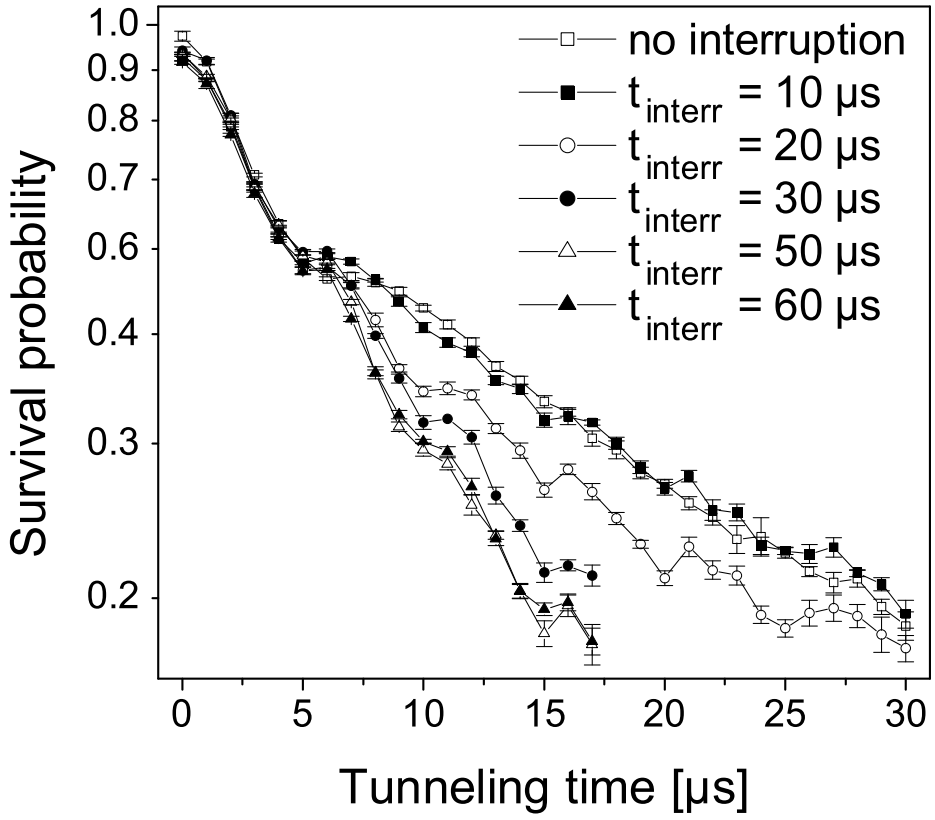

Figure 2.10: Survival probability as a function of duration of the tunneling acceleration. The hollow squares show the non-interrupted sequence, other symbols indicate the sequence with a finite interruption duration after every 5 μs of tunneling. The error bars denote the error of the mean. A further increase of the interruption duration than indicated does not result in a further change of the decay behavior. The experimental data points have been connected by solid lines for clarity. For these data the parameters were: $a_{\mathrm{tunnel}} = 15,000\,\mathrm{m/s^2}$, $a_{\mathrm{interr}} = 2,000\,\mathrm{m/s^2}$ and $V_0/h = 91$ kHz.

This fact sets a minimum time for the measurement, for it takes some time for an atom to be accelerated to the corresponding velocity. The time scale for the measurement is the Bloch period $\tau_{\mathrm{B}} = 2v_{\mathrm{r}}/a_{\mathrm{interr}}$. An interruption shorter than this time will not resolve the tunneled atoms from those still trapped in the potential, and therefore results in an incomplete projection of the atom number.

To investigate the effect of the interruption duration, we repeated the sequence to measure the Anti-Zeno effect for varying interruption durations while holding all other parameters constant. The results of this measurement are displayed in Fig. 2.10, where decay was interrupted every 5 μs with an acceleration of a_{interr} of 2000 $\mathrm{m/s^2}$. The hollow squares show the uninterrupted decay sequence as a reference. For an interruption duration smaller than the Bloch period of 30 μs the procedure is incomplete and has little or no effect. For a duration longer than the Bloch period the effect saturates and results in a complete restart of the decay behavior after every interruption.

2.4 Properties and limitations of cooling and transport methods using near resonance light

Right after the conclusion of the investigation of both Zeno and Anti-Zeno effects using optical lattices [1], it was time to maximize the number of atoms in our MOT so we could have a chance to implement magnetic trapping and subsequent cooling by evaporation. The goal of the experiment was to obtain sub-recoil atoms, and to launch them towards a glass prism placed inside the vacuum chamber. We expected to study the atom-surface interaction using an evanescent wave at the surface of the prism.

After optimization, the maximum transfer efficiency in this system was about 10%. This was disappointing, if we compare to the case of rubidium in a similar system to ours. In such a system reported efficiencies get close to 100% [52]. In our case, the maximum number of atoms collected in the lower MOT never exceed 1.2×10^7 (using a dark spot [53]). Two approaches were followed in order to improve our chances of obtaining subrecoil atoms: realization of a Type II MOT, and implementation of lattice cooling.

2.4.1 The Type II MOT

Back in 1987, the first MOT was experimentally demonstrated [49]. In that paper it is described how the trap worked for two different transitions between the hyperfine levels of the trapped sodium atoms. The transition used was the $3S_{1/2} \longrightarrow 3P_{3/2}$, and in one scheme the hyperfine levels used were $F = 2 \longrightarrow F' = 3$, with repump light between $F = 2 \longrightarrow F' = 2$ (Type I). The Type II trap was obtained by using the transitions between $F = 1 \longrightarrow F' = 0$, and $F = 2 \longrightarrow F' = 2$, and a larger number of atoms was reported [54].

We decided to implement the type II trap in the upper MOT to increase the number of atoms before they were transferred down. The trapping light was detuned accordingly, without success. It was not until we made the polarization of both trapping and repump light the same that we saw either type I or type II working, just by slightly changing the lock point in the saturation spectroscopy signal, Fig. 2.11.

Results. After optimization, the type II trap produced a factor of 3 more atoms than type I. While this was encouraging, we observed a factor of 70 less in density. Moreover, a factor of 35 higher in temperature compared

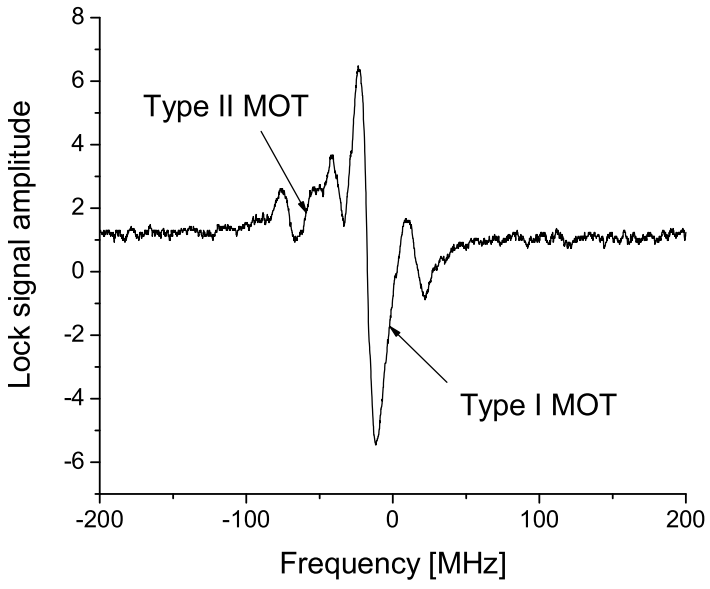

Figure 2.11: Saturation spectroscopy signal for the $3S_{1/2}(F = 2) \longrightarrow 3P_{3/2}(F' = 1, 2, 3)$ transitions of sodium. The lock points for both type I and type II traps are shown. For a normal MOT (type I), the frequency is locked 20 MHz to the red of the $3S_{1/2}(F = 2) \longrightarrow 3P_{3/2}(F' = 3)$ transition.

to type I was seen. At this point, we decided to try a 'linear combination' of both types of traps by placing sidebands in both trapping and repump light at 59 MHz. Our hope was that by controlling the relative amplitude between sidebands we could achieve a combination of large numbers and low temperatures. This worked to some degree, as the temperature of the atoms was closer to atoms in type I than in type II. However, the loading time became very long, on the order of 10 s. When calculating the ratio between the number of collected atoms over the loading time for different configurations of sidebands in the trapping beams, we found it to be constant. This ratio was the figure of merit for the upper MOT, since the efficiency of collecting the atoms there and transferring them to the lower MOT is directly proportional to the number of atoms launched, and inversely proportional to the time it takes to collect them.

In the end, we abandoned the type II MOT since there was no net gain in the flux. Using type I, our lower MOT contained on the order of 1.5×10^7 atoms after 30 s of loading into a dark spot.

2.4.2 Lattice cooling

With the limitation in the number of atoms available from the MOT, it was not possible to transfer them into a magnetic trap for further cooling using evaporation, the main reason being the low collision rate in the trap. As an alternative, we decided to implement lattice cooling [55, 56]. This method had been used in other groups (including our own lab in the experiment working with cesium [57]), to obtain atomic samples close to the recoil limit.

As mentioned earlier, in the year of 1988 several groups observed tem-

peratures below T_{D}, and a successful explanation came afterwards [45]. The polarization gradient cooling mechanism, which is a combination of optical pumping and stimulated scattering, produces cold samples with a typical rms velocity of $\sigma_{\mathrm{v}} = 5\, v_{\mathrm{r}}$. However, efforts to cool dilute gases to the recoil limit, and below, began immediately. One of these methods is lattice cooling, first demonstrated by the group of W. Phillips [55].

The idea of lattice cooling can be understood in two parts with three main components. The first part is the loading of the atoms from the MOT to the lattice, and its temporal coexistence for few milliseconds. The second one is the adiabatic release of the atoms from the lattice. The three main components are: the MOT, the repump light, and the lattice beams. Certain conditions must be fulfilled in order to achieve low temperatures as we now proceed to describe.

We start by saying that a major limitation in the density of atoms in a MOT is the number of atoms captured, due to the light that is randomly scattered by them. This light heats up the sample, limiting not only the density but the lifetime and the temperature as well [54]. One alternative is to reduce the amount of repump light (which is done during PGC). The only problem is that the spring constant of the trap can be severely diminished, resulting in a weak trap that cannot hold fast atoms. What one would like to do is to have the ability to reduce the intensity of the repump light, but keeping a tight confinement (very much like in a dark spot, Section 4.7.1). The reduction of the scattering of light with its subsequent heating would produce samples approaching the recoil limit. Lattice cooling in three dimensions achieves exactly that. The procedure goes as follows. A MOT is loaded for a few

seconds with an optical lattice superimposed to the fields of the MOT. After loading, the atoms are cooled using PGC. Then, the repump light is diminished as well as the trapping light. During this time the atoms are being cooled as in normal molasses, but now held in place by the optical lattice. As the cooling continues, the atoms fall into the ground state of the lattice, after which point the cooling stops. The atoms stay in the presence of the lattice only for a few milliseconds.

The second part of lattice cooling consists in the adiabatic release of the atoms. The light forming the lattice is extinguished adiabatically with respect to the trapping frequency of the confining wells, and the momentum spread is converted into position spread, which is negligible for dilute gases in a lattice.

Results. The light forming the optical lattice was obtained from a homemade dye laser. We constructed three sets of counter-propagating beams by sending three independent beams into the glass cell, and retro-reflecting them taking care to match the size of the incoming beam at the atomic position. The beams had relative detunings of: +95 MHz, +40 MHz, and 180 MHz respect to an arbitrary frequency. Also, each pair had an orthogonal polarization to the other two. This was done to avoid unwanted interference fringes between any pair of orthogonal beams. The waist of the beams at the position of the atoms had a geometrical mean of $w = 550\,\mu$m, about a factor of two larger than the typical rms size of the atomic distribution containing 5×10^6 atoms. Various detunings were tried, and we found the best results using anywhere between 8-15 GHz to the red of the $3S_{1/2}(F = 2) \longrightarrow 3P_{3/2}(F' = 3)$ trapping transition. During adiabatic decompression, we decreased the light

intensity according to $I(t) = I(0)/(1 + Lt)^2$, with L=150 kHz, following the work of Kastberg, et. al. [55].

After careful optimization, the lowest temperatures achieved in 3D were $\sigma_{\rm v} = 3.0\, v_{\rm r}$, which is a factor of 2 below our typical molasses (PGC) temperatures. In contrast, a similar setup implemented in our lab using cesium [57], obtained $\sigma_{\rm v} = 1.5\, v_{\rm r}$. One explanation for this discrepancy is found in the depth of the lattice relative to the characteristic unit of kinetic energy of the atom, that is, its recoil energy.

The following analysis is valid for 1D, but will give us an idea of the problem. Typical power in any beam forming the optical lattice was 35 mW. With $w = 550\,\mu$m, and a detuning $\Delta = 8$ GHz, the resulting well depth is $V_0 =$ 2.3 MHz= $92 \times E_{\rm r}$ ($E_{\rm r}$ is the energy associated with a single photon recoil), and the trapping frequency $\omega_0 = 2\pi\, 687$ kHz. The ratio $\varepsilon = E_{\rm r}/(\hbar\omega_0)$ was equal to 0.037, placing the atoms in the tightly bound regime. The scattering rate at the center of the lattice was R_{sc} =18 kHz, making the ratio $f = R_{sc}/\omega_0 =$ 0.026. The condition $f \ll 1$ has been identified as the figure of merit for the suppression of recoil induced heating [56]. We now compare with the experiment performed in cesium [57]. Typical well depths used were $V_0 = 1.75$ MHz, with a trapping frequency of $\omega_0 = 2\pi\, 170$ kHz. The scattering rate at the center of the lattice was $R_{sc} = 1$ kHz. The ratios $\varepsilon = 0.012$, and $f = 0.006$ were therefore similar to our sodium experiment numbers. Not surprisingly, the first part of lattice cooling yielded very similar results for both experiments. Right after a molasses stage, the cesium experiment obtained samples having $\sigma_{\rm v} = 6.5\, v_{\rm r}$, while for the sodium experiment this value is: $\sigma_{\rm v} = 6.0\, v_{\rm r}$. We note that $v_{\rm r}$ refers to the recoil velocity of the particular atom mentioned.

When lattice cooling is implemented without adiabatic release but sudden turn off instead, the results are: $\sigma_{\rm v} = 3.0\, v_{\rm r}$ for cesium, and $\sigma_{\rm v} = 3.0\, v_{\rm r}$ for sodium. However, after adiabatic release, lattice cooling yielded very different results: $\sigma_{\rm v} = 1.5\, v_{\rm r}$ for cesium, and $\sigma_{\rm v} = 3.0\, v_{\rm r}$ for sodium. This may not be surprising if we consider the following. When the atoms are released from the lattice, the original energy levels map into those of the final state, corresponding in this case to a free particle. From a simple 1D model of adiabatic release from an optical lattice [55], the expected temperature after decompression is:

$$\frac{1}{2}k_{\rm B}T = E_{\rm r}\left(\frac{Q}{k}\right)^2 \frac{1 + 4f_{\rm B} + f_{\rm B}^2}{12(1 - f_{\rm B})^2} \tag{2.3}$$

where Q is the reciprocal lattice constant, k the wave number of the light forming the lattice, and $f_{\rm B} = \exp(-\hbar\omega_0/k_{\rm B}T_0)$ is the Boltzmann factor corresponding to the initial thermal populations $\pi_n = (1 - f_{\rm B})f_{\rm B}^n$. The index n refers to the energy level in the lattice, and T_0 is the temperature of the sample before adiabatic release. In the case of counter-propagating beams $Q = \pi/\lambda$. The Boltzmann factor for sodium is $f_{\rm B} = \exp(-\hbar\omega_0/2E_{\rm r}n^2) = 0.2216$, and for cesium $f_{\rm B} = 0.0102$. The temperature of the sample prior to release is equal to $T_0 = 2(3^2E_{\rm r})/k_{\rm B}$. Substitution of these values into Eq. (2.3) yields:

$$\begin{aligned} T/T_{\rm r} &= 1.06 \quad \text{(sodium)} \\ &= 0.35 \quad \text{(cesium)}, \end{aligned}$$

which implies rms values of the velocity distribution:

$$\begin{aligned} \sigma_{\rm v}/v_{\rm r} &= 1.03 \quad \text{(sodium)} \\ &= 0.59 \quad \text{(cesium)}. \end{aligned}$$

While the observed values are: $\sigma_{\rm v}/v_{\rm r} = 3.0$ (1.5) for sodium (cesium), roughly a factor of 3 higher than expected. Such a factor may be explained due to the

limitations of the simple 1D model. The important part is that it is consistent when comparing the two experiments.

From this discussion we conclude that lattice cooling works much better in a heavy atom like cesium than in sodium. The larger mass causes the recoil frequency to be much smaller compared to the spacing between energy levels in the lattice. The Boltzmann distribution effectively puts most of the atoms in the lowest states of the lattice. Adiabatic release completes the work by mapping these levels to the very low kinetic energy levels of a free particle.

After these experiences with the vapor cell chamber we decided to abandon it in late October 2001, and move on to the next generation, which came along bringing new, unsuspected virtues and challenges.

2.5 A double MOT system in the new chamber

We started to work on the new chamber in late 2001. By mid April 2002 we had well over 10^9 atoms in the MOT, loading directly from the Zeeman slower (see Chapter 4). The scope of experiments we have in mind include the study of diffusion of ultracold atoms in aperiodic lattices, for which full optical access to large numerical aperture optics is needed. This is why we decided to implement a double MOT system prior to the most recent design. In this system a lower MOT trapped atoms directly from a high flux Zeeman slower. Once trapped and cooled, the atoms were transferred to another MOT located nearly 40 cm on top of the first one. A second MOT was chosen because it can be located in a small glass cell, with excellent optical access and the necessary proximity for magnetic trapping coils. The design also included a load-lock system, to be used later in the preparation and placement of different samples

to be probed using ultracold atoms. Our plan was to condense the atoms at the upper cell, and then move them using an optical lattice towards the location of the surfaces, a few centimeters below. Over the next months we tried several methods to maximize the transfer efficiency from one MOT into the other. We pushed to the limit all available techniques to increase the number of atoms in the upper MOT for magnetic trapping and subsequent evaporative cooling. In the end, the limitations were enough to prevent a high collision rate in the magnetic trap. At this point, we were forced to change the strategy, and design a different chamber that would allow for magnetic trapping using a single MOT, which is the subject of subsequent chapters.

In this section we give a description of the methods implemented for transferring atoms in the double MOT system, together with an analysis of their limitations. We will not describe any specifics of the chamber or the Zeeman slower, as this will be done later (Chapter 4).

2.5.1 Magnetic launch

One of the early goals within the atom optics community was the achievement of high brightness ultracold atomic beams. Several techniques were developed to create them, including moving molasses, intensity imbalance, and magnetic launching. Of these techniques, the latter resulted attractive because of its simplicity and also because it had been already demonstrated experimentally, for velocities of up to 5 m/s, in our own lab. Magnetic launch is similar in spirit to moving molasses [58], where the detuning of one or more of the beams producing a MOT is changed with time, creating an imbalance in the pressure exerted on the atoms. When a uniform magnetic field is superimposed to

laser beams in the molasses configuration, an imbalance of radiation pressure is induced by the Zeeman effect, resulting in a net force that pushes the atoms along the axis of the magnetic field (for small spatial displacements). One attractive feature of this method, shared with moving molasses, is that as the atoms are pushed in one direction they continue to cool in the perpendicular plane by the beams that are unaffected by the magnetic field. This results in atomic beams, which, at least in principle, can have velocities of few meters per second while retaining typical MOT temperatures (a few recoils).

Consider a two level system where the ground state has zero angular momentum $J = 0$, and an excited state with angular momentum $J = 1$. A uniform magnetic field lifts the degeneracies between Zeeman sublevels in the excited state. We then illuminate such an atom with two counter-propagating laser beams in the $\sigma^+ - \sigma^-$ configuration, traveling along the direction defined by the B field. For an atom with velocity v along the field direction in the lab frame, the detunings with respect to the beams will be:

$$\begin{aligned} \Delta^- &= \mu_J B/\hbar - 2\Gamma - kv \\ \Delta^+ &= -\mu_J B/\hbar - 2\Gamma + kv, \end{aligned} \tag{2.4}$$

where k is the magnitude of the wavevector of the beams. These quantities depend on the particular m_J sublevel. An atom initially placed with velocity $v = 0$ in the lab fame will acquire velocity until radiation pressure balances again, due to the Doppler shift. The velocity at which this occurs satisfies the condition:

$$\Delta^- = \Delta^+. \tag{2.5}$$

The maximum velocity $v_{\max} = \mu_J B/\hbar k$, is a limiting factor in the transfer efficiency from one MOT to the other. In reality we do not have a two level system

but the much more complicated real sodium atom. However, the analysis is illustrative, and justified by earlier studies which have found that $\sigma^+ - \sigma^-$ optical molasses in a longitudinal magnetic field stops accelerating atoms at a velocity that does not depend on the value of the ground state angular momentum [59, 60]. For estimating purposes, we can replace the magnetic moment by

$$\mu_J = \mu_B(m_{F'} g_{F'} - m_F g_F) = (3 \cdot 2/3 - 2 \cdot 1/2)\, \mu_B = \mu_B,$$

for the $3S_{1/2}(F = 2) \longrightarrow 3P_{3/2}(F' = 3)$ cycling transition of sodium. Therefore, we could expect maximum launching velocities of $v_{\max}/B = 0.82\,\mathrm{m/sG}$.

Results. We placed a coil as close as possible to the lower MOT, only a few centimeters away. With 150 turns, passing 3 A produced a field of about 25 G at the atomic position. We found 1.5 ms of launch time to be an optimum. The corresponding velocity was 7 m/s. The transfer efficiency to the upper MOT after optimization had the value of 2%.

Even though a velocity of about 7 m/s optimized the transfer, velocities up to 10 m/s were observed. It is clear that, to maximize the transfer efficiency, the atoms must be launched with the maximum velocity possible, to minimize the free expansion during the transfer time. The maximum velocity in our case is defined by the capture range of the MOT, that is, 25 m/s. We believe that maximum transfer efficiencies were found at lower launch velocities because once the magnetic field is increased further the atoms not only acquire a higher velocity but they are heated considerably as well. This effect has been observed in the magnetic launch of rubidium atoms [60]. Atoms launched at velocities greater than 6 m/s had temperatures 30 times higher than those with low velocities.

2.5.2 Continuous and pulsed resonant push

Having transfer efficiencies of 2% was unacceptable, as we were losing the vast majority of the atoms captured in the lower MOT. Another approach was taken instead, by trying to launch atoms with a resonant beam in the presence of the MOT. This is analogous to the double MOT, routinely used for rubidium in BEC machines [61]. The only difference is that we had both MOT's and the transfer region in ultrahigh vacuum environment (10^{-11} Torr). We also tried a pulsed version of this type of pushing, quite similar to the setup we had in our old double-MOT chamber [15]. At the end of many days of optimization, we discovered that the transfer efficiencies were also limited to about 2%. This, again, is in sharp contrast to the experience with rubidium. The atoms were launched with the required velocities, but the heating associated with the pushing was unavoidable. Ideally, we would like to have the scenario of the atomic fountain described in reference [61], where the atoms are pushed longitudinally, but cooled transversely during the pushing. Our vacuum chamber had several limitations to implement a 2D transversal molasses stage after the pushing (separated either in space or in time). Because of this reason, we stopped the efforts to continue using these methods.

2.5.3 On why double MOT systems work better with rubidium than sodium

In a double MOT system, atoms are pushed by radiation pressure from one MOT to the other. Let N be the number of scattering events required to impart a longitudinal velocity v to the atoms, that is $v = Nv_{\mathrm{r}}$. The associated heating in the transversal directions is $\sigma_{\mathrm{v}}^{\mathrm{heat}} = \sqrt{N}v_{\mathrm{r}}$, because it arises from a random walk distribution of scattered photons in all directions. Then, the

atoms have a velocity spread of $\sigma_{\rm v} = \sqrt{\sigma_0^2 + (\sigma_{\rm v}^{\rm heat})^2}$ after the pushing, where σ_0 is the initial rms velocity of the distribution. The figure of merit in the problem is the transversal spatial dispersion, that is $\zeta = \sigma_{\rm v}/v$. A small number for ζ will give a better transfer efficiency. If we denote by n the number of recoils of the initial distribution before pushing, we get

$$\zeta = \sqrt{n^2 + N}/N. \tag{2.6}$$

The function thus obtained monotonically decreases for increasing N. Therefore, in order to minimize it, we must put the maximum value for N possible. As we said already, this value corresponds to the capture range of the MOT. We then set $v = 20$ m/s $\sim 667\, v_{\rm r}^{\rm Na} \sim 3333\, v_{\rm r}^{\rm Rb}$. Both Rb and Na MOTs produce atoms with a typical $n = 6$. Substitution of these numbers in Eq. (2.6) yields

$$\begin{aligned} \zeta &= 0.0039 \quad \text{(sodium)} \\ &= 0.0017 \quad \text{(rubidium)}. \end{aligned}$$

A factor of $\zeta_{\rm Na}/\zeta_{\rm Rb} = 2.3$ may seem not very important. However, we must remember that this means the rms area in the transversal plane of the atomic cloud will be $2.3^2 = 5.3$ times bigger in sodium than in rubidium. If the atomic velocity distribution were uniform, we would expect a factor of 5 less transfer efficiency for sodium than rubidium. This only gives an idea of the difficulties of having a much lighter atom.

2.5.4 The lattice launch method

We implemented yet another method to load the upper MOT, using an accelerating optical lattice to create an atomic beam. This is not unreasonable,

since it is possible to tune the interaction beams far from resonance, to the point where spontaneous emission is negligible. This, of course, provided one has enough power available to obtain the necessary gradients to trap the atoms and accelerate them. In any attempt to plan the use of such accelerating lattice, a few factors of importance must be considered. First, the laser power available and the necessary spot sizes, which together with the detuning determines the well depth. Second, the required accelerations and final velocities. Finally, for a given well depth, a certain critical acceleration exists where the atoms undergo Landau-Zener tunneling into higher energy bands. Since the band gaps decrease with increasing band index, the atoms are eventually lost very soon after they leave the first band of the lattice. Therefore, care must be taken to avoid this.

Results. The optical lattice was created using the same homemade dye laser employed during the quantum transport experiments. One of the beams was frequency controlled by using an AOM in the double pass configuration to avoid transverse displacement. The resulting power in the beams after spatial filtering was about 120 mW on each beam. The beam waist used was $w_0 = 1.7$ mm, to have a uniform well depth across the atomic sample. After optimization, we set the detuning $\Delta = 2\pi\, 5.5$ GHz to the red of the trapping transition. Substitution of these numbers into Eq. (1.18), yield $V_0 = 1.2$ MHz, which is 48 times the recoil energy. The acceleration used was 20000 m/s^2, imparting a total velocity of $550\, v_\mathrm{r}$ (16.5 m/s) to the atoms. We did not go to higher velocities or accelerations due to technical problems with the frequency swept AOM, which limited the interaction times to no less than 825 μs. This was a problem, because the scattering rate due to the lattice was 14

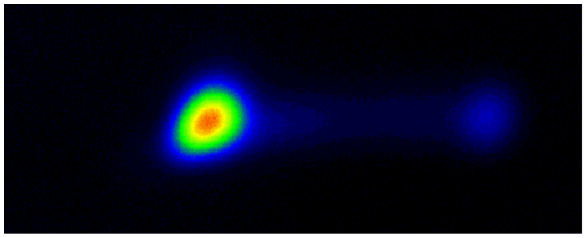

Figure 2.12: A typical atomic distribution after atoms have been dragged in an optical lattice. At the left are the atoms in a MOT, and only the small fraction at the right is being accelerated by the optical lattice. The atom number in the MOT is about 5×10^7, and the field of view is 0.7×2.2 cm.

kHz. On the average, 10 photons were spontaneously emitted by the atoms during launching, with a subsequent heating of 3 recoils in the transversal directions. As we have said before, any heating during launching imposes a serious limitation in the transfer efficiency.

Despite this problem, the method was the best we ever tried. It gave us transfer efficiencies on the order of 20%. Typical atomic distributions after dragging can be seen in Fig. 2.12. Only a small fraction of the atoms are seen to have undergone acceleration, but that is partly because they start falling on the wings of our molasses detection region. We typically loaded the lower MOT for 30 ms, apply molasses cooling and then accelerate the atoms. The upper MOT was used in the dark spot configuration, to minimize losses during transfer. With a captured flux of 10^9 atoms per second in our lower MOT, we obtained up to 6×10^8 atoms in the upper MOT after 10 s.

After several days of optimization, we decided to try magnetic trapping with those numbers. The magnetic trap used was the baseball configuration [62], limited to gradients on the order of 150 G/cm. The lifetime of the magnetically trapped atoms was above 30 s. The combination of these numbers did not lead us to runaway evaporation. This is why we decided to move to a different design for the main chamber, a subject of the next chapters.

Chapter 3

The Casimir-Polder problem

The electromagnetic interaction between atoms is at the essence of molecule formation. Similarly, the interaction of atoms or molecules with an extended array of atoms constitutes the field of surface physics. While a considerable amount of experimental research is devoted to the study of surface chemical processes, few precise measurements of the interaction potentials have been made. It is our interest to study the interaction between a conductive surface and a neutral atom in the ground state. We divide this chapter in three parts. In the first one we introduce the relevant potential. In order to gain understanding of the forces, we begin by discussing the interaction between two neutral atoms. Then, we consider the atom-wall potential using semi-classical theory. Finally, the full interaction, within the frame of quantum electrodynamics, is described. In the second part we review the current status of the Casimir-Polder experiments. The last section is devoted to the study of quantum reflection as a means to measure the atom-wall interaction.

3.1 The atom-atom van der Waals forces

The study of the interaction between an atom and a surface at distances much greater than the atomic radius began with the study of the so called van der Waals forces. These forces are responsible for many phenomena, from molecule formation to surface tension and capillarity. The systems that exhibit these

interactions include atom-atom, atom-wall, ion-molecule, molecule-molecule, etc. Because of this variety, the nomenclature for the interactions of this type is vast. We will introduce the concepts that will lead us to understand the atom-wall potential under consideration in this thesis, while making as clear as possible the resemblances and differences with related types of interaction.

Influenced by theoretical work on viscosity and capillarity from Laplace, Gauss, and Maxwell, and by experiments of Joule and Kelvin, in 1881 Johannes D. van der Waals arrived to the equation of state that bears his name [63]. The equation takes into account molecular interactions for a more realistic description of a dilute gas. For this work van der Waals received the Nobel prize in Physics in 1910, and during his acceptance speech he expressed satisfaction because the molecular point of view was not "a figment of the imagination", and the fact that his theory may have been a contributing factor for its acceptance. It must be pointed out that he did not specify the nature of the intermolecular forces, and only assumed they were attractive. In the first review paper of the van der Waals forces by Margenau [64], a definition for this type of interaction is given as: "Van der Waals force is that force which gives rise to the constant a in van der Waals equation". The mentioned equation is:

$$\left(\frac{V}{N} - b\right)\left(P + \frac{aN^2}{V^2}\right) = k_{\mathrm{B}}T, \tag{3.1}$$

where k_{B} is Boltzmann's constant, V the volume, N the number of particles, and P the pressure exerted by the gas on the confinement walls. The constant b reflects the fact that at very short distances the particles repel each other, decreasing the effective volume available. The constant a takes into account the attractive force of our concern, which effectively reduces the pressure of the gas compared to the ideal situation.

At this stage Margenau's definition of van der Waals forces is still not very precise. He then points out a very important fact: that chemical forces arising from the overlapping of electronic clouds with subsequent rearrangement due to the Pauli principle, and ionic intermolecular forces are excluded from consideration. These other forces arise directly from the Coulomb interaction of charges at very short distances, while van der Waals forces appear due to the interaction of independent *bound* systems separated by a large distance.

The exact nature of the van der Waals interaction can be seen when we consider the interaction of two hydrogen atoms in the ground state separated by a distance R. The atoms are not only neutral but spherically symmetric, so static Coulomb forces varying as $1/R$ are absent. However, in the classical picture the atom at any point in time can be thought as the electron forming an electric dipole with the nucleus, and inducing a second dipole in the other atom. The interaction between these instantaneous dipoles will give rise to the van der Waals force. It must be stressed that, even though the average dipole moment over time is zero, the instantaneous alignment (with the subsequent interaction) of the dipoles persists.

The following will be a semiclassical analysis, where the atom is quantized but the electric interaction is classical. Consider two hydrogen atoms, one at the origin and the other at $\mathbf{R}$. The separation is large, that is $R \gg a_0$, where a_0 is the Bohr radius. This condition allows to consider the energy levels of each atom as independent, and the interaction energy as a perturbation. The dipole moment of the first atom is $\mathbf{d}_1 = e\mathbf{r}_1$, and generates the electric field at the position of the second atom [65]:

$$\mathbf{E}_1(\mathbf{R}) = \frac{1}{4\pi\epsilon_0}\frac{3\hat{R}(\mathbf{d}_1 \cdot \hat{R}) - \mathbf{d}_1}{|\mathbf{R}|^3}, \tag{3.2}$$

using MKS units. The interaction potential energy is

$$\Delta V_{12} = -\mathbf{d}_2 \cdot \mathbf{E}_1(\mathbf{R}) = \frac{1}{4\pi\epsilon_0} \frac{\mathbf{d}_1 \cdot \mathbf{d}_2 - 3(\mathbf{d}_1 \cdot \hat{R})(\mathbf{d}_2 \cdot \hat{R})}{|\mathbf{R}|^3}. \tag{3.3}$$

We chose $\mathbf{R} = R\hat{z}$, so we get

$$\Delta V_{12} = \frac{e^2}{4\pi\epsilon_0} \frac{x_1 x_2 + y_1 y_2 - 2z_1 z_2}{R^3}. \tag{3.4}$$

As stated before, because the atoms are far apart, we can consider R as fixed, and treat the problem using perturbation theory. The energy of the unperturbed state is $2E_{n=1,l=0}$, and the unperturbed wavefunction is the vector product of the two wavefunctions for ground state hydrogen: $|\psi^{(1)}_{1,0,0}\psi^{(2)}_{1,0,0}\rangle$. The energy shift of the perturbed system up to second order in perturbation theory becomes:

$$\begin{aligned} \Delta E &= \langle \psi^{(1)}_{1,0,0}\psi^{(2)}_{1,0,0} | \Delta V_{12} | \psi^{(1)}_{1,0,0}\psi^{(2)}_{1,0,0} \rangle + \\ &\quad \sum_{n,l,m;n'l'm'}^{\star} \frac{|\langle \psi^{(1)}_{1,0,0}\psi^{(2)}_{1,0,0} | \Delta V_{12} | \psi^{(1)}_{n,l,m}\psi^{(2)}_{n',l',m'} \rangle|^2}{2E_{1,0} - E_{n,l,m} - E_{n'l'm'}}, \end{aligned} \tag{3.5}$$

where the star in the generalized summation indicates that the ground state is excluded. The first order correction to the energy vanishes due to the spherical symmetry of the ground state wavefunction. The second term becomes the energy shift:

$$V(R) = \left(\frac{e^2}{4\pi\epsilon_0 R^3}\right)^2 \sum_{jj'}^{\star} \frac{|\langle \psi^{(1)}_0 \psi^{(2)}_0 | (x_1 x_2 + y_1 y_2 - 2z_1 z_2) | \psi^{(1)}_j \psi^{(2)}_{j'} \rangle|^2}{2E_0 - E_j - E_{j'}}, \tag{3.6}$$

where $\{j, j'\}$ represent the indices $\{n, l, m; n', l', m'\}$. We can already see the two main characteristics of the interaction: that it is attractive, as the denominator is always negative, and that it varies as $1/R^6$. The calculation of

the sum in Eq. (6.1) involves all the excited states of hydrogen, and it is not trivial. However, an approximate answer can be obtained if one replaces the energy of the summing states with that of the first excited state $\{n = 2, l = 1\}$,

$$\begin{aligned} V(R) &\simeq \left(\frac{e^2}{4\pi\epsilon_0 R^3}\right)^2 \frac{1}{2E_{1,0} - 2E_{2,1}} \\ &\quad \times \sum_{jj'}^{\star} |\langle \psi_0^{(1)} \psi_0^{(2)} | (x_1 x_2 + y_1 y_2 - 2 z_1 z_2) | \psi_j^{(1)} \psi_{j'}^{(2)} \rangle|^2 \\ &= \left(\frac{e^2}{4\pi\epsilon_0 R^3}\right)^2 \frac{1}{2E_{1,0} - 2E_{2,1}} \\ &\quad \times \langle \psi_0^{(1)} \psi_0^{(2)} | (x_1^2 x_2^2 + y_1^2 y_2^2 + 4 z_1^2 z_2^2) | \psi_0^{(1)} \psi_0^{(2)} \rangle, \end{aligned} \tag{3.7}$$

where in the last step we have used the fact that

$$\begin{aligned} \sum_j^{\star} |\langle 0|H'|j\rangle|^2 &= \sum_j |\langle 0|H'|j\rangle|^2 - |\langle 0|H'|0\rangle|^2 \\ &= \sum_j |\langle 0|H'|j\rangle|^2, \end{aligned} \tag{3.8}$$

and the completeness relation. Finally, we can use the result $\langle x_i^2 \rangle_{00} = \langle \mathbf{r}^2 \rangle_{00}/3 = a_0^2$, to obtain

$$V(R) \simeq -8 \frac{e^2 a_0^5}{4\pi\epsilon_0 R^6}. \tag{3.9}$$

The exact evaluation of the summation in Eq. (6.1) gives the factor in front of the fraction close to 6.5 [66].

The result for the energy shift can be given in terms of the *static dipole polarizability*:

$$\alpha = \frac{2e^2}{3} \sum_{n \neq 0} \frac{|\langle \psi_n | \mathbf{r} | \psi_0 \rangle|^2}{E_n - E_0}. \tag{3.10}$$

The units for the polarizability are

$$\begin{aligned} [\alpha] &= \text{cm}^3 \quad (\text{cgs}) \\ &= a_0^3 \quad (\text{atomic units}) \\ &= \text{J}/(\text{V/m})^2 \quad (\text{SI}). \end{aligned} \tag{3.11}$$

In the case of hydrogen $\alpha = 4.50(4\pi\epsilon_0)a_0^3$ [67]. Using the natural, semiclassical frequency of the hydrogen atom:

$$\omega_H = \frac{e^2}{4\pi\epsilon_0\hbar a_0}, \tag{3.12}$$

the final form of the long range interaction is

$$V(R) = -K\frac{\hbar\omega_H}{(4\pi\epsilon_0)^2}\frac{\alpha^2}{R^6}, \tag{3.13}$$

where $K = 6.5/4.5^2$. Written like this, the equation is said to be in the London form. In 1930, Fritz London was the first to calculate formulas for the van der Waals forces, and he named the interaction between non-polar molecules the *dispersion effect*, because of the connection with the process of optical dispersion through the polarizability [68, 69, 70]. The work of London opened the field of long range interactions, and because of this the latter are often referred as London-van der Waals forces.

So far, we have presented one example of the van der Waals forces, arising through the dispersion effect, and several comments need to be made.

1. First, we must say that long range interactions between polar molecules also form part of the van der Waals group. However, we will not review this case, because is out of the scope of this research.

2. We have considered just the dipole-dipole interaction. In the London-van der Waals group all interactions of instantaneous configurations of charge, like dipole-quadrupole, quadrupole-quadrupole, etc. must be included. In this work we do not consider these configurations, due to its minimal importance compared to the dipole-dipole case [64].

3. The calculation proceeded using perturbation theory up to second order. Higher orders are not considered here. However, we must mention that retardation effects were calculated for the first time using fourth order perturbation theory in the interaction of dipole-dipole plus dipole-electromagnetic field [71, 72].

4. Lastly, the interaction is not limited to atoms in the ground state or similar atoms, of course. Atoms in excited states will interact, and all the information about the exact strength of the forces will be contained in the polarizabilities.

In order to conclude this section, it is worth mentioning the fact that almost all atoms form van der Waals molecules, with binding energies of a few meV, and bond lengths on the order of $R_0 = 0.5$ nm [73]. As we have seen, for long distances the potential is attractive, but when $R \longrightarrow 0$ Pauli repulsion between electrons and Coulomb repulsion between the nuclei dominates. This creates a potential well that helps in the formation of molecules and to describe atom-atom scattering. However, because the exact form of the repulsive part of the potential is not well known, several models are used to mimic the interaction. The Lennard-Jones potential

$$V(R) = C\left(\frac{1}{2}\left(\frac{R_0}{R}\right)^{12} - \left(\frac{R_0}{R}\right)^{6}\right) \tag{3.14}$$

is one of the most used [67]. A similar potential well exists in the atom-wall interaction.

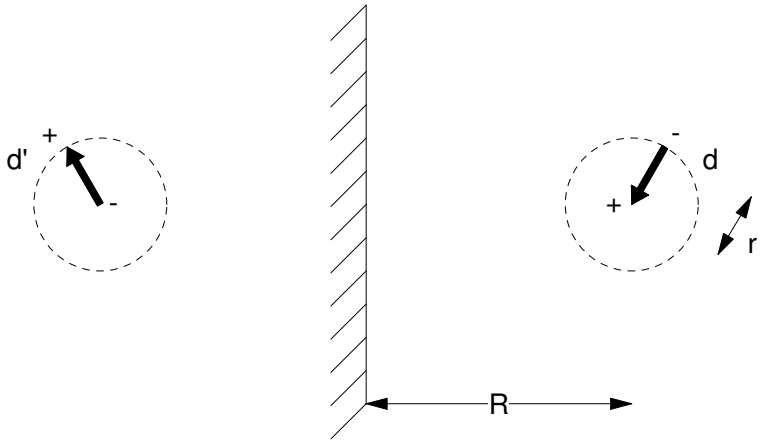

Figure 3.1: Interaction of a hydrogen atom with a metallic wall. The potential between the atom and the wall can be seen as arising from the interaction between the instantaneous atomic dipole ($\mathbf{d}$) with its image ($\mathbf{d}'$).

3.2 The atom-wall potential. Semiclassical picture

The nature of the long range interaction of an atom and a surface is very similar to that between atoms; after all it can be understood as a summation of the attraction by pairs of atoms. The approach introduced in the last section will lead us to find the form of the potential.

Consider one hydrogen atom in the ground state, interacting with a metallic wall at a distance $R \ll c/\omega_0$, where ω_0 is the frequency corresponding to the main dipole transition of the atom. This condition allows us to assume an instantaneous atom-wall interaction, neglecting the effects of the finite propagation velocity of light (retardation). As before, the atom can be seen as a rotating dipole. The instantaneous effect of the dipole interacting with the surface will be the creation of an image dipole on the surface (Fig. 3.1). It is the interaction of the atomic dipole with its image what will give rise to the van der Waals force. In a completely analogy with the atom-atom case, the atomic dipole $\mathbf{d}$ will create a field of the form given in Eq. (3.2).

This field will interact with the image dipole $\mathbf{d}'$. The key difference is now the fact that the image dipole is correlated with the original: $d'_{x,y} = -d_{x,y}$, and $d'_z = d_z$, as shown in Fig. 3.1. The interaction potential is:

$$\Delta V = -\frac{1}{2}\frac{e^2}{4\pi\epsilon_0}\frac{x^2+y^2+2z^2}{(2R)^3}, \tag{3.15}$$

where the factor of $1/2$ is included because the electric field within the conductor vanishes. The calculation for the energy shift due to this interaction can be done using first order perturbation theory. The result is

$$\Delta E = -\frac{1}{4\pi\epsilon_0}\frac{e^2}{12}\frac{\langle \mathbf{r}^2 \rangle}{R^3}. \tag{3.16}$$

In general, the formula involves the mean square displacement of the electrons of the atom or molecule. We observe that the interaction is attractive and proportional to $1/R^3$. This result was first obtained by J. E. Lennard-Jones in 1932 [74]. This is why the unretarded atom-wall potential is named after him, but it must be noted that it is often called van der Waals potential as well. In this thesis we use the term van der Waals potential, to keep in mind its semiclassical nature, and not to confuse with the Lennard-Jones potential used in scattering, Eq. (3.14).

The perfect conductivity for the metal assumed in the Lennard-Jones formula does not hold true at high frequencies, and specific properties of the material need to be considered. As pointed out by Margenau [75], the electrons in the metal rearrange themselves to form electric images of the atomic distribution of charge, but have finite relaxation times that makes hard the following of rapid fluctuations of the molecular instantaneous dipoles. A number of papers appeared to account for these effects ([75, 76] and references

therein), with the result of a weaker magnitude of the interaction force, and the explicit appearance of metal properties.

Unless explicitly stated, in the description that follows we will use atomic units (a.u.) because of convenience, and because those are the units used by theorists. The van der Waals interaction between an atom and a wall is usually written as:

$$V_{\mathrm{LJ}}(R) = -\frac{C_3}{R^3}, \tag{3.17}$$

where the coefficient C_3 is given by [77, 78]

$$C_3 = \frac{1}{4\pi}\int_0^\infty d\omega \alpha(i\omega). \tag{3.18}$$

The result depends critically on the dynamic electric dipole polarizability for the valence state under consideration $|v\rangle$, evaluated at imaginary frequencies:

$$\alpha(i\omega) = \frac{2}{3}\sum_k \frac{E_k - E_v}{(E_k - E_v)^2 + \omega^2}|\langle v|\mathbf{D}|k\rangle|^2, \tag{3.19}$$

where the dipole operator for the N electron system is $\mathbf{D} = \sum_{j=1}^{N} \mathbf{d}_j$. The calculation of the C_3 constant is clearly not an easy task; the best available value for sodium is $C_3 = 1.889$ in atomic units ($1.889\, e^2 a_0/4\pi\epsilon_0$ in SI units) [79]. In the case of an atom interacting with a dielectric material with index of refraction n, the C_3 constant is related to the metal case by the relation [80]

$$C_3^{(n)} = \frac{n^2 - 1}{n^2 + 1} C_3^{\mathrm{metal}}. \tag{3.20}$$

Finally, it is important to mention that similar to the atom-atom interaction, the atom-wall potential becomes repulsive at very short distances (on the order of a few Bohr radii). The combined potential has therefore a minimum, and gives rise to *physisorption* [81, 82]. This phenomenon consists in the adsorption

of a molecule by a surface, where there is no chemical bonding. The binding energies are on the order of the depth of the potential, a few meV. In our experiment for quantum reflection the atoms reflect from the tail of the atom-wall potential, far away from the surface, therefore making the process of physisorption unimportant.

3.3 The Casimir-Polder potential

We have limited the discussion to long-range or dispersion forces, where the atom and the wall are separated by a distance R much larger than the atomic radius, but small enough so that instantaneous interaction can be assumed. We now discuss the case when this is not longer true. The first question that arises is at which distance retardation effects are important. For an atom at a distance R from the wall, its emitted light at energy $\Delta E = \hbar\omega_0$ will reach the wall in a time $\Delta t = R/c$, where c is the speed of light. Now, according to standard quantum mechanics "the state ket of a physical system ceases to retain its original form after a time interval of order $\hbar/\Delta E$" [24]. In our case, after a time of order $1/\omega_0$ the fluctuating dipole will no longer be the same, and it may change before light carrying information about its previous condition reaches the wall. The equation $1/\omega_0 = \Delta t$, yields the distance at which retardation effects become relevant:

$$R \simeq \frac{\lambda_0}{2\pi}, \tag{3.21}$$

where λ_0 is the wavelength of the main dipole transition. The reason to consider dipole transitions is that they are the main contributions to the polarizability. In the case of sodium, for example, the major contribution for the

excitation of the valence $3s$ electron is the resonance $3s - 3p$ transition, which has an oscillator strength of 0.962 [79].

The proper treatment of retardation effects abandons the semiclassical picture to adopt the methods of Quantum Electrodynamics (QED). The first to derive the correct form of the atom-wall, and atom-atom potentials were H. B. G. Casimir and D. Polder in a paper of 1948 [83]. Previously in that same year, Casimir had predicted the famous result on the attraction of two parallel metal plates [71]. The Casimir effect has received a lot of attention, because it is a non-intuitive consequence of vacuum fluctuations [84]. It is worth writing the Casimir force per unit area of two conducting parallel plates separated at a distance R:

$$F(R)/A = \frac{\pi^2}{240}\frac{\hbar c}{R^4} \quad (\text{SI units}), \tag{3.22}$$

and noting the fact that only fundamental constants are present. There is no coupling of matter with the electromagnetic field, as the electron charge e is absent. Recently, this interaction has been measured in the 0.6 to 6 μm range [85, 86].

Casimir and Polder calculated the interaction potential between a neutral atom and a perfectly conducting plate by considering the interaction of the atom with its image, and with the electromagnetic modes of the vacuum as they are modified by the presence of the wall. The calculation is not straightforward, and the reader is directed to the full calculations of references [71, 72]. The final result recovers the potential of Eq. (3.17) for short distances. On the other hand, for large distances the potential behaves like

$$V_{\text{CP}}(R) \simeq -\frac{C_4}{R^4}. \tag{3.23}$$

The constant C_4 is equal to

$$\begin{aligned} C_4 &= 3\frac{\alpha(0)}{8\pi\alpha_{\rm fs}} = 16.36\,\alpha(0) \quad \text{(atomic units)} \\ &= 3\frac{\hbar c\alpha(0)}{32\pi^2\epsilon_0} \quad \text{(SI units)}, \end{aligned} \tag{3.24}$$

where $\alpha(0)$ is the static dipole polarizability, Eq. (3.10), and $\alpha_{\rm fs}$ the fine structure constant. The static dipole polarizabilities have been calculated for almost all the alkali-metal elements [87]. In the case of sodium, the best calculation reports $\alpha(0) = 162.6(3)$ a.u. [78], while the measured value by Pritchard and coworkers using an interferometric method is $\alpha(0) = 162.7(5)$ a.u. [88]. Therefore, the C_4 constant in the case of sodium is

$$C_4 = 2661(9), \tag{3.25}$$

in atomic units.

It is interesting to note that, as pointed out in references [89, 90], the long range behavior of the potential can be recovered using a simple reasoning. In the presence of the wall, the electromagnetic modes of the vacuum are modified, especially those with wavelengths large compared to the atom-wall distance. Now, for a given mode of the field there is an interaction energy of the atom with the field given by $-\alpha{\mathcal{E}_\omega}^2/2$, where $\mathcal{E}_\omega$ is the magnitude of the electric field at frequency ω. The static polarizability is used, as deviations from perfect conductivity arise only beyond the visible range of frequencies. Then, the contribution for each mode is added:

$$V(R) \simeq -2 \sum_{\omega<c/R} \alpha{\mathcal{E}_\omega}^2/2, \tag{3.26}$$

where the factor of two takes into account the two possible polarizations of the field. The electric field of each mode enclosed in a box of volume L^3 is

given by $\mathcal{E}_\omega = (\hbar\omega/2\epsilon_0 L^3)^{1/2}$, in SI units [91]. The sum is over the density of photon states becomes

$$\sum_\omega \longrightarrow \sum_{\epsilon=1}^{2} \int \frac{L^3\omega^2 d\omega d\Omega}{(2\pi c)^3}.$$

The result is

$$\begin{aligned} V(R) &= -\frac{\alpha\hbar}{4\pi^2\epsilon_0 c^3}\int_0^{c/R} \omega^3 d\omega \\ &= -\frac{1}{16\pi^2\epsilon_0}\frac{\hbar c\alpha}{R^4}, \end{aligned} \tag{3.27}$$

which is very close to the exact value given in Eq. (3.24). It can be shown that the potential of Eq. (3.23) is the result of the atom driven by the altered structure of the modes of the vacuum (vacuum fluctuations), as opposed to the reaction of the atom to its own field [92].

To conclude this section, we must note that the expressions for the interaction potential given by Eqs. (3.17), and (3.23) represent the limiting behavior of the Casimir-Polder potential for short and long distances, respectively. There is no analytical formula for the potential in the intermediate region, and numerical values have to be calculated using various methods. We will use these values when we calculate the reflection probability for sodium atoms incident on conductive surfaces. Only approximate analytical expressions for the full Casimir-Polder potential exist, and one of the most used is given by [93]

$$V_{\rm CP}(R) = V_{\rm QED}(R) \simeq -\frac{C_4}{R^3(R+R_0)}, \tag{3.28}$$

where the value R_0 is close to $3\lambda_0/2\pi^2$ [83].

3.4 A review of experimental progress

While an experimental demonstration of the Casimir Polder effect has been realized, a precise measurement of the atom-wall interaction is still needed. The best work in this direction was done by the Yale group, who observed a match between experimental data and the QED prediction with 10% confidence level. The impressive advances in the field of atomic laser trapping and cooling enabled the observation of quantum reflection at grazing incidence, and recently perpendicular to the surface. In none of these cases however, the precision of the experimental technique allowed a good comparison with the QED predictions. Specially true for the paper on reflection at normal incidence, the results are more qualitative than quantitative. It is our purpose to push the experimental techniques available to date to obtain a precision on the level of .1% for the quantum reflection probability. This will not only allow good comparison with the theory but open up additional possibilities for a possible application of the Casimir-Polder interaction.

3.4.1 Hydrogen on helium

Initially, studies were performed to characterize the properties of thin film liquid helium [94]. The first series of experiments that reported observation of quantum reflection were done by reflecting grazing incidence atomic ^{4}He on a thin film of superfluid ^{4}He [95]. Reflection probabilities up to 20% were observed, with incident atoms whose de Broglie wavelength associated with its normal momentum was about 10 nm. Later, by using a concave mirror, normal incidence reflection of H on liquid helium was observed [96]. Also, a strong influence of the substrate supporting the thin He film was reported for incident

atoms as cold as 300 μK (corresponding to a de Broglie wavelength of 100 nm) [97]. Even though an influence of the Casimir-Van der Waals potential was observed, no quantitative measurement of the potential could be made. The main sources of uncertainty in these experiments are: the determination of film thickness, specific characteristics of the substrate where the liquid helium film is deposited, and inelastic scattering processes taking place at the surface (ripplons) [96].

3.4.2 The Yale experiment

The first observation of reflection of a thermal beam from a surface at room temperature was done by the group of Ed Hinds [98]. In order to measure the Casimir-Polder interaction, moving from liquid helium to a room temperature surface has many clear advantages. This was the first step in a series of experiments in the same group that culminated with the measurement of the van der Waals [99], and Casimir-Polder [100] interactions between a free atom and a macroscopic surface.

In the case of the Casimir-Polder measurement a thermal beam from an effusive oven was sent through the space of a cavity. The cavity consisted of two glass substrates coated with a 42 nm thick layer of gold, and the separation ranged from 7.5 μm down to 0.75 μm. The gradient in the potential energy between the atom (sodium) in the ground state and the walls of the cavity deflects the atoms towards the walls. With the knowledge of the geometry of both cavity and incoming atomic beam it is possible to calculate the expected transmission of atoms through the cavity. The measured quantity is therefore the number of atoms transmitted as a function of cavity width.

Recalling the condition for the distance atom-wall z to observe retardation effects:

$$z = \frac{1}{2\pi}\lambda_0 \simeq 94\,\mathrm{nm}, \tag{3.29}$$

would indicate that the interaction in this experiment would be dominated by the Casimir-Polder potential, varying as $\sim -1/z^4$. For large wall separations, however, the force was small, and only below 1 μm separation a clear agreement between the data points and the predicted QED curve was seen. The authors considered several systematic effects, including background counts, gradients in stray electric fields, and imperfect reflectivity of the gold surface for wavelengths smaller than the cavity width. The result was an agreement between experimental data and the QED prediction at the level of 10%. This constitutes the best measurement of the force between an atom and a surface so far.

3.4.3 Cold atoms on a prism

In the field of atom optics two experiments have observed qualitatively the effects of van der Waals forces in the interaction atom-surface. The first one was by the group of Steven Chu [101]. Atoms in an atomic fountain were launched towards the surface of a BK-7 prism. The prism supported an evanescent wave with blue detuned light. The light created an exponentially decaying repulsive potential, which added to the attractive van der Waals interaction formed a potential barrier. Incident velocities used were on the order of 3.0 ± 0.5 cm/s, the velocity selection being done with collimating slits. What was measured was the number of atoms reflected as a function of the barrier height. Instead of a sharp threshold at the barrier height corresponding to the incident veloc-

ity of the atoms, a smooth function was observed. This indicates above the barrier reflection, a pure quantum effect. The atoms came as close as 200 nm from the surface, and in principle is possible to expect an influence of retardation effects. However, this experiment was only a qualitative demonstration, and was not pursued further.

The second experiment that worked along a similar direction was done by the Orsay group [102]. Rubidium atoms from a MOT were dropped a distance of 15 mm before they hit the surface of a glass prism where a repulsive evanescent wave was present. The reasoning was similar to that of Chu's experiment, but the goal was a quantitative measure of the van der Waals interaction between the atom and the dielectric. At the time the atoms reached the surface they had acquired a velocity of 54 cm/s, which corresponds to a de Broglie wavelength of 8.7 nm. Typical barrier widths used were on the order of 125 nm, therefore barring above the barrier reflection. Also, while retardation effects changed the barrier height by 10%, it was not possible to distinguish clearly a change in the threshold as the experimental uncertainties were more than 10%.

An experiment of the type of the two works discussed above presents many challenges that make very difficult a precision measurement (better than 1%). The introduction of an evanescent wave introduces a big source of error as the power cannot be calibrated better than 10% easily. The use of a gaussian beam for the repulsive potential presents a threshold that changes as a function of position. Also, the use of MOT atoms precludes monochromaticity, and averaging has to be performed. Finally, in a dielectric charge may build up, and electric fields are of serious concern (this is different than the process

considered in [103], where adsorbed atoms create the electric field).

3.4.4 Shimizu's experiment

Quantum reflection of atoms incident on a surface at room temperature was observed for the first time by Shimizu [93]. The atom used was metastable neon coming from a MOT, and the surfaces used included glass and silicon. In quantum reflection the necessary incident velocities are extremely small, and so the keys of this experiment were the velocity selection and the detection scheme. Atoms from the MOT were released, and 37 cm below, the transversal velocity selection was done by a collimating hole 100 μm in diameter. A highly monochromatic beam was obtained this way (transversal spread of less than 1 mm/s). The atoms then were sent towards a surface at grazing incidence, and by changing the angle normal incident velocities ($v_{\rm n}$) between 1 mm/s and 3 cm/s were obtained. Finally, as the atoms reflected from the purely attractive potential they were detected using a micro channel plate.

This experiment is very significant in that quantum reflection was observed for the first time using ultracold atoms, and that reflectivities up to 30% were observed at $v_{\rm n} = 1$ mm/s. On the other hand, the experimental statistical error was between 20% and 50%. In any case, a semi-qualitative description of the data that included the Casimir-Polder potential was given. The data was fitted to the function:

$$U_{\rm int}(z) = -\frac{C_4}{(z + \lambda/2\pi)z^3}, \tag{3.30}$$

which incorporates the correct behavior for both long and short distances (compared to $\lambda/2\pi$). The qualitative agreement was very good, which definitively shows retardation effects responsible for the measured reflectivities. However,

a precise measurement of the potential is not feasible in this system, specially at high incident velocities. Because the atom is in a metastable state it cannot get very close to the surface before it decays to the ground state.

After the demonstration of quantum reflection, a similar system was used by the same group to observe reflectivities up to 60% [104], and for the realization of gratings and a hologram mask for matter waves [105, 106].

3.4.5 Recent developments

Recently, two more experiments have reported the observation of quantum reflection from a purely attractive atom-wall potential. While these demonstrations achieve reflectivities that match with the expected calculations, they do not constitute a precise determination of the Casimir-Polder interaction potential.

1. The experiment of V. Druzhinina and M. DeKieviet

In this experiment, neutral helium atoms were scattered form an α-quartz crystalline surface at grazing incidence [107]. The maximum reflectivities reported are of a few percent. The parameters used for the atomic beam incident on the surface are such that observed the reflected atoms are due the interaction with the van der Waals potential far from threshold $E_i \longrightarrow 0$. The condition of relatively high incident energies is precisely determined by $E_i \gg C_3^4/C_4^3$. The significance of using these incident energies is that atoms will get close to the surface before they are reflected. The reflected signal is thus sensitive not only to the tail of the potential, as in Shimizu's experiment, but to details of the interaction at short distances. It is interesting to compare the parameters

used in that experiment:

$$\left(\frac{C_3^4}{C_4^3}\right)^{\text{He-quartz}} = 2.4 \times 10^{-9}\,\text{eV}$$
$$E_i = 6.9 \times 10^{-6} - 1.4 \times 10^{-8}\,\text{eV} \quad (3.31)$$

with our own system:

$$\left(\frac{C_3^4}{C_4^3}\right)^{\text{Na-metal}} = 6.9 \times 10^{-12}\,\text{eV}$$
$$E_i = 2.7 \times 10^{-11} - 1.1 \times 10^{-12}\,\text{eV}. \quad (3.32)$$

Incident energies in our case correspond to velocities ranging from 1.5 cm/s to 3 mm/s. We distinguish clearly the regime under which the experiment was performed, that is, quantum reflection at 'high energies'. The obtained results were quantitative, and were sensitive enough to probe some predicted characteristics of the He-quartz potential at short distances. However, a number of effects had to be taken into account, mainly related to the roughness of the quartz surface. In reflection from potential tails this is not critical, but for large incident energies this affects not only the specularity but the reflection probability as well.

Finally, a fit to the corrected data was performed using for the potential

$$V(z) = -\frac{C_4}{z^3(z+l)}, \quad (3.33)$$

with the transition length l as a fitting parameter. The result gave $l = 10 \pm 1$ nm, which is close to $\lambda/2\pi = 9.3$ nm, corresponding to the atomic transition between the ground state and the first excited state of helium.

2. The MIT experiment

The MIT group recently reported an experiment which is related to ours, using a completely different technique [108]. Sodium atoms forming a BEC were trapped in a weak gravito-magnetic trap near a silicon surface. At this point dipole oscillations of the BEC cloud inside the trap were induced, as the minimum of the trap moved suddenly to be at the surface. This imparted to the atoms the necessary incident velocity towards the surface, and it was varied between 1 and 8 mm/s. The atomic cloud remained trapped before, during, and after the scattering with the surface. Reflectivities as high as 20% were observed.

This experiment constitutes a qualitative demonstration of retardation effects using atoms at normal incidence, as opposed to previous experiments which used grazing incidence to achieve the required (normal) incident velocities necessary to observe reflection. Because of the qualitative nature of the work, many details were left aside, like the effect of electric field gradients created by the adsorbed atoms on the surface [103]. The effect of the trap on the reflectivity is ignored, and the data does not fit very well to the calculation using a potential of the type Eq. (3.33), especially for incident velocities below 3 mm/s.

3.5 Quantum Reflection

The atom-wall interaction can be determined by scattering atoms from the surface, and looking for an effect due to a mechanical force experienced by the atoms. In the past, experiments have seen deviations in the trajectory of an atomic beam as it passes close to a surface [82]. We chose to measure the interaction by means of *quantum reflection* [80], which is an effect occurring

for atoms incident at very small energies.

3.5.1 The reflection effect

An atom of mass M incident on a surface at normal velocity v_i will experience the attractive potential $V(x)$ and accelerate towards the wall. If the incident kinetic energy is large the atom will follow a classical trajectory and interact with the surface at very short distances. However, for very small incident velocities the picture changes. The atoms can be reflected when the variation of the de Broglie wavelength ($\lambda_{\rm dB}$) over distance is large, as the atom moves along the potential. Clearly, a rapidly varying potential increases the probability for reflection. This effect is of purely quantum nature, as there are no classical turning points involved.

The condition for quantum reflection is

$$\frac{d\lambda_{\rm dB}(x)}{dx} \geq 1, \tag{3.34}$$

where $\lambda_{\rm dB}(x) = h/(2M(E_i - V(x)))^{1/2}$, and the incident energy is $E_i = Mv_i^2/2$. This is the condition where a semiclassical analysis fails, and we will extend the discussion when we calculate the reflection probability. The case of homogeneous potential tails ($V_\alpha(x) = -C_\alpha/x^\alpha$) is relevant, as it is the form the Casimir-Polder potential takes in the short and long distance limits. The variation of the de Broglie wavelength under such potential reaches a maximum at a distance

$$x_\alpha = \left(\frac{C_\alpha(\alpha-2)}{2E_i(\alpha+1)}\right)^{1/\alpha}. \tag{3.35}$$

To have an idea of the distance scale, we consider the Casimir-Polder potential in the retarded limit. For sodium atoms incident at $v_i = 1$ cm/s, the reflection

distance is equal to $x_4 = 628$ nm. If one uses the Lennard-Jones limit instead, the distance is a little less: $x_3 = 430$ nm.

The reflection probability $|R|^2$ has the characteristic of always approaching unity as the incident velocity goes to zero, for potentials falling faster than $1/x^2$. The reflection amplitude has the behavior [109]:

$$|R|_{v_i \to 0} \sim 1 - 2kb, \tag{3.36}$$

where k is the asymptotic wavevector of the incident particle ($k = mv_i/\hbar$). The distance b is a parameter that depends only on the potential beyond the point x_α. Its value for the corresponding short and long ranges is:

$$\begin{aligned} b_3 &= \pi \frac{2M}{\hbar^2} C_3, \quad \text{and} \\ b_4 &= \left(\frac{2M}{\hbar^2} C_4 \right)^{1/2}. \end{aligned} \tag{3.37}$$

The authors of reference [109] point out that the behavior of Eq. (3.38) can also be written as

$$|R|_{v_i \to 0} \sim \exp(-2bk), \tag{3.38}$$

for a number of potentials, including homogeneous tails. As we proceed in the calculation of the reflection probability we will check the validity of the formula.

3.6 Calculation of the reflection probability

Analytical solutions to problems of scattering is limited to a number of potentials. Approximate methods therefore must be used, and the Wentzel-Kramers-Brillouin (WKB) approximation is one of the most powerful methods

available. However, the WKB method is not accurate for rapidly varying potentials or small de Broglie wavelengths. A numerical solution therefore must be found. In the case of quantum reflection, we calculate the probabilities for reflection using a method described in reference [110]. In this chapter we will use atomic units.

3.6.1 The method

We begin our discussion by recalling the WKB approximation: under the influence of potential $V(x)$, the wave function of a particle of mass M that satisfies the Schrödinger equation can be approximated by

$$\psi(x) \simeq \frac{1}{\sqrt{k(x)}} \exp\left(\pm i \int^x k(x')dx'\right), \tag{3.39}$$

where the particle wavenumber is given by $k(x) = \sqrt{2M(E - V(x))}/\hbar$. The approximation is valid only if the de Broglie wavelength $\lambda_{\rm dB} = 2\pi/k(x)$ varies slowly:

$$\frac{1}{2\pi}\left|\frac{d\lambda_{\rm dB}}{dx}\right| \ll 1. \tag{3.40}$$

Regions of space where the condition of Eq. (3.40) is violated are known as *badlands*. In the case of atomic reflection form surfaces, the badlands appear around 100 nanometers away from the surface. The reflection amplitude can be found by using a numerical answer inside the badlands, and a WKB approximation away from them. The solutions are then matched at some point x_m, and from the matching conditions the reflection coefficient can be calculated.

The van der Waals or Casimir potentials are valid for distances down to a few tens of angstroms away from the surface. At closer distances the electronic interaction of the atom with the lattice is repulsive. Also, there

are adsorption processes with possible chemical reactions. This cannot be accounted for in our calculations, and it does not need to, as the atom is reflected at distances of hundreds of angstroms away from the surface. The atoms that are not reflected will eventually get close to the surface and participate in some adsorption process. In order to calculate the probability for quantum reflection, it is enough to know the tail of the potential. With this in mind, the calculation reduces to the problem of reflection above a potential step [110].

We consider a particle incoming from $x \to -\infty$ with kinetic energy $\hbar^2 k_1^2/2M$, that interacts with the potential step $V(x)$. The potential is taken to have a constant negative value $-V_0 = -(k_1^2 - k_2^2)\hbar^2/2M$ for $x \to -\infty$, and to vanish at $x \to \infty$. Upon transmission, the particle has kinetic energy $\hbar^2 k_2^2/2M = E$. We must note that the particle is incident from the left ($x \to -\infty$), and that the potential under test is relevant only for $x > 0$. This is just for calculation purposes. The reflection probability calculated this way is the same as for a particle incident from $x \to \infty$, by the reciprocity principle (a discussion on this subject can be found in reference [23], p. 506). The WKB approximation for $x \leq x_m$ is:

$$\psi(x) = \frac{1}{\sqrt{k(x)}} \left[\exp\left(i \int_{x_m}^{x} k(x')dx' \right) + R_{\mathrm{WKB}} \exp\left(-i \int_{x_m}^{x} k(x')dx' \right) \right]. \tag{3.41}$$

At $x \to -\infty$ the wave function is proportional to $\exp(ik_1 x) + R\exp(-ik_1 x)$. The conventional reflection amplitude R differs from R_{WKB} up to a phase factor. On the other hand, for $x \to +\infty$ the wave function is $\psi_o \propto \exp(ik_2 x)$. For finite, positive x satisfying Eq. (3.40), an accurate solution can be found that corresponds to ψ_o in the $x \to +\infty$ limit. The coefficient R_{WKB} is obtained by matching the logarithmic derivatives of both the WKB solution, Eq. (3.41),

and the exact solution (numerically calculated) at the point x_m. The procedure gives

$$R_{\rm WKB} = -\frac{z - ik(x_m) + k'(x_m)/2k(x_m)}{z + ik(x_m) + k'(x_m)/2k(x_m)}, \tag{3.42}$$

where $z = \psi'(x_m)/\psi(x_m)$.

3.6.2 Solution in the van der Waals limit

We start by writing the outgoing wave function at $x \to +\infty$: $\psi_o = \exp(ik_2 x)$, using an arbitrary phase. This function is taken as the initial condition for the solution of the Schrödinger equation. Once the solution is propagated numerically up to the point x_m, the logarithmic derivative is calculated and the reflection probability obtained, $|R|^2 = |R_{\rm WKB}|^2$. We observe then the behavior of $|R|^2$ as a function of x_m, and look for a convergent value.

Because we are interested in calculating the real number $|R|^2$, we can put it in terms of the real an imaginary parts of the exact wave function $\psi(x) = \psi_R(x) + \psi_I(x)$, and its derivatives. The result is:

$$|R|^2 = \frac{(a + k'(x_m)/2k(x_m))^2 + (b - k(x_m))^2}{(a + k'(x_m)/2k(x_m))^2 + (b + k(x_m))^2}, \tag{3.43}$$

where

$$\begin{aligned} a &= \frac{\psi_R' \psi_R + \psi_I' \psi_I}{\psi_R^2 + \psi_I^2} \\ b &= \frac{\psi_R \psi_I' - \psi_I \psi_R'}{\psi_R^2 + \psi_I^2} \end{aligned} \tag{3.44}$$

are to be evaluated at x_m.

To perform the computation we consider a potential that behaves for $x \to +\infty$ asymptotically as:

$$V_\alpha(x) = -\frac{\hbar^2}{2M}\frac{\beta^{\alpha-2}}{x^\alpha}. \tag{3.45}$$

The wavevector becomes:

$$k(x) = \sqrt{k_2^2 + \frac{\beta^{\alpha-2}}{x^\alpha}}. \tag{3.46}$$

We can transform to dimensionless variables by scaling in terms of the natural unit of length β,

$$k(x) = \sqrt{\kappa^2 + \frac{1}{x^\alpha}}, \tag{3.47}$$

where $\kappa = k_2\beta$. The logarithmic derivative of the wave vector becomes

$$\frac{1}{k}\frac{dk}{dx} = -\frac{\alpha}{2}\frac{1}{\kappa^2 + 1/x^\alpha}\frac{1}{x^{\alpha+1}}. \tag{3.48}$$

In the case of a sodium atom in the ground state and a metal surface the potential is:

$$V_{\mathrm{vdW}}(x) = -\frac{C_3}{x^3}. \tag{3.49}$$

with the constant $C_3 = 1.8858$ [78, 79, 111]. Therefore, the unit of length becomes:

$$\beta = C_3\frac{2M}{\hbar^2} = 1.8858 \times 2\frac{M}{m_e}\,a_0 = 1.5829 \times 10^5\,a_0, \tag{3.50}$$

or a distance of about 8.4 μm. The most important parameter of the reflection problem is the incident velocity, that is $v_i = \hbar k_2/M$. Because the relevant range of incident velocities goes from a few mm/s up to a few cm/s, we calculate the variable κ to be

$$\kappa(v) = k_2\beta = 30.322\,v_i, \tag{3.51}$$

where v_i is in cm/s.

Finally, for computation purposes, the Schrödinger equation is needed in dimensionless form:

$$\frac{d^2\psi}{dx^2} + \left[\frac{1}{x^\alpha} + \kappa^2\right]\psi = 0. \tag{3.52}$$

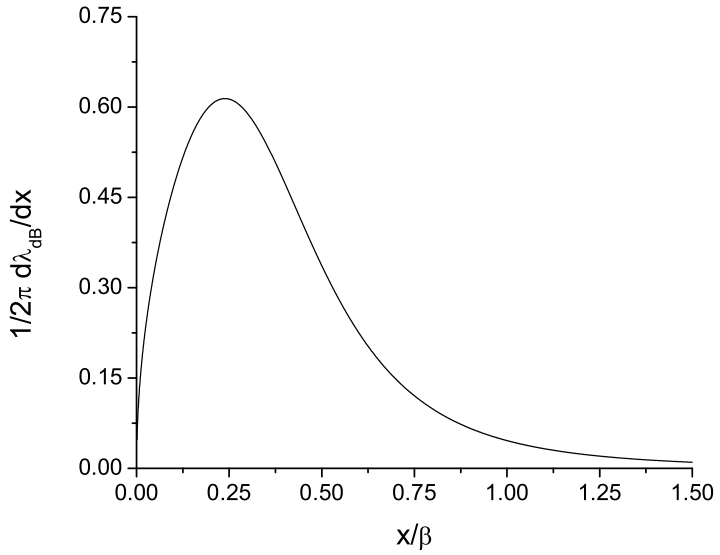

Figure 3.2: The change of the de Broglie wavelength, $\frac{1}{2\pi} d\lambda_{\rm dB}/dx$, as the particle travels along the potential. Positions for which the function is close to or larger than 1 defines the badlands. The incident velocity is 1 mm/s.

Equation (3.52) is solved numerically using a fourth order Runge-Kutta algorithm [112]. The initial condition is taken to be $\Psi_0 = \exp(ik_2 x_0) = \exp(i\kappa(v_i)x_0)$, where $x_0 = 3.5$, which corresponds to 29 μm.

The results of the calculation for a particle incident on the surface with a velocity of 1 mm/s are shown in Figs. 3.3 through 3.4. First, in Fig. 3.2 we show the behavior of the rate of change for de Broglie wavelength:

$$\frac{1}{2\pi}\left|\frac{d\lambda_{\rm dB}}{dx}\right| = \frac{3}{2}\frac{1}{(\kappa^2 + 1/x^3)^{3/2}}\frac{1}{x^4}. \tag{3.53}$$

As the atom approaches the steeper part of the potential condition Eq. (3.40) is not fully satisfied. The badlands in this case occur at distances around $(x = 0.25\,\beta)$.

The behavior of the wave function as it approaches small distances is

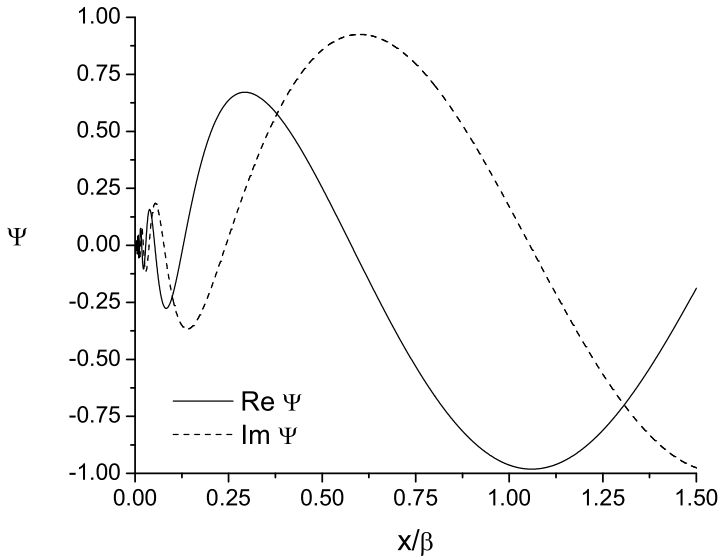

Figure 3.3: The real and imaginary parts of the incident wave function as a function of distance. Note the dramatic change as the particle approaches the badlands. The incident velocity is 1 mm/s.

shown in Fig. 3.3. The wavelength decreases in a rapid variation, as the kinetic energy increases. However, it is still possible to calculate the probability of reflection. Figure 3.4 shows the behavior of $|R_{\mathrm{WKB}}|^2$, as it changes dramatically from zero as it crosses the badlands, but it manages to converge where the condition of Eq. (3.40) is valid again.

The convergent values of $|R_{\mathrm{WKB}}|^2$ for very small distances are taken to construct the plot of reflection probability as a function of incident velocity, Fig. 3.6. The reflection probability approaches 1 as the velocity tends to zero, but it decreases very rapidly. For a velocity of 1 mm/s the reflection probability is already 0.3%. The situation improves by many orders of magnitude when retardation effects are taken into account, as we will see shortly.

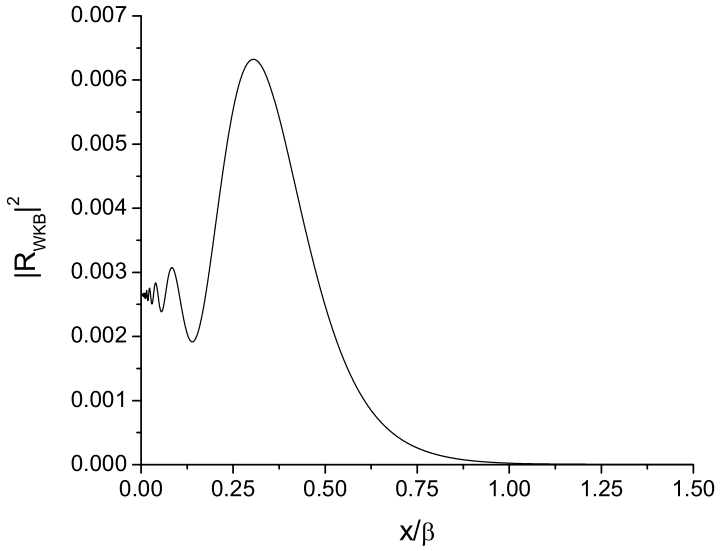

Figure 3.4: The evolution of the WKB reflection probability as the particle approaches the surface. It is interesting to note the convergence to a definite value (in this case 0.00264), when the region of badlands is left behind. The incident velocity is 1 mm/s.

3.6.3 Solution for the Casimir-Polder potential

An exact analytical formula for the full QED, Casimir-van der Waals potential is not known yet. Marinescu and coworkers have calculated numerical values for the potential in a range that is useful for determining the probability of reflection (between $1 - 10^6\, a_0$) for a number alkalis [87]. A more recent calculation for the potential was done by Kharchenko *et. al.* [79], which has a good agreement with the most recent calculations of the C_3 constant by Derevianko and coworkers [78]. After analyzing the information of reference [87], Friedrich and coworkers have found a rational approximation to the potential that reproduces the potential within a maximum relative error of 0.6% [109]. They write the full QED potential as

$$V_{\mathrm{QED}}(r) = \frac{\hbar^2 K_0^2}{2M} v\left(\frac{r}{l}\right), \tag{3.54}$$

where the fitting function is

$$v(x) = -\frac{1}{x^3}\left(\frac{1+\zeta x}{1+\eta x+\zeta x^2}\right). \tag{3.55}$$

In the Casimir-Polder potential there is an energy independent unit of intrinsic length

$$l = \frac{C_4}{C_3}. \tag{3.56}$$

The value for the C constant in the retarded potential limit is $C_4 = 2661$, see Eq. (3.25); while for short distances Friedrich and coworkers use $C_3 = 1.5753$. The fitting function Eq. (3.55) has the following parameters for the calculated potential of reference [87]:

$$\begin{aligned} l &= 1.6895 \times 10^3\, a_0 \\ \zeta &= 0.35 \\ \eta &= 0.98. \end{aligned} \tag{3.57}$$

Using the most accurate value of $C_3 = 1.8858$, yields $l = 1.4113 \times 10^3\, a_0$. It is worth noticing that this distance is equal to 75 nm, a value very close to $\lambda/2\pi = 94$ nm, that signals the transition between the van der Waals limit and the retarded potential.

To perform our computation for the reflectivity we will use the more recently calculated potential given in reference [79], as opposed to that of [87]. In order to compare to our previous van der Waals calculation, we will keep as our unit of length the parameter β, defined in Eq. (3.47). We write the potential as:

$$V_{\rm QED}(x) = -\frac{\hbar^2\beta^{-2}}{2M}\frac{1}{x^3}\,u(x/\beta). \tag{3.58}$$

The fitting function is now

$$u(x) = C\left(\frac{1+\zeta' x}{1+\eta' x+\zeta'' x^2}\right), \tag{3.59}$$

where the fitting constants are

$$\begin{aligned} \zeta' &= 5.94 \\ \eta' &= 84.1 \\ \zeta'' &= 666 \\ C &= 0.897. \end{aligned} \tag{3.60}$$

The datapoints calculated in reference [79] for the Casimir-Polder potential are shown in Fig. 3.5, together with the fitting function. The fit has a maximum relative deviation of 1.8% in the range $x = 100 - 30000\, a_0$. For values of x between $30000 - 10^6\, a_0$, the deviations increase to a level of up to 9%. However, we believe this is not a serious problem, as the potential does not have any badlands beyond $x \sim 10^5\, a_0 = 5.3\,\mu$m for the incident velocities considered in

the calculation (no less than 1 mm/s). We must mention that fittings of the form described by Eq. (3.28) were tried but they performed worse than what is presented here.

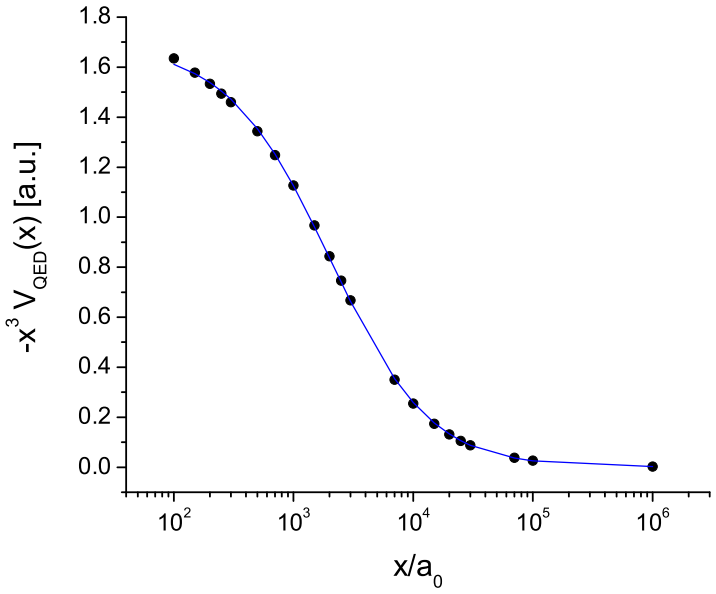

Figure 3.5: Results of the fit to the calculated QED potential between a sodium atom and a metallic wall (reference [79]). The fit was performed over the region relevant for quantum reflection. The average relative deviation from the calculated potential is 0.8% in the region $x = 100 - 3 \times 10^4\, a_0$.

With the potential set this way the procedure that follows is almost identical to the one carried out for the homogeneous van der Waals case, as the only difference is the term $u(x)$ in Eq. (3.58). For example, the Schrödinger equation in dimensionless form is analogous to Equation 3.52:

$$\frac{d^2\psi}{dx^2} + \left[\frac{1}{x^3}u(x) + \kappa^2\right]\psi = 0. \tag{3.61}$$

Finally, we give the form for the wave vector

$$k(x) = \sqrt{\kappa^2 + \frac{1}{x^3}u(x)}, \tag{3.62}$$

and its logarithmic derivative:

$$\frac{1}{k}\frac{dk}{dx} = \frac{1}{2}\frac{1}{\kappa^2 + (1/x^3)u(x)}\left(\frac{-3}{x^4}u(x) + \frac{1}{z^3}u'(x)\right). \tag{3.63}$$

The results of the calculation are shown in Fig. 3.6, where we plot the reflection probability for both the full QED potential, and the van der Waals limit. The reflection changes by many orders of magnitude, facilitating an experimental measure of the Casimir effect.

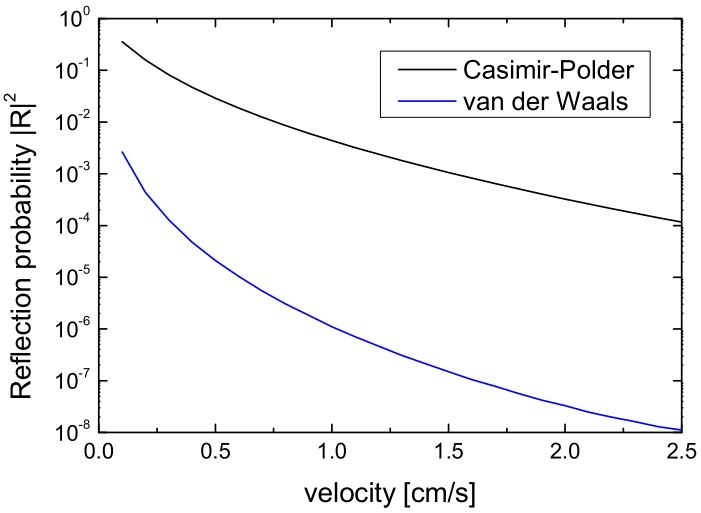

Figure 3.6: The reflection probability for sodium atoms incident on a metallic surface as a function of velocity, for the both van der Waals and Casimir-Polder potentials. The several orders of magnitude in difference make a clear distinction between the two curves, but the low incident velocities necessary for a measurement still present an enormous experimental challenge.

To conclude this section, we come back to the question of the universal behavior for the reflection probability close to threshold, that is, when the incident velocity approaches zero. According to Eq. (3.38), for small incident energies

$$|R|_{k\to 0} \sim \exp(-2bk).$$

Now, the combination bk in the exponential relates to the parameters β, l and k_2 we used in the calculation of the reflection coefficient. From Eqs. (3.51),(3.37) and (3.56) we have that

$$\begin{aligned} b_3 k &= \pi\beta k_2 = \pi\kappa(v) = 30.322\pi\, v, \quad \text{and} \\ b_4 k &= (\beta l)^{1/2} k = 2.863\, v, \end{aligned} \tag{3.64}$$

where v is in cm/s. The lowest incident velocity calculated was $v = 0.1$ cm/s, which is still very far from threshold in the case of the van der Waals potential. The only reasonable answer comes if we consider the retarded potential alone. Replacing $b_4 k = 0.2863$ in Eq. (3.38) gives for the reflection probability

$$|R|^2 \sim 0.318, \tag{3.65}$$

while the value found in the computation is $|R|^2 = 0.354$.

3.6.4 An experimental concern

Now that we have reviewed the origin and characteristics of quantum reflection, and calculated the probability for its occurrence, we understand the need for small incident velocities in order to observe the effect. In the calculations we have assumed that atoms that did not reflect are simply lost and never counted. However, during the experiment these atoms will undergo interaction with the wall in some way. For sodium atoms having an incident velocity of 1 cm/s towards the wall, the corresponding kinetic energy is 1.1×10^{-11} eV. At these extremely low energies, atoms that are not reflected due to quantum reflection cannot induce elementary excitations in the surface like excitons, plasmons or phonons; these processes involve energies within the range 1 meV to a few eV [82].

It is not clear whether non-reflected atoms will stick to the surface, and what the process involved may be [113]. Low energy atom-surface bound states between Cs and a dielectric surface have been considered in reference [114], where a spectroscopy method to study them is proposed. The authors study levels with energies on the order of 10^{-8} eV, three orders of magnitude larger than the characteristic energies expected to yield quantum reflection in our experiment. Already at these energies the 'bond length' between an atom and the surface would be on the order of tens of nanometers! The temperature of the surface may also play a significant role. While a more detailed study of these processes is needed, in our experiment we expect to distinguish the specular fraction of reflected atoms. We can image the atoms after reflection a few hundred micrometers away from the surface by using absorption imaging (the technique is described in Section 5.2), and also 10 cm below the surface using either absorption or fluorescence detection. A combination of these methods will help us to distinguish only those atoms that have undergone quantum reflection.

Chapter 4

Experimental techniques II

4.1 A new experimental system

The experimental observation of quantum reflection is not an easy task, much less the precise determination of the Casimir-Polder potential. Several techniques must be used in order to have the interacting atoms with a spread in velocity much less than the required incident velocities necessary for reflection. Also, the control over the atomic motion must be very precise during the process of launching.

At this point, it is convenient to give a general description of the experimental sequence necessary to measure the reflection probability. Atoms from a thermal source are trapped and cooled down to temperatures below 1 μK, using laser cooling and subsequent forced rf evaporation in a magnetic trap. Once the atoms are cold they can be transported and launched towards a surface using magnetic or optical potentials. For convenience, the surface is located a few centimeters above form the initial position of the atoms. Due to the low kinetic energy, the atomic cloud does not spread spatially during the launch. Finally, as the atoms reflect from the surface they can be imaged *in situ* using an absorption technique, or fall freely under gravitational force, and be recaptured at the initial launch position. The atom number can then be counted and compared with the incident number, obtained from a destructive measurement prior to the launching. This method for measuring the reflection

probability clearly relies on small statistical fluctuations of the initial number, and averaging is needed.

While substantial modifications to this scheme can be made, it contains the essence of our current experimental setup. We actually started developing necessary tools while working with ultracold atoms in a vapor cell [15]. However, we realized very soon that the previous chamber had enormous limitations, and had to be replaced. The design of the new chamber took into account the next generation of planned experiments, that include atom-surface interactions, and quantum transport in non-periodic lattices.

In this chapter we give a description of the apparatus we use to trap and cool atoms to the point of quantum degeneracy, including the effusive oven, the Zeeman slower, the main chamber, and the magnetic trap.

4.2 The oven

The effusive oven is at the beginning of the entire experiment, providing an atomic beam to be decelerated by the Zeeman slower. The Zeeman slowing technique, however, has limited efficiency: about 1 part in 10^6 of the atoms coming out of the oven will be in the MOT region with small enough velocities to be captured. The oven consequently has to be operated at relatively high temperatures (550K), and macroscopic amounts of sodium usually do not last for more than a few hundred hours. The oven chamber must be designed such that it allows for quick and practical refilling, without disturbing the vacuum of the main chamber. Considerations of design along with typical numbers and parameters will be discussed in this section.

4.2.1 The design

When the experiment was still in the design phase, we did not have in mind a simple effusive oven. Instead, the entire oven chamber was planned and built to house a recirculating oven. The recirculating oven made in our lab was based on a design by the Harvard group [115]. The idea is to recover atoms that otherwise would stick to the walls of the chamber, and bring them back to the oven. This is done by separating the design in two parts: the emission part, and a 'recovery zone'. Atoms are recovered by laying a gold wire mesh at a temperature above the melting point of the substance (98 ^{o}C in the case of sodium). Once the atoms 'wet' the mesh in one end, they go back to the other end, situated at the oven reservoir, by means of capillary action. The idea is very attractive, because the recycling of the atoms means that the oven lifetime can be extended to thousand of hours, as opposed to few hundred hours for a conventional oven.

A considerable amount of time and effort was put to make the recirculating oven work. However, after a few months of testing and debugging, it had to be abandoned. Several problems arose, mainly concerning the mesh, and atoms very easily clogging the outer emission hole. The oven was never reliable in terms of flux, and a simple effusive oven was finally made. There is, however, the possibility of using a recirculating oven with a much simpler design [116]. This would allow reservoir lifetimes of few thousand hours.

The actual oven chamber consists of four parts: 1. The oven, 2. The cryo-shroud, 3. The housing chamber, and 4. The differential pumping region.

1. **The oven.** The oven is extremely simple: it is a can made of SS 304, 3.5" deep, and 1.125" in diameter, Fig. 4.1. Close to the top there is

the emission hole, 5 mm in diameter. The can extends 1.5" from the bottom, and is attached to a conflat flange at the end of that extension. The bottom of the oven has one recessed entry 0.265" in diameter, that houses an 80W cylindrical heater. The heater is pushed all the way to the top of the recessed hole, ending where the emission hole is located, Fig. 4.1. The idea is to have the emission hole as the hottest spot in the oven, to prevent clogging (even though it is unlikely due to the size of the hole). The walls at the hole are shaped such as to have a knife edge, minimizing again risks of clogging.

2. **The cryoshroud** A cryoshroud (Thermionics, 8" OD) surrounds the oven, and was installed to provide further pumping by the combined action of a titanium sublimation pump and filling the shroud with liquid nitrogen. In the early stages of the experiment we were not completely sure the differential pumping tube would be enough to isolate the main chamber to the required pressures of a few times 10^{-11} Torr. We used liquid nitrogen only during the first few weeks of testing. Afterwards, the cryoshroud serves no purpose other than acting as a 'cold finger' at a little bit higher than room temperature. This avoids coating the rest of the chamber and the differential pumping region with unwanted sodium.

3. **The housing chamber.** The oven chamber houses the cryoshroud, the oven, and has a turbo-molecular pump attached to it. Several ports were put in order to have optical access for diagnostics, and venting. However, with time, most of these ports were blanked off. Only one port for an ion gauge was needed, and another, very important, for a rotary motion vacuum feedthrough was also required. This feedthrough is used to move

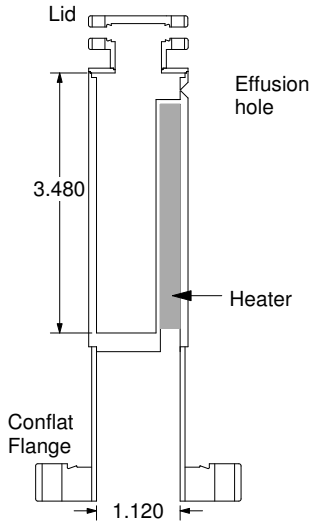

Figure 4.1: The effusive oven. We load typically 15 g of sodium, which last for about 450 h at full operation.

a flag in and out of the atomic beam path. This shutter helps isolate the main chamber from the oven.

In the final design the chamber is a cylinder of 10" diameter and 8" in height. While some of its features are never used, it is fully functional and reliable.

4. **The differential pumping tube and 2D Molasses region.** We consider the differential pumping tube and a 2D molasses region part of the oven chamber because they are baked together when a sodium change is made. A gate valve separates the oven side from the Zeeman slower.

   The differential pumping tube was designed to withstand three orders of magnitude of differential pressure. It is a tapered hollow tube made out of stainless steel. The original piece has a length of 7.0", with initial

and final openings of inner diameter 0.625" and 0.25", respectively. A small, 1" long, appendage was added at the beginning of the tube to limit further the conductance. The diameter of its opening is 0.125". The tapered form was designed to match the divergence of the atomic beam coming out from the oven. The distance between the effusion hole and the beginning of the differential pumping tube is 3.5". The conductance of the tube is 0.15 l/s, enough to maintain the required differential pressure of three orders of magnitude between the oven chamber and the Zeeman slower.

To attach the differential pumping tube to the body of the oven chamber, a bellows is used. This allows almost independent motion of the entire oven chamber respect to the rest of the chamber. This proved to be very useful in aligning a misplaced effusion hole in the oven to the line of sight of the slower. After the bellows there is a six-way crossing, where 4 of the 2-3/4" viewports are used for transverse 2D molasses cooling of the atomic beam (Section 4.3.5). The cross has an additional port that is used for pumping out that region during the bakeout.

After the 2D molasses region, an all-metal gate valve (VAT # 48132-CE01) is placed. The choice for installing this valve at this location was a very fortunate one. The valve has an unlimited number of openings and closings, can be sealed easily by hand, and holds vacuum in the main chamber at the 10^{-11} Torr regime when we break vacuum in the oven chamber. At the end of a typical day of running the experiment the valve is closed, minimizing risks of losing vacuum due to catastrophic failure of the turbo pump on the oven side. These features would be unrealistic with a normal gate valve, which very

often require a much higher torque to seal, and have only a few openings and closings before its gasket needs to be replaced.

4.2.2 Vacuum considerations

When the oven is fully operational, a vacuum of up to 10^{-8} Torr in the oven chamber is acceptable. Higher pressures would require a differential pumping tube with unreasonable conductance. We achieve the required pressure with a turbo molecular pump (BOC Edwards, 240 l/s pumping speed). The choice for using a turbo pump is understandable as ion pumps are quickly poisoned in an environment of relatively high pressure alkali gases (10^{-8} Torr). Regarding this type of pump, however, mechanical vibrations were initially thought to be a significant concern. A turbo pump operates by imparting a preferred velocity to molecules hitting a set of high speed rotating blades, keeping a differential pressure between them. The vibrations produced by the rotating blades are above 1×10^3 Hz, and can be heard and felt as they travel through the structure supporting the oven and the Zeeman slower. Even worse are the vibrations produced by the required backing pump, a standard rotary vane mechanical pump. These vibrations occur in the range between 10-500 Hz. Care was taken to minimize the vibrations produced by the backing pump, by attaching a heavy load to one of the tubes connected to the inlet port. The turbo pump is connected to the backing pump with a flexible braided hose that is also clamped using sorbothane. With regard to the noise produced by the turbo pump itself, it is damped greatly along the chamber. First, a bellows connecting the oven chamber to the slower prevents direct transmission of vibrations. Second, the slower itself weighs 70 kg, presenting a large inertial mass. Finally, another bellows connects the slower to the main chamber.

Noise due to the pumps turned out to be not a problem for getting Bose condensation. One last factor that contributes to mechanical stability is the monolithic character of the magnetic trap (Section 4.8.6).

4.2.3 Operation of the oven chamber

Loading. We typically load the oven with 15 g of sodium (ESPI 3N5 grade, 99.95% purity). The sodium is shipped in breaksealed pyrex ampoules, each containing 5 g under an argon atmosphere. Loading into the oven is done by breaking the ampoules, and crushing the glass in small pieces about 5 mm in size. This must be carried out under a fumehood, with nitrogen flowing through the working region. Using a metal rod, the sodium and shattered pieces of glass stuck to it are stuffed in the oven. Once all 15 g have been put inside, a mini conflat secures the top (Fig. 4.1). This procedure takes about 3-4 min. We currently have two almost identical ovens[1]. The reason for this is to minimize the time it takes to change the sodium after depletion. This is important as grams of sodium deposited in the chamber react immediately with water once vacuum is broken. The resulting sodium hydroxide (NaOH) can clog the differential pumping tube. Once sodium hydroxide forms inside the chamber it is difficult to remove without thorough cleansing, as its melting point is 318 °C, compared to 98 °C for Na.

When the oven is depleted, a new load of sodium is prepared in the second oven. Once this is done, a valve is closed to isolate the backing pump,

[1]The ovens have only one slight difference, in the height at which the effusion hole is located. In one oven the hole was misplaced by 0.25". This, however, was not a serious problem due to the size of the hole itself. The whole oven chamber had to be tilted to regain the necessary atomic fluxes.

and the turbo pump is turned off. Vacuum is broken in the oven chamber, the empty oven removed and the new one installed. After this, both backing and turbo pumps are connected and turned back on. The whole process takes about 5 min, and it is done under the flow of nitrogen to minimize exposure of sodium to air. After the installment a bakeout proceeds.

The procedure described to change the sodium is followed about three or four times before a thorough clean up of the oven chamber is needed. For this, the chamber is disassembled and all NaOH traces removed, mainly from the bottom of the chamber and from the elbow that connects to the turbo pump.

Bake out. After a sodium change is completed, the oven chamber (oven housing, differential pumping tube, and 2D molasses crossing) is baked for a few days. The philosophy found to work is to go up from room temperature up to 200 ^{o}C is two days, stay at the maximum temperature for two more days, and finally bring the temperature down in two more days. After this, there is one day to clean the pressure gauges, and to fire the titanium sublimation pump. Finally, one more day to realign the 2D molasses optics, test the system for possible leaks, and let the pressure go down to typical 2×10^{-9} Torr, as measured by an ion gauge placed close to the oven. It takes eight to ten days from the point of running out of sodium to resume the experiment fully. This happens every four months or so, depending on the number of hours devoted to run the experiment. Recirculating oven designs could make this period many times as long, but it may add extra complications to the simplicity we currently have.

The bakeout and sodium change procedure do not always run smoothly.

In fact, great care has to be taken to avoid contamination by sodium of any viewports close to the oven. This is a serious problem, as many times we found that, after the end of a bakeout, numerous viewports either cracked with leaks or shown signs of alkali poisoning along the kovar seal. This is the reason why all viewports (save one) in the original design for the oven chamber were removed and the flanges blanked off.

4.2.4 Final numbers

A new load of 15 g of sodium lasts for about 450 h, with the oven operating at a temperature of nearly 250 °C. To estimate the lifetime of the oven, we consider a 3D Maxwell-Boltzmann velocity distribution:

$$f(v) = \frac{1}{(2\pi)^{3/2}\sigma_{\mathrm{v}}^3} \exp\left(-\frac{v^2}{2\sigma_{\mathrm{v}}^2}\right), \tag{4.1}$$

where $\mathbf{v}$ is the velocity, and $\sigma_{\mathrm{v}} = \sqrt{k_{\mathrm{B}}T/M}$. The fraction of atoms with velocity between $\mathbf{v}$ and $\mathbf{v} + d\mathbf{v}$ is $f(v)dv_x dv_y dv_z$. The atomic flux Φ coming out of a hole of area A is:

$$\begin{aligned} \Phi &= nA \int_0^\infty v_z f(v)\, d^3v. \\ &= \frac{1}{\sqrt{2\pi}} nA\sigma_{\mathrm{v}}, \end{aligned} \tag{4.2}$$

where n is the density. Using the relation $P = nk_{\mathrm{B}}T$, we put the flux in terms of pressure and temperature:

$$\Phi = \frac{PA}{\sqrt{2\pi M k_{\mathrm{B}} T}}. \tag{4.3}$$

The vapor pressure for atomic sodium at a temperature T is [117]

$$\log_{10} P = 5.006 + 4.704 - 5377/T, \tag{4.4}$$

where P is in pascals, and T in kelvin. At a temperature 250 °C the pressure is 0.27 Pa (2.0×10^{-3} Torr). In our oven, the emission hole has 5 mm in diameter. With this information we get:

$$\Phi = 1 \times 10^{17} \text{ atoms per second.} \tag{4.5}$$

Considering that we load 15 g of sodium (3.9×10^{23} atoms), the estimated lifetime is 1080 h. As stated before, typically we see complete depletion after 450 h. This may be because of an underestimate in the temperature of the oven. For comparison, at a temperature of 275 °C the sodium has a vapor pressure of 0.79 Pa (5.9×10^{-3} Torr). A load of 15 g of sodium would last for 470 h, close to what we observe.

4.3 The Zeeman slower

A standard Magneto Optical Trap is capable of cooling and trapping atoms with velocities up to a few tens of meters per second. Such atomic samples can be provided by a reservoir heated up beyond the melting point of the substance, as it is done in the case of a vapor cell. However, the atoms captured captured by the MOT consist of the low-velocity class of the Maxwell-Boltzmann velocity distribution, limiting their number considerably. A response to this challenge is the Zeeman slower (ZS) technique, invented in 1982 [118], which is used to obtain atomic beams with low velocities and high flux. Other slowing techniques developed later used laser beams swept in frequency [119], and electric fields [120].

To decelerate an atomic beam using a single counter-propagating laser beam it is necessary to keep the atoms in resonance with the light as they are

decelerated. This can be achieved by a spatially varying magnetic field. The main objective in the design of a Zeeman slower is to decelerate atoms in the shortest time possible, making its length reasonably short so the divergence of the atomic beam is minimized. Therefore, the maximum deceleration possible must be used. In the case of an atom absorbing and re-emitting photons, the maximum deceleration possible is equal to one recoil velocity in one spontaneous absorption-emission cycle. This means $a_{\max} = v_{\mathrm{r}}/2\tau$, where τ is the lifetime of the excited state. The factor of 2 in the denominator is due to the maximum scattering rate at very large saturation intensities, see Eq.(6.5).

Next, we must determine the shape of the changing magnetic field that keeps the atoms in resonance. We call Δ the detuning of the laser beam with respect to the zero velocity atoms in the lab frame. The resonance condition means that the Doppler shift compensates the Zeeman Shift plus the original detuning: $\mu B - \Delta = kv$. Both the magnitude of the field B and the velocity v change with time as the atom is decelerated. For constant deceleration the field must change as a function of distance z:

$$B = (\Delta + \sqrt{v_i^2 - 2za}/\lambda)/\mu. \tag{4.6}$$

To achieve such a variation in the magnetic field, the first successful slower used a tapered coil that started with a high magnetic field close to the diffusion oven, and ended with a field of magnitude close to zero [118]. This is known as a decreasing field Zeeman slower. The opposite configuration can also be used, where the field starts close to zero and ends with high negative values. Such configurations have three characteristics: (1) First, the power dissipated in the coils is very large, up to several kilowatts. (2) The field at the end of the slower, close to the MOT region, has to be taken into account in the design

of the MOT fields. In fact, in some slowers the tail of its field is used as part of the trapping field of the MOT, therefore maximizing the delivery of atoms from slower to MOT. (3) Finally, the slowing light may be close to resonance for the MOT atoms, resulting in displacement of the trapped atomic cloud.

While all the previous points can be addressed and solved after some work and care, there is an optimum configuration that satisfies many of the characteristics that are important in the design of a slower. This configuration is known as the *spin-flip* Zeeman slower. In this case the magnetic field varies according to Eq. (4.6), with an offset in the field. The maximum magnitude of the magnetic field becomes roughly half compared to that of either increasing or decreasing field configurations. This reduces the magnitude of electrical currents needed, and consequently dissipates much less power compared to normal slowers.

4.3.1 Spin-Flip slower

We can understand easily what happens with the atomic spin as the atoms travel along a spin-flip slower, by making a comparison in both the stationary lab frame and the moving frame of the atoms. The atomic frame is defined by the direction of the magnetic field. We consider transitions between levels $J = 0 \longrightarrow J' = 1$. In Fig. 4.2 we have a schematic of the basic idea of any ZS: the Doppler shift brings atoms into resonance with the laser light, by compensating for the shift in the atomic energy levels due to magnetic fields, and the light detuning. At the beginning of the slower in both the atomic and the lab frames the spin is aligned in the same direction as the magnetic field. The light, having a polarization σ^+ in the lab frame starts driving transitions

between the sublevels $m_J = 0 \rightarrow m'_J = +1$.

At the zero crossing point all Zeeman sublevels are degenerate, and the helicity of the slowing light is defined only by residual fields. After crossing the zero, the atoms experience again the usual Zeeman shift. In the lab frame, however, the spin still points in the same direction while that of the magnetic field has changed. The light has now become σ^- as far as the atoms are concerned, and the cycle continues with transitions between the $m_J = 0 \rightarrow m'_J = -1$ sublevels. In conclusion, the spin flips only in the frame of reference defined by the magnetic field.

The zero crossing point is dangerous as some of the atoms become unpolarized, and therefore lost for further slowing. This problem can be minimized by the addition of a small field in the transversal direction. In our final design, the atoms have velocities on the order of 350 m/s at the zero crossing point. Assuming this region to be 1 cm long, the atoms spend 30 μs there. A constant field of 1 G produces a Larmor frequency of 1.4 MHz, giving each atom enough time to keep their polarization.

4.3.2 The design

Based on the experience and information from other labs using sodium [121, 122], we decided to construct a spin flip Zeeman slower with one major feature: coils partitioned in individual sections and connected electrically in series. The tapered solenoid used in previous designs produces a very smooth changing field that keeps the atoms always on resonance. However, it has several disadvantages: because it is a single, long solenoid, any electrical short ruins the whole structure. The power dissipated in the coil typically requires significant

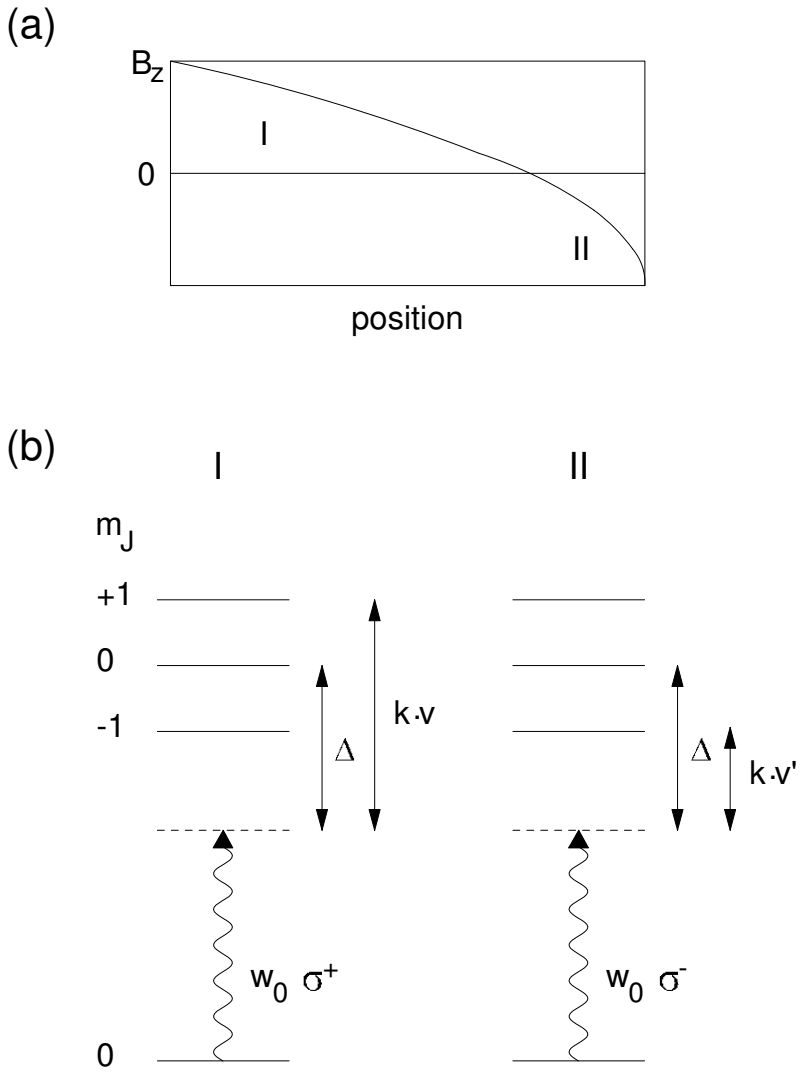

Figure 4.2: The evolution of a $J = 1$ atomic spin in a spin-flip Zeeman slower. (a) A schematic of the field variation as a function of position. At the beginning of the slower (region I) the atomic magnetic moment aligns with the field. After crossing the zero crossing (region II), the spin becomes anti-aligned with respect to the new field direction. (b) The optical transitions also change labels as atoms travel along the slower.

cooling, and water is used often, carrying its own problems in the design. In fact, current-carrying copper tubing has been used to create these slowers with very efficient cooling, as the water flows through the tubing. But these structures are difficult to repair when they break, and not easy to construct in the first place.

We use several identical coils, put side by side, and connected in series. The advantages are:

1. Each individual coil has its own current driver that can be optimized independently of the other coils.

2. Mounting the individual coils on fins makes cooling very efficient such that air cooling is enough.

3. Repair of possible electrical shorts reduces to the replacement of only one small section of the slower.

On the other hand, there is one major disadvantage of design over a tapered solenoid: the produced field is not as smooth, resulting in the loss of atoms and overall efficiency. We now proceed to discuss the design in detail.

While we were still embarked in some work to keep the old chamber alive, visiting student Artur Widera started to design and build our Zeeman slower in the summer of 2000 [123]. The goal of the slower is to produce a field of the form given in Equation 4.6, taking into account all offsets in the field and the detuning of the slowing light. The chosen value for the initial atomic velocity was 850 m/s. The acceleration parameter was set to $a = 0.50\, a_{\max}$. Assuming constant deceleration, the length of the slower is 77

cm. In a decreasing field Zeeman slower with $\Delta = 0$, the required initial field to stop atoms at the initial velocity v_i is:

$$B_0 = \frac{v_i}{\lambda\mu}. \tag{4.7}$$

In the case of the $3S_{1/2}(F = 2) \longrightarrow 3P_{3/2}(F' = 3)$ cycling transition of sodium:

$$\mu = \mu_B(m_{F'}g_{F'} - m_F g_F) = (3\frac{2}{3} - 2\frac{1}{2})1.4\,\text{MHz/G} = 1.4\,\text{MHz/G}. \tag{4.8}$$

This value makes $B_0 = 1030$ G. In the spin flip slower such high fields are not needed, and we chose to have the first and last coil to produce the same magnitude in the field, that is, roughly 500 G. The last thing to consider is the detuning of the light. If we want to decelerate atoms having initial velocities of 850 m/s, and have an initial magnetic field of 515 G, then we need a detuning equal to

$$\Delta = B\mu - \frac{v_i}{\lambda} = -720\ \text{MHz}. \tag{4.9}$$

In order to produce such detuning, we use a 300 MHz acousto-optic modulator (AOM) in the double pass configuration. It turns out we cannot get detunings larger than 600 MHz in the light because of limitations in our AOM. Such detuning limits us to capture initial velocities up to 800 m/s.

The last relevant part of the design was the number of coils forming the slower. Using only a few coils would make the field look like a staircase instead of a nice slope, leading to unacceptable slowing efficiencies. On the other hand, too many coils would make the number of variables to control impractical, and technically difficult to control. A good compromise was found after calculating the fields taking into account geometry, weight, and power dissipation. The final number was 12 coils in series. An additional coil, the

'extraction coil', is added at the end to oppose the huge field of the last coil. This stops the deceleration process, and allows the obtention of an atomic beam with a controllable final velocity.

4.3.3 Construction

In order to produce the required fields it is desirable to wind coils with a small diameter, to reduce the amp-turns product, which also decreases the dissipated power. For the coils we use 18 AWG wire, which was decided after considerations of resistance, size and weight. About 700 turns form each coil: 300 in one inner cylinder and 400 in one outer. The resistance of each coil (700 turns) is about 5 Ω. We wind the coils in brass cylinders that can slide outside a standard vacuum tube of 1.75" OD 4.3. An individual coil is wound in two concentric cylinders of length 2.6". The inner cylinder has an inner diameter of 2.5", and the outer has an inner diameter of 3.5". Both have a thickness of 0.125". For cooling and structural stability purposes, the cylinders were attached to copper plates of dimensions 7.5×7.5×0.125". The brass cylinders fit into a groove 1 mm deep milled into the copper plates. The plates have a circular hole 2.375" in diameter, so that an aluminum pipe of slightly smaller outer diameter supports the entire structure. This pipe also helps centering all the coils. Holding the two plates together are springs, which keep the coils well secured.

One important idea of the design was to have coils that could be assembled and never removed, even during bakeouts. This imposed constrains in the materials used, as well as in the insulation between the slower assembly and the chamber vacuum tube. For this reason, the chosen wire for the coils was

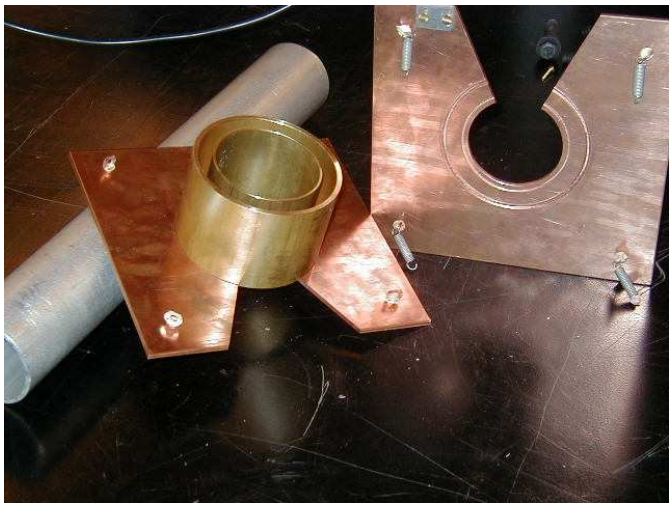

Figure 4.3: A picture of a Zeeman slower coil assembly, showing the brass cylinders and the copper fins used for mounting.

a Phelps Dodge Poly-Thermaleze Tough Wire. The wire has Thermal Class 220 (20,000 h lifetime at 226 °C), and is insulated with multiple coatings of polyester and polamyde Imide. The wire is bakeable up to 200 °C, and is less prone to scratches. To minimize the risk of electrical shorts, layers of Dupont Kapton film (500 HN, .005" thick) are placed between the wire and the metal cylinders. Kapton film was also used in adhesive tape form (0.00" thick, 0.5" width, with 0.002" thick adhesive on one side).

Once all the individual coils were wound and assembled, they were mounted in the long aluminum pipe. Inside this pipe it was inserted the vacuum tubing that connects the oven region with the main chamber. In between the two a thermal insulating layer of fiber glass was placed. Right in between the insulating layer and the vacuum pipe heaters were installed for bakeout use.

The total weight of the Zeeman slower is about 70 kg, including copper, brass, wire and aluminum structure. To get an idea of the dissipated power,

and compare to that used in a decreasing field slower, we use Eq. (4.6). In our case we use $n = 12$ nearly identical coils. The current in each coil as a function of distance has the form:

$$I_n = I_0(2\sqrt{1 - n/11} - 1), \tag{4.10}$$

where I_0 is the magnitude of the current in the first coil (roughly equal to that of the last one). The factor of 11 used in the denominator is used because $n \in [0, 11]$. Each coil has a resistance R. The total dissipated power is then

$$P = \sum_{n=0}^{11} I_n^2 R = I_0^2 R \sum_{n=0}^{11} (2\sqrt{1 - n/11} - 1)^2 = 4.9\, I_0^2 R. \tag{4.11}$$

For our coils $R = 5.0\,\Omega$, and $I_0 = 4.7$ A. This makes $P = 540$ W. In reality, because fringing fields contribute to the field created by adjacent coils, the power dissipated is less. A more careful estimation gives us 430 W. In a decreasing field Zeeman slower using the same geometry, we would have required to shift the magnitude of the field by roughly 500 G in all the coils. That is, an extra $12 \times I_0^2 R = 1400$ W.

The cooling is done with a set of fans placed on top of the structure, and the temperature never goes above 40 °C.

4.3.4 Results

In March 2002, soon after the effusive oven was completed, we started the testing of the slower.

The slowing light is created by splitting off 85 mW of the MOT light. The repump light is absolutely essential, so about 15 mW is used (because the correct frequency is produced with an electro-optical modulator, only one third

of the total beam power is in the relevant sideband, Section 2.2.1). Each beam is shaped independently in order to have the two co-propagating with same size and divergence. The beams are combined and overlapped in a polarization cube beam splitter (PBS). Naturally, this produces beams with orthogonal polarizations, so another PBS is used to equal the polarizations, with about 50% transmission. The rejected beams travel together to form a 2D molasses stage at the beginning of the slower. After the two PBS, the ZS AOM receives 85 mW of resonant light and 15 mW of repump. The AOM is used at 300 MHz in the double pass configuration, shifting therefore the frequency by 600 MHz.

The total efficiency of the double-pass is about 50%. After the AOM, the beams are expanded to a waist of $\omega_0 = 1.7$ cm, making the peak intensity equal to 7.7 mW/cm^2. Right before the beam enters the chamber, a lens is placed so that the focus is located at the hole of the oven. This matches (to first approximation) the divergence of the atomic beam with that of the slowing light beam. The scattering rate at the end of the slower (MOT region) is equal to 1.7×10^7 Hz, which multiplied by the recoil velocity $v_\mathrm{r} = 3\,\mathrm{cm/s}$, makes the acceleration $a = 0.5\,a_\mathrm{max}$, as assumed earlier during the slower design.

After completion of the slower, the first check we made was a measurement of the atomic velocity distribution. A probe beam was sent to the MOT region (1.8 m away from the oven), and its frequency scanned while the fluorescence was collected using a photomultiplier tube (PMT). To be Doppler sensitive to the atomic velocity, the probe beam made a 60^o angle respect the atomic beam path. The measured fluorescence as a function of frequency was indicative of the distribution. To scan the frequency we used a double pass

AOM that could be scanned from 180 to 300 MHz (360 to 600 MHz change in the light frequency). Therefore, we could see atoms having velocities between 0 and 240 m/s.

After optimizing the current of the coils in the slower we could get a peak in the fluorescence signal around 100 m/s, with a full width at half maximum (FWHM) of 50 m/s. For some unknown reason, the signal disappeared when probing smaller velocities. While this was somewhat disturbing, we decided to continue, and perform the final optimization of the slower by using a MOT. This method is clearly not the best, as the MOT itself has a capture limit in the velocity of about 30 m/s, making difficult to see what is happening at higher velocity classes. Also, the MOT saturates when a particular number of atoms is captured. In conclusion, the MOT is good enough to align the slower and making it work, and that is what we did. However, it cannot provide reliable numbers for the atomic flux for any velocity higher than 30 m/s.

In Fig. 4.4 we show a plot of the measured magnetic field of the slower, using the design values for the currents. An analytical formula was fit to the data, taking into account all the geometry of the coils, having one free parameter per coil to match the measured field. This curve is shown on top of the measurements. The designed slower was expected to slow atoms with initial velocities on the order of 850 m/s. On the same graph, we show the actual field in current use (as estimated by using the fitting function and the actual optimized currents). There are several points worth mentioning.

1. At the beginning of the slower, the field is 300 G only, instead of the calculated 500 G. This of course limits the initial velocities of atoms to

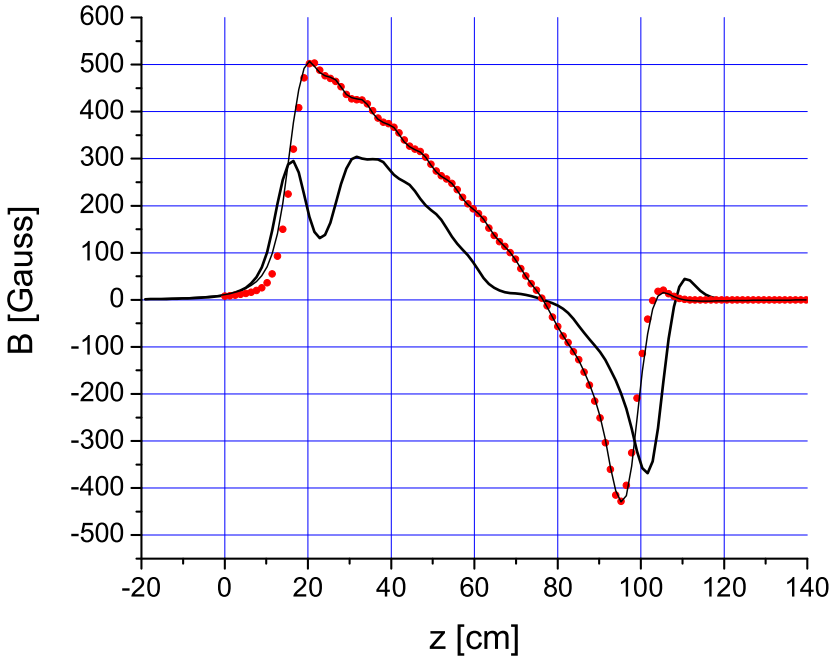

Figure 4.4: The field of the spin-flip Zeeman slower as a function of position. The red dots represent the measured values of the field after the slower completion, and the thin line is a fit using an analytical function. The thick line represents the actual field used in the experiment, deduced from the fitting function, and the values of the actual currents.

slow, which in turn decreases the number of slowed atoms considerably. In our case, the maximum slowing velocity is 625 m/s. In order to get more atoms it is necessary to increase the oven temperature at the expense of vacuum pressure and oven lifetime. Additionally, we did not observe any improvements by using higher currents in the first coils. Since any additional current contributes to heating, we maintain the low current values.

2. The second coil is off. Surprisingly, any other value than 0 A in the coil

degrades the overall performance. There must be one or more reasons for this. Because we had a good MOT that enabled evaporative cooling and, ultimately BEC formation, we did not pursue a formal investigation of these bugs.

3. Towards the zero field crossing the actual slower was elongated with respect to the calculated curves. The reason for this was mentioned earlier, as is necessary to allow the atoms to follow the field adiabatically. A space of about 10 cm was inserted between coils 9 and 10. In this spacing a permanent magnet was placed, to provide a small field in the perpendicular direction to the slower axis. The magnitude of the field at the atoms' position is about 10 G. This improved the final flux, as it helped the atoms to perform a 'spin flip' into the second part of the slower.

4. The final coil of the slower, or 'extraction coil', cancels the field at the end of the slower. This minimizes the effect of fringing fields on the MOT and subsequent magnetic trap, located 25 cm away form the last ZS coil. At this position the field is on the order of few tens of milligauss. This is not very important for the magnetic trap, as its direction is along the strong axis of the Ioffe-Pritchard trap (Section 4.8.3).

Using the estimated magnitude of the actual field across the slower, and the parameters for the slowing beam, we can calculate the evolution of the atomic velocity as it travels through. The results are depicted in Fig. 4.5. The highest atomic velocity class that can be slowed is about 625 m/s. It is important to notice how the atoms stop decelerating when the field becomes flat. This

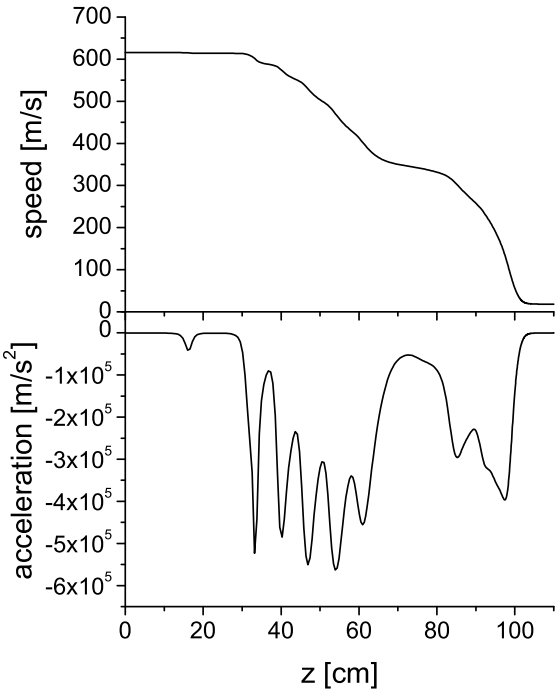

Figure 4.5: The evolution of the atomic velocity in the Zeeman slower. The initial and final velocities are 615 m/s, and 18 m/s respectively. The gap seen around z=72 cm corresponds to the field zero-crossing region.

happens at the regions between coils and can be seen as small steps. In order to compensate for this, we wound additional coils right in between two main coils in the first part of the slower. The produced field was on the order of 10 G, enough to modify the 'steplike' structure. However, we did not see any improvement in the number of atoms captured in the MOT.

The conclusion is that the Zeeman slower is not working at 100% of its capability, but it works well enough to routinely produce Bose-Einstein condensates.

4.3.5 Addendum. 2D Molasses

A normal Zeeman slower is enough to provide fluxes on the order of 10^{10} atoms per second at 20 m/s in the MOT region, until the oven depletes. In

order to extend the oven lifetime, various approaches have been pursued. One possibility is the use of recirculating ovens, as discussed in Section 4.2. The second is to minimize the transversal spread of the atoms as they travel through the slower. This will increase the final number of atoms in the MOT region, so it is possible to reduce the temperature of the oven while maintaining the flux. The reduction in the transversal velocity distribution can be realized by a two dimensional (2D) molasses stage after the oven, which consists of two orthogonal pairs of counter propagating cooling beams. Its use may result in the extension of the oven lifetime by a considerable factor.

For this purpose, we use the six-way cross between the oven chamber and the beginning of the Zeeman slower, and implement the 2D molasses there. It has the disadvantage of adding distance after the oven so that atoms spread more spatially, however this is overcompensated by the cooling provided in the 2D molasses stage.

The 2D molasses is formed by a single beam (containing resonant light co-propagating with repump light) that first goes through an anamorphic prism. Then it is expanded to a size of about $\omega_0 = 5$ mm in the short direction, and aspect ratio of 3. Typical power used is 20 mW for resonant light and 10 mW for repump. The beam passes through the windows and retro-reflects, forming a stationary lattice (lin $\parallel$ lin configuration). We tried also the $\sigma^+ - \sigma^-$ configuration but it didn't improve the final flux. After the alignment is optimized, the 2D molasses gives us about a factor of 2.5 of gain in the final number of atoms captured in the MOT.

Finally, we have some power left from the combining in a PBS the slower light (28 mW of resonant light and about 12 mW of repump). They

are put to use by passing them through a 618 MHz AO, and sent almost co-propagating with the main Zeeman slower beams. Rather than adding light power, the idea is to address a different velocity class coming out of the oven. This is in spirit of the decelerating experiments done with broadband, or white light [124]. The use of this additional set of slowing light increases the total number of atoms by a factor of 1.5.

4.4 The main chamber

The design of the main chamber needs to be flexible enough to have all necessary optical access, and proximity to the atoms for magnetic trapping. The type of magnetic trap used is critical for the design. In our case, we decided to house one type of Ioffe-Pritchard trap known as the cloverleaf trap (Section 4.8.5). However, even by using this coil arrangement, the optical access is still restricted, and the use of high numerical aperture optics is prohibitive. Full optical access is necessary for our planned experiments on quantum transport in non-periodic lattices. Therefore, a glass cell is still needed, to which sub-recoil atoms can be transported. In the following lines we describe the main features of the design that accounts for specific points needed for both optical transport and quantum reflection from surfaces.

In order to decide the location of the glass cell, we chose not to transport the sub-recoil atoms horizontally, as it seemed to us that a more natural way to do it would be using a vertical optical lattice. Since the chamber is not required to extend horizontally but a few inches, a pancake shape was chosen, with the glass cell attached on top. The chamber is a parallelogram 10" long, 10" high, and only 3.5" deep. It was custom made by HPS, using 304 stainless

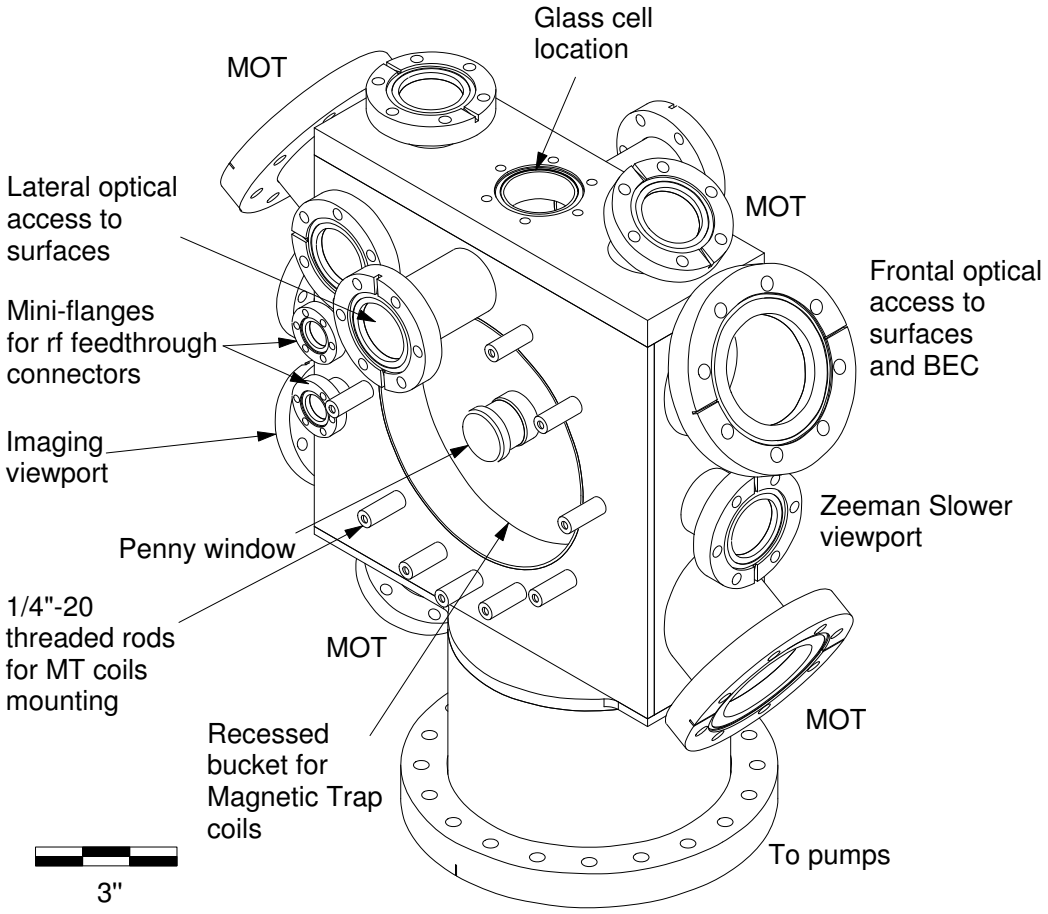

Figure 4.6: A schematic view of the main vacuum chamber used in our experiment. The main features are listed.

steel with electro-polish finish. A drawing of the chamber is found in Fig. 4.6, showing all the ports and features necessary in our experiment, which we now proceed to list.

1. **Zeeman slower.** The main chamber connects to the Zeeman slower using standard 2-3/4" vacuum flanges. In between, a 3" long bellows is placed, to avoid the problems of joining two very rigid structures. On the opposite side there is another 2-3/4" flange where a 5" extension

tube. Attached to the tube there is the viewport where the slowing light is sent through. This viewport has to be kept at a constant temperature close to 98 °C, the melting temperature of sodium. This avoids the build up of sodium on the window, which would be deleterious in two ways. First, it would make the window less transparent to the slowing light, and second, it would put the window at risk to a possible leak due to the reaction of sodium with the glass to metal seal of the window (kovar). The reason for the extension tube is to avoid some of this sodium from back-streaming into the magnetic trap region, limiting the lifetime of the atomic sample.

2. **MOT viewports.** On the narrow part of the chamber, four viewports are used for MOT beams. The other two MOT beams go through penny windows that will be described later. Of the four lateral viewports, two of them are 2-3/4", while the other two are 4-1/2" in diameter. The large opening flanges are very convenient for optical access, useful in applications like a dark-spot MOT, where an independent repump beam is needed at the center of the MOT. The viewports are oriented at a 30° angle respect to the horizontal, allowing for all other ports and flanges.

3. **Samples and optical access.** The load-lock mechanism intended to change surfaces in the atom-surface experiment was removed. In its place, a permanent holder with two samples was attached to one of the chamber side flanges. The sample holder was placed as close as possible to the center of the magnetic trap, without interfering with imaging and MOT beams.

The necessary (lateral) optical access to the samples is available with two 2-3/4" viewports. Also, a 4-1/2" viewport was placed in front of the samples, right between one MOT flange and the Zeeman slower port. This allows us frontal optical access to the samples, and to atoms in the center of the chamber as well.

4. **Glass Cell.** As stated before, a glass cell is very convenient for future experiments. It is placed at the top of the chamber, aligned with the center of the magnetic trap. The cell has quartz windows, and is only 4.0" tall, despite the fact it has a graded glass to metal seal that ends in a conflat flange.

5. **Other windows.** The beams used for transporting the atoms from the magnetic trap to their final position close to the samples enter the chamber from a lower viewport, located 23" below the trap. The viewport uses a 4-1/2" flange that is attached to an elbow 5.75" in diameter that joins the main chamber with the pumping region.

6. **Magnetic trap.** The chamber has 6" diameter recessed buckets, that house the coils for the magnetic trap. The walls of the buckets are 0.065" thick, and the separation between them is 1.0"; this proximity is required to achieve the necessary field gradients. To mount the trap coils several 1" deep rods with 1/4-20 taps were welded around the bucket.

7. **Penny window.** The design of the magnetic trap requires the coils of the trap to be as close as possible to the atoms. Optical access in the horizontal direction can only be achieved with a penny window that is welded directly onto the recessed walls of the buckets. The viewports

(custom made by Larson Electronic Glass, part # VPN-112-T-SPCL) have a 1-1/4" O.D. at the glass-metal seal, and 1-1/8" diameter at the non-magnetic, 304 stainless steel body. The view diameter is 1", and the length 1-1/5". The windows are made out of glass; quartz would have been preferable but it was not available for the required dimensions within reasonable time. They have a maximum baking temperature of 450 °C.

8. **RF coils, and holder.** The forced rf evaporation in the magnetic trap is done with two coils mounted inside vacuum. To mount the coils, eight 8-32, 316SS hex nuts were welded on the inner walls of the chamber, around the buckets. The choice for using 316SS was based on the requirement of having a non-magnetic material with low outgassing. Even though it is harder to machine, austenitic grade 316 is better than 304 in both aspects.

   The wire used for the coils is coated with kapton, able to be baked up to 400 °C. Before it was integrated into the chamber, the wire was pre-baked up to 250 °C for several hours.

   Great care was taken with the mounting of the rf coil to be under vacuum. A 1" long standoff was attached to each welded 8-32 hex nut, with machined holes and a slot to avoid virtual leaks. The wire was secured using 8-32 alumina screws in the standoffs, which compressed the wire between one alumina and one stainless steel washers. Alumina was used to avoid risks of electrical shorts between the coils and the chamber.

9. **Sample holder** The samples we use for the quantum reflection experiment are mounted in stainless steel structure. They just sit on a flat

piece, and they are pushed on the back towards stoppers placed at the front. To control the amount of force pressing the samples we have a spring that is compressed by a setscrew on the back. The spring then pushes a rod, that connects to a shim piece behind the sample.

10. **Pumping ports.** The chamber is pumped by a 270 l/s ion pump (Duniway VA-270-GX/M), with the help of a titanium sublimation pump (TSP) and a cryoshroud similar to that used in the oven chamber. Liquid nitrogen in the shroud was used only in the very early stages of the experiment. An ion gauge is placed close to the TSP. Because the main chamber is narrow, it limits the conductance. This is why 5" below the center of the magnetic trap the chamber cross section changes form a rectangle measuring 3.5" by 10" to a circle of radius 5-3/4".

    Finally, an additional port is used during baking out of the chamber. It is located in front of the base of the sample holder, and has a gate valve attached. Once the bake out is completed the valve is closed.

The conductances of the main chamber are above 500 l/s for all the elements, with the exception of the glass cell, which has a conductance of only 20 l/s approximately. The estimated pumping speed at the center of the magnetic trap is 160 l/s, produced only by the action of the ion pump. The conductance of the Zeeman slower is only 5 l/s. This small conductance together with the 0.15 l/s of the differential pumping tube completely isolate the oven form the main chamber. A drawing for the full assembled chamber is shown if Fig. 4.7.

To estimate the actual pressure at the center of the magnetic trap P_{A}, we consider the known pressure at the ion gauge in the main chamber P_{I}.

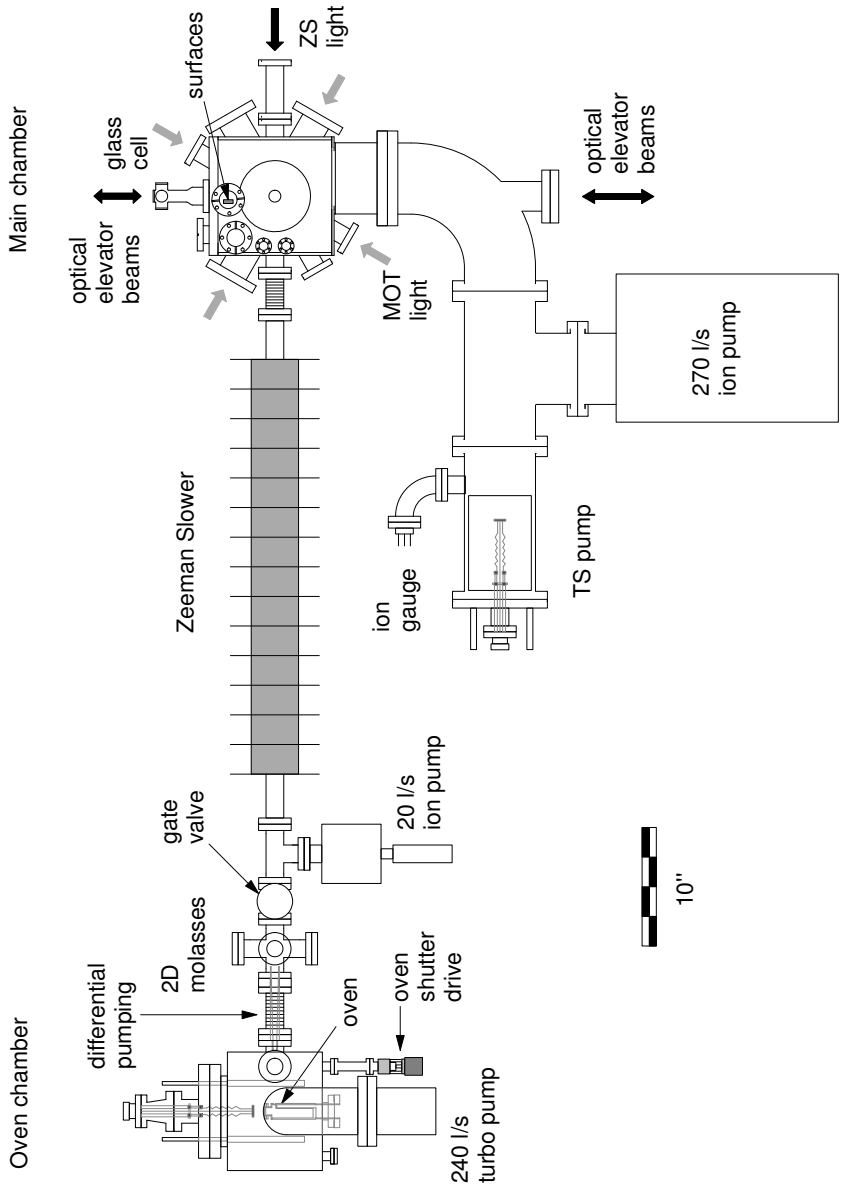

Figure 4.7: A schematic view of the full chamber assembled. The main components and features are indicated. Total length for the chamber is 2.4 m. The distance from the glass cell to the lower viewport used for the optical elevator is 87 cm. The supporting structure is not shown.

They relate to each other using the conductance from point A to point I, C_{AI}:

$$Q = (P_{\mathrm{A}} - P_{\mathrm{I}})C_{\mathrm{AI}} = S_{\mathrm{I}}P_{\mathrm{A}}, \tag{4.12}$$

where S_{I} is the pumping speed at position I. The conductance between the 270 l/s ion pump and the atomic position is much greater than between pump and ion gauge. Therefore, we can use the value for the conductance between the pump and the center of the magnetic trap: $C_{\mathrm{AI}} = C_{\mathrm{AP}} = 27$ l/s, and for the pumping speed $S_{\mathrm{I}} = S_{\mathrm{P}} = 270$ l/s. The pressure at the ion gauge during normal working conditions is 1.2×10^{-11} Torr or lower (x-ray limit). Therefore, at the position of the atomic cloud the pressure is

$$P_{\mathrm{A}} = P_{\mathrm{I}}(1 + \frac{S_{\mathrm{P}}}{C_{\mathrm{AP}}}) = 3.2 \times 10^{-11} \text{ Torr}. \tag{4.13}$$

4.5 Bakeout

The latest version of the main chamber (the one we present here) arrived in early May, 2003. With all the viewports, the rf coil in place, and the glass cell attached, a pre-bake was done to test for possible leaks and to look for problems with any of the components. The maximum temperature reached was 200 °C, during two days. In the past, a previous step would have included a bakout of the stainless steel chamber alone at a higher temperature, *in air*. This procedure has been shown to help in reducing the outgassing of SS304 by surface oxidation [125]. We decided not to do it this time because of the penny windows. All the massive metal parts like the ion pump and its surroundings can be baked by attaching heaters and wrapping in aluminum foil. However, the main chamber with the viewports needs to be in an oven, where the temperature is uniform.

A total of 30 heaters at an average of 150 W of power each were used for the bakeout of the whole chamber, excluding the part beyond the VAT valve. The chamber was baked for 13 days, with maximum temperature of 220 °C during 6 days. A graph indicating the evolution of the pressure as a function of time is shown in Fig. 4.8. When the pressure did not change any more at 220 °C, the chamber was brought to room temperature over the course of three days. At this point the ion pump, the ion gauges and the titanium sublimation pump were degassed, in that order. It is important to note that this procedure is not done at high temperature. Finally, the gate valves for the pump station during bakeout were closed, the ion pump and ion gauges turned on, and the TSP fired. The bakeout was finished by June 7, 2003.

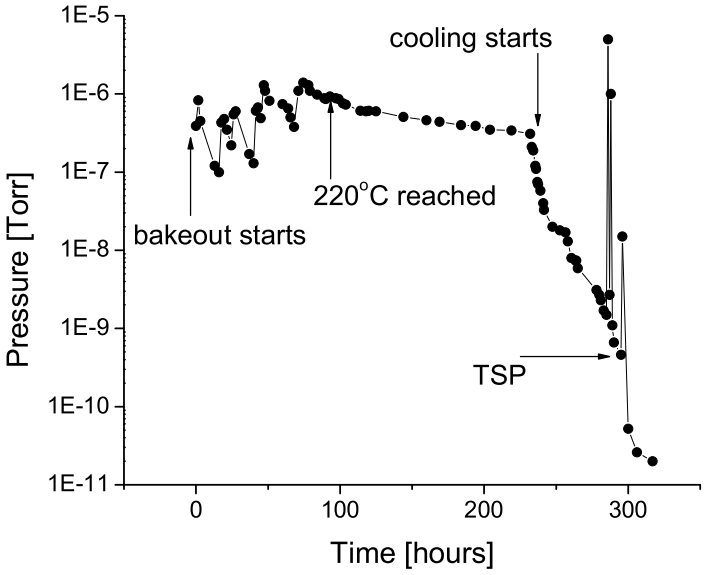

Figure 4.8: Bakeout of the main chamber. The procedure lasted for two weeks, using well over 2 kW of power in the heaters. The peaks in the pressure towards the end are due to the flashing of the ion gauges, and both ion and titanium sublimation pumps.

4.6 The laser system

All the light necessary to create and image a Bose-Einstein condensate in sodium is obtained from a single dye laser (Coherent 899-21). The laser system is basically the same used for our quantum transport experiments, and is described in Section 2.2.1. A few changes have been made, to utilize as much as possible laser light previously unused.

It is important to mention that, due to historical reasons, in our experiment we use three different optical tables. On a central optical table we have all the lasers we use for trapping and cooling (Fig. 2.2). A second table was custom made to have a notch at the center, simply a space that houses the main vacuum chamber where atoms will be captured in a MOT or magnetic trap. This second table contains all the optics necessary for the Zeeman slower, the MOT, the imaging system, and to shape the beams for optical potentials (Chapter 6). Finally, in a third table (located 10 meters away from the atoms) another laser system provides the blue detuned, far of resonance light necessary for the quantum reflection experiment.

In order to transport the beams from one table to the other we decided not to use optical fibers, mainly because of the loss of power. Instead, we send the beams directly through air, protected against air currents (and for safety reasons as well) by black-anodized aluminum pipes. Pointing instability can become a serious problem using this simple method for transport, but it can be minimized by proper optical imaging.

4.7 The Magneto Optical Trap

After the conclusion of the bakeout of the new chamber on June 7, 2003, we began assembling the optics while working on the magnetic trap. On June 26 we obtained the first MOT, and few days later we were capturing well over 10^9 atoms after four seconds.

We use six independent beams to form the MOT, instead of three retro-reflected beams, to avoid detriment in the capture efficiency due to absorption by the atomic cloud. Typically, the peak intensity in a single MOT beam is $I_0 = 11$ mW/cm^2. The total power for the repump is 60 mW, and is distributed to copropagate with the six MOT beams. Only about one third of this power is contained in the relevant sideband. The beams are all 1" in diameter, and they cannot be bigger due to the size of the penny window and the spacing between the recessed bucket walls. The light for both MOT and repump beams is spatially filtered to allow for good molasses imaging, necessary in the case of the quantum reflection experiments. The current in the quadrupole coils is 14 A, producing a gradient of 19 G/cm. At the time we started optimizing the MOT, we wanted to capture as many atoms as possible. In order to increase not only the number but also the atomic density in the MOT, we spent a few weeks implementing two solutions.

4.7.1 The dark spot MOT

The dark spot technique was developed by the group of Pritchard in 1993 [53]. Usually, despite the high flux provided by the Zeeman slower, the MOT is not able to capture a large number of atoms with high density. Light re-scattered spontaneously by the trapped atoms is emitted in all directions with no specific

polarization, leading to heating of the sample. The other source of heating at high densities is the collisions between atoms in ground and excited states [54]. The solution proposed by the MIT group was to block the repump light at the center of the trap, removing both sources of heating. Atoms outside the dark spot are cooled normally, and they experience a force towards the center of the trap. When the dark region is reached, they are quickly optically pumped into the dark ground state ($F = 1$ in the case of sodium). They stop scattering light as long as they remain in the dark spot. As they wander around they will eventually reach the bright region again, only to be pushed back into darkness. Atoms then start piling up at the center. In the first demonstration of the method, over 10^{10} sodium atoms were captured at densities close to 10^{12} cm^{-3} [53]. The JILA group added light that optically pumped the atoms into the dark ground state, improving the efficiency of the dark spot [126].

We implemented a dark spot in our experiment, by using two extra, independent, crossed repump beams with a shadow cast onto the atoms. The MIT group reports that using a single repump beam with a dark spot in the middle manages to capture over 10^{10} atoms at a density of 5×10^{11} cm^{-3} [127]. We found that a crossed set of beams with central shadows on each is more efficient. The shadow was formed by a piece of aluminum soldered to a thin copper wire. Care was taken to image the spot onto the atoms, otherwise a lot of unwanted diffracted light reached the center. Several sizes of spots were tried, between 3 and 13 mm, as well as several repump intensities. At the end, we managed to capture up to 2×10^9 atoms at a density of 6×10^{10} cm^{-3}, after a few seconds. The loading time was not much different than without the dark spot, leading us to believe that strong losses were still present. Losses

came mainly from stray repump light entering the MOT region, or reflecting off from one of the recessed walls inside the chamber.

We also tried to improve the efficiency of the shadow by superimposing a single, retro-reflected depump beam tuned 20 MHz below the ($F = 2 \longrightarrow F' = 2$) transition [128]. The capturing efficiency never improved, and it actually decreased for high powers (>2 mW).

4.7.2 Compressed MOT and Polarization Gradient Cooling

The second method implemented to increase the density was a small period of compression after loading. Without the dark spot we typically have 2×10^9 atoms. The shape of the MOT is elongated, and it changes from day to day. After loading the MOT, we lower the intensity of the repump light to 5% of its usual value, while the MOT light remains at 100%. The current of the quadrupole coil is then ramped from 14 up to 25 A in 1 msec , and it remains there for 7 msec. This produces an increase of a factor of three in the density, and a factor of 1.2 in the temperature. This period of compression is followed by 2 msec of Polarization Gradient Cooling (PGC). During PGC the magnetic field is turned off, and the level of MOT light is set to 40%, while the repump is 8% with respect to the full MOT value. At the end of these steps we produce a cloud of 2×10^9 atoms with a peak density close to 1×10^{11} cm^{-3}. The rms velocity of the atomic distribution is σ_v =8.0 recoils, or 24 cm/s.

After PGC cooling the repump light is turned off and the MOT light is left on for 500 ms for optical pumping into the $F = 1$ state. During this time no magnetic field is on. This results in about 30% of the atoms transferred into the magnetic trap in the $F = 1, m_F = -1$ state.

4.8 Magnetic Trapping

4.8.1 Introduction

Cooling by using optical methods based on spontaneous absorption and emission is limited by the recoil value[1]. Alternatively, far off resonance traps [131] have now been used to achieve quantum degenerate gases [132]. However, a very robust and practical method to obtain ultracold atomic samples is based on magnetic trapping and subsequent evaporative cooling. Magnetic traps were proposed as early as 1960, and the first experimental demonstration was done by W. Phillips group in 1985, trapping atomic sodium. In this chapter we describe the basis of magnetic trapping and evaporative cooling.

4.8.2 Principles

Magnetic trapping is based on the mechanical interaction of an external magnetic field with the total magnetic moment of an atom. The energy shift due to the interaction of a magnetic field $\mathbf{B}$ with the magnetic dipole moment $\bar{\mu}$ is,

$$U = -\bar{\mu} \cdot \mathbf{B}. \tag{4.14}$$

The complicated atomic structure simplifies in the case of the alkali atoms. The total magnetic dipole moment is just the sum of the nuclear, and orbital and spin contributions of the valence electron. In the case of the sodium atom, the unpaired electron has quantum numbers $n = 3$, $l = 0$, and the nuclear spin is $I = 3/2$. For small magnetic fields, it is possible to use the total angular

[1]Strictly speaking, this is not accurate. Sub-recoil temperatures have been demonstrated using methods based on selective spontaneous scattering and optical pumping [129, 130]. However, these procedures are involved, and limited in the achievable final three-dimensional velocity.

momentum $\mathbf{F} = \mathbf{J} + \mathbf{I}$, where $\mathbf{J}$ and $\mathbf{I}$ belong to orbital plus spin, and nuclear angular momentum respectively. The hyperfine structure ground state is a therefore a doublet with total angular momentum numbers $F = 1, 2$. The dipole moment of the atom is,

$$\bar{\mu} = \frac{\mu_B}{\hbar}(g_S\mathbf{S} + g_L\mathbf{L} + g_I\mathbf{I}), \tag{4.15}$$

where g_S, g_L, and g_I are the electron spin, electron orbital, and nuclear g-factors, respectively. The Bohr magneton is represented by μ_B. In the anomalous Zeeman regime, the energy shift due to the external magnetic field is less than either the fine or hyperfine structure energy splittings. It is then possible to write,

$$U = -m_F g_F \mu_B B_z, \tag{4.16}$$

where m_F is the Zeeman sublevel quantum number, and g_F the Landé factor.

In the presence of an inhomogeneous magnetic field the atom will experience a force:

$$\mathbf{F} = m_F g_F \mu_B \nabla |B|. \tag{4.17}$$

A very important assumption is implied in the writing of Eq. (4.17), namely, the adiabatic following condition. The condition states that the atomic motion is such that the magnetic dipole will follow changes in the magnetic field. A more precise statement will be given later in the context of Majorana transitions. The condition cannot be underestimated. In fact, it is a central point in any design of a magnetic trap.

To trap atoms it is necessary to have either a maximum or a minimum in the magnitude of the field. A local maximum in a region free of sources is prohibited in nature, as explained in Wing's Theorem [133]. Therefore,

the field configuration must have a local minimum, and the trappable states must have $m_F < 0$. Such hyperfine sub-levels are known as *low field seeking states*. In the case of sodium, these states are $3S_{1/2}(F = 1, m_F = -1)$, and $3S_{1/2}(F = 2, m_F = 1, 2)$. The $(F = 1, m_F = -1, g_F = -1/2)$ state is the more commonly used in magnetic trapping. The other two states present problems due to dipolar relaxation, which can be solved at the expense of a more involved experimental scheme [134].

The first geometry used to trap atoms magnetically is probably the simplest one: a spherical quadrupole field, generated by two circular coils with opposite currents [48]. The field has cylindrical symmetry, with linear gradients close to the middle point between the coils. Along the axial and radial directions the gradients are B'_z, and B'_ρ, respectively. They satisfy the relation $B'_z = 2B'_\rho$, due to symmetry and Maxwell's equation $\nabla \cdot \mathbf{B} = 0$. This trap has the problem of having a zero in the field at the center. Atoms that are moving slow enough may be aligned with the field, but as soon as they reach the zero crossing region they depolarize, and leave the trap. This is known as spin flips or Majorana transitions.

A task then is to avoid having atoms reach the zero crossing of the field, or avoid the zero at all. Three strategies were developed, and all are stable and robust enough to produce quantum degenerate gases. The first solution was to 'plug' the hole using a blue-detuned far off resonance beam, and this gave the first BEC in sodium [135] (recently the Georgia Tech group is reviving this technique [136]). The second alternative was to rotate the zero of the field on the radial plane between coils around the center. For fast enough rotation speeds the AC trap can be viewed as a DC trap with finite field at the center.

Such a scheme was used to produce the first BEC with ultracold atoms [137]. The last solution was the implementation of a DC magnetic trap, of the type known as Ioffe-Pritchard (IP) [138].

4.8.3 The Ioffe-Pritchard trap

The IP trap uses a quadrupole field in two dimensions, and a uniform field with a so called 'bottle' curvature in the third dimension [139]. Ideally, the quadrupole field in the XY plane can be created using four parallel wires carrying currents in alternate directions. Confinement along the $\hat{z}$ direction is achieved with two circular coils carrying currents in the same direction, but with a larger separation compared to the Helmholtz configuration (the 'pinch-off' coils). This not only produces the curvature in the field necessary for confinement, but also a bias field at the center.

The magnetic field of a magnetic trap of the IP type is:

$$\mathbf{B} = B_0 \begin{pmatrix} 0 \\ 0 \\ 1 \end{pmatrix} + B'_\rho \begin{pmatrix} x \\ -y \\ 0 \end{pmatrix} + \frac{1}{2} B''_z \begin{pmatrix} -xz \\ -yz \\ z^2 - \frac{1}{2}(x^2+y^2) \end{pmatrix}, \tag{4.18}$$

where the first and last terms come from the 'pinch-off' or curvature coils, and the second from the quadrupole coils alone. The magnitude of the magnetic field $|\mathbf{B}|$, can be expanded in $\mathbf{r}$ around zero, keeping terms up to second order:

$$|\mathbf{B}| \simeq B_0 + \frac{1}{2} B''_z z^2 + \left(\frac{B'^2_\rho}{2B_0} - \frac{B''_z}{4} \right) (x^2 + y^2). \tag{4.19}$$

The harmonic approximation is valid for small clouds. Some of the neglected terms in the expansion imply

$$\begin{aligned} \frac{B'_\rho B''_z}{B_0^2} x^2 z &\ll 1 \\ \frac{B''^2_z}{4B_0^2} x^2 z &\ll 1. \end{aligned} \tag{4.20}$$

For an order of magnitude estimate of the length at which the harmonic approximation breaks down, we can set from Eq. (4.20): $\xi \ll \sqrt{2B_0/B_z''}$, where ξ is a typical length. It can also be written as $\xi \ll \sqrt[3]{B_0^2/(B_z'' B_\rho')}$. Typical values for our magnetic trap are $B_0 = 3$ G, $B_\rho' = 300$ G/cm, and $B_z'' = 120$ G/cm^2. The first condition gives $\xi \ll 2.2$ mm, while the second yields $\xi \ll 650\,\mu$m. In our experiment, these values are easily satisfied for atomic samples with lower temperatures than 15 μK.

From Eqs. (4.19) and (4.16), it is possible to obtain the trap oscillation frequencies in the harmonic approximation:

$$\omega_{\rho,z} = \sqrt{\frac{\mu B_{\rho,z}''}{M}}, \tag{4.21}$$

where $\mu_B g_F m_F = \mu$. The effective radial curvature is given by

$$B_\rho'' = \left(\frac{B_\rho'^2}{B_0} - \frac{B_z''}{2} \right). \tag{4.22}$$

One last point is worth mentioning here. The harmonic approximation is valid for very cold samples, but it can break down for certain sets of currents. To see this we consider the magnitude of the field in the XZ plane, from Eq. (4.18):

$$\begin{aligned} |\mathbf{B}(x,z)| &= \sqrt{\left(B_0 + \frac{1}{2} B_z'' \left(z^2 - \frac{1}{2} x^2 \right) \right)^2 + \left(B_\rho' x - \frac{1}{2} B_z'' x z \right)^2} \\ &= \sqrt{B_0^2 + f(z) + \left(\frac{1}{2} B_z'' x^2 \right)^2 + x^2 \left(B_\rho'^2 - B_z'' B_\rho' z - \frac{1}{2} B_0 B_z'' \right)}, \end{aligned} \tag{4.23}$$

where $f(z)$ is a function of z only. Confinement along the X direction is lost wherever

$$z < \frac{B_\rho'}{B_z''} - \frac{B_0}{2B_\rho'}. \tag{4.24}$$

The instability points are always present, and care is required to have relative currents in the coils that push these points as far as possible form the atomic cloud.

4.8.4 Adiabatic following

Having a non-zero value of the magnetic field at the center is no guarantee to avoid spin flips. In the presence of an external field, a magnetic dipole will precess. The condition is that the magnetic dipole of the atom can follow the changes in the field:

$$\mathbf{v} \cdot \nabla \left(\frac{\mathbf{B}}{|\mathbf{B}|} \right) \ll \nu_{\mathrm{Lar}}, \tag{4.25}$$

where ν_{Lar} is the Larmor frequency, and $\mathbf{v}$ the velocity of the atom. To estimate the necessary field, we rewrite: $\mathbf{v}(h/\mu) \cdot \nabla|\mathbf{B}|/ \ll |\mathbf{B}|^2$. The gradients in our trap during evaporation are on the order of 300 G/cm, and typical velocities of the atoms are less than 25 cm/s ($\sim 8\, v_{\mathrm{r}}$). The value for μ, in the case of the $3S_{1/2}(F = 1, m_F = -1)$ state of sodium, is $1/2\, \mu_B$. Therefore, the magnitude of the bias field must be larger than 100 mG. Under typical working conditions, the value we use is about 3 G.

4.8.5 The cloverleaf coil

There are several designs for a magnetic trap of the Ioffe-Pritchard type: ying-yang, 4-dee, QUIC-trap, baseball, etc. ([140] and references therein). Any of these designs works and has good and bad points. During our first set of experiences with magnetic trapping we used a baseball trap. The trap is formed from a winding resembling the stitches of a baseball, which produces not only the transversal quadrupole but also the axial curvature. Our trap

had 9 turns, used up to 350 A of current, and produced gradients on the order of 160 G/cm. It was mounted over the glass cell on top of the chamber. As we already mentioned, atoms were transferred from one MOT in the center of the chamber to another MOT in the glass cell. Up to 5×10^8 atoms were captured in this MOT, and about 25% of them transferred to the magnetic trap. The frequencies of the trap were 225 Hz radially, and 10 Hz axially, using a 1 G bias field. The lifetime of the atomic sample in the trap was about 40 s. Evaporative cooling using this configuration was extremely inefficient, due to a combination of low atom number and weak magnetic confinement. Despite efforts to improve any of the numbers stated above, after a few months we decided to change the design of the chamber to house another magnetic trap.

For the new trap, we use a cloverleaf design. The cloverleaf trap was developed by the group of W. Ketterle, and it was the first DC magnetic trap to obtain a BEC, using sodium [138]. Our design is based on a similar set of coils used in one of the recent BEC machines at MIT [141]. This trap has the enormous advantage over other designs of having a planar geometry, thus allowing for 360 degrees of optical access. Because the coils cannot be arbitrarily close to the atoms, the currents needed are on the order of 500 A. The trap consumes about 11 kW of power during normal operation. However, it is not difficult to implement, requiring only patience and care.

The cloverleaf trap takes its name from the resemblance of the arrangement of its coils with a cloverleaf, Fig. 4.10. The resulting fields from such a configuration are not intuitive, but they are easily understood after considering the following. The task is to produce a quadrupole field on the side of a planar structure. A simple circular coil cannot do this. Adding a second half

with opposite current will not help, because we would end up having the original spherical quadrupole, with the Majorana losses due to a zero in the field. The MIT team solved the problem of increasing the gradients by breaking the symmetry of the configuration [142].

We start with the simple circular coil, Fig. 4.9 (b), but it is then pinched in one direction, Fig. 4.9 (b). The gradients created on the plane parallel to the coil will not have the same magnitude. Let another of these pinched coils to be superimposed to the first one, and let their long axes be perpendicular to each other. Also, we require the coils to have currents flowing in opposite senses. If the first coil produced a field pointing, say, outwards, the field of the second coil will point inwards. The predominant field will be that of the short axis, with very little contribution from the (opposite) long axis. This procedure has created a quadrupole, planar field in XY, Fig. 4.9 (c). Along the Z axis the field is zero. Adding a second half with identical coils but opposite currents will double the gradient. All that is left to do is to add a set of pinch off coils along the axial direction to have again an IP type trap with strong gradients.

The configuration just described can be easily transformed into the final cloverleaf arrangement (Fig. 4.10). Eight small coils produce the linear gradients on the XY plane. Two circular coils (curvature), produce the gradient along the axial direction. To adjust the bias field produced by the curvature coils along Z, two more coils (anti-bias) are added. It was necessary to include two more sets of coils to oppose the large field created by the curvature coils. The first one is called the trombone. The second one, the bias coils, carries only a few amps of current, and provides fine tuning of the bias field B_0.

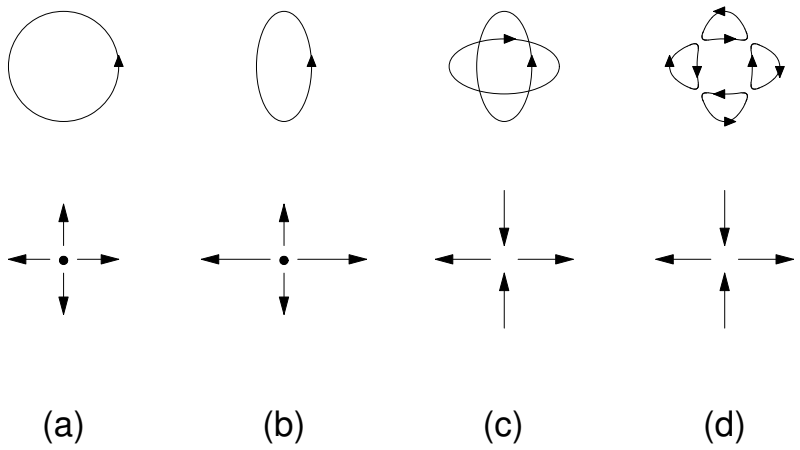

Figure 4.9: Origin of the quadrupole field created by the cloverleaf coils. The upper row shows current carrying wires, while the second indicates the magnetic field produced on a plane parallel to the plane of the coils (XY). (a) A circular coil produces a field that has a strong component along Z (represented by a central dot). (b) A pinched coil still produces similar fields but asymmetric. (c) The addition of a similar coil with opposite current and orientation produces a quadrupole field along XY, and cancels the field along Z. (d) The configuration of (c) can be thought of as 4 independent coils, the cloverleaves.

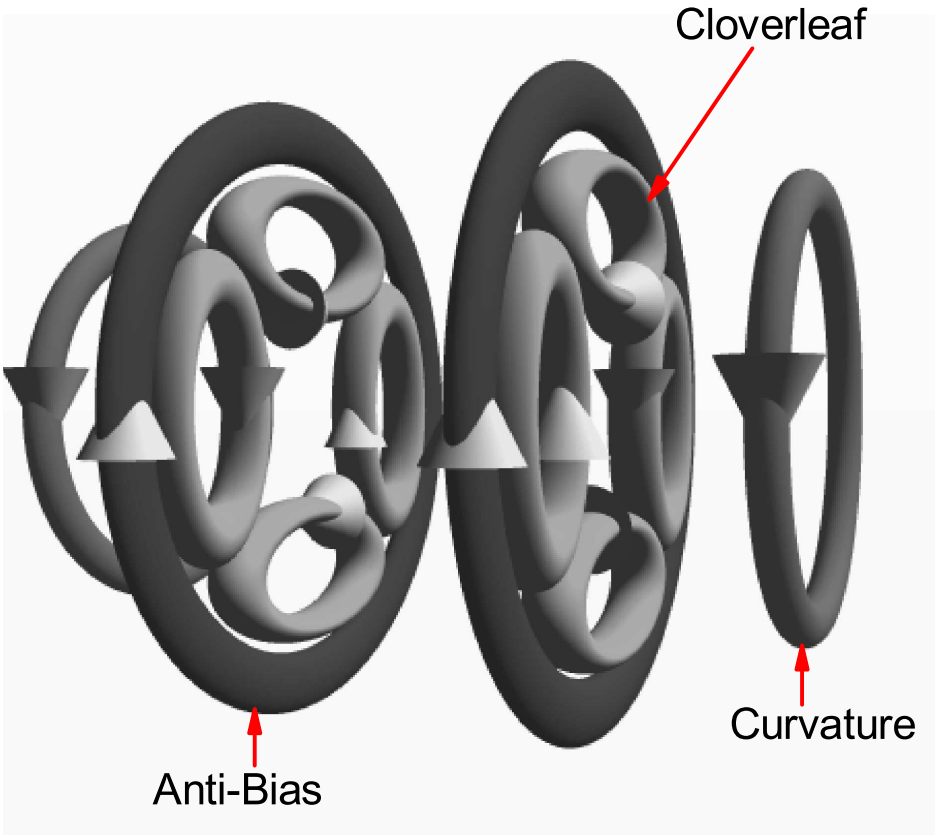

Figure 4.10: The arrangement of the coils for the cloverleaf magnetic trap. The quadrupole gradients are produced by eight cloverleaf coils. Confinement along the axial direction is created by two pinch-off coils (curvature). The bias field produced by the curvature coils is canceled with two coils in the Helmholtz configuration (anti-bias).

4.8.6 Design and construction

The sets of coils were arranged to maximize the filling of the space available. In order of importance, the gradient coils were made first. They are also the closest to the atoms, to maximize the gradients. The curvature coils, and then the anti-bias-trombone set, are also important, but less critical.

The necessary fields require currents of 500 A for the gradient coils, and about 100 A for the curvature and compensation coils. Water cooling is necessary, so hollow copper tube is used. In our previous baseball trap we used circular cross section tubing, which doesn't fill space efficiently. Following the experience of the MIT team, we used a squared cross section instead. At the time we were looking into buying materials, we found out that our neighbors (Professor Dan Heinzen's Lab) had a quantity spared of the required tubing. They had just finished constructing their own sets of coils for a cloverleaf magnetic trap in their rubidium BEC experiment. We were very fortunate to have Professor Heinzen letting us use well over 100 meters of the tubing on 'permanent loan'. This saved us weeks in time, and the effort they went through in having the copper coated with insulating fiberglass material.

The tubing (Small Tube Products) is made from soft tempered copper alloy 101; with 1/8" OD, and 0.032" wall thickness. The insulation was done by Essex Group Magnet Wire & Insulation, using spun glass fiber. The measured electrical resistivity is 2.75 mΩ/m. The coils were not very difficult to wind, with the exception of the cloverleaves. The main problem was that a winding acts as a spring. If not kept tight, the coil will unwind and even a slight relaxation may destroy completely the carefully planned dimensions. This is a serious problem if all the coils are to fit together with tolerances on the order

of 25 mils. In order to prevent unwinding, individual coils are glued using 5 min epoxy Quik-Stik. During application, coils were pre-heated using a heat gun and epoxy added. This not only helped for better curing of the epoxy but allowed it to flow nicely through the tubing, maximizing contact.

1. Cloverleaves (Gradient). These coils took the longest to make, mainly because the precision required, and the size. A single coil has 12 turns, 4 radial and 3 axial. Its shape is oval, rather than a circle, to maximize the field gradients. The inner axes' dimensions are 0.85"×0.22", while for the outer ones we have 2.10"×1.34". The thickness is 0.44". The average length of each coil individual is 1 m (1.45 m). Numbers in parenthesis indicate total length including leads.

2. Curvature. The coils are circular in shape, 1.32" ID, and 2.94" OD. They have 6 radial by 8 axial turns, and have 1.14" in thickness. Because they are mounted right behind the gradient coils, the most critical part of this coils is the inner diameter, as they have to slide over the penny window (OD 1.25"). The length for each coil is 8.4 m (9.2 m).

3. Anti-Bias. The critical dimension for these coils was the diameter, as they had to slide into the 6" diameter bucket of the vacuum chamber, but also house the gradient coils. Final dimensions were 4.22" ID, and 5.9" OD, for 18 turns, 6 axial and 3 axial. Thickness is 0.44", and length 7m (8.2 m) per coil.

4. Quadrupole. Another coil was made to fit around the curvature coil. The original purpose is to have a high current coil that can be helpful

in adding strong magnetic field in necessary cases like Feschbach resonances. It is a circular coil 3.1" ID and 4.8" OD, divided in two layers to improve the cooling. The inner layer has 28 turns, 4 radial by 7 axial. The second layer has 2 radial turns by 7 axial. Thickness is 1.00", and total length for both layers 13 m (14.3 m). Currently we use this coil to produce the MOT quadrupole field.

5. Trombone. Serving the same purpose as the Anti-Bias coil (to cancel the huge axial bias field created by the curvature coils), the trombone was not in the original design of the trap. It was added later to minimize heating created from current fluctuations in the power supplies (see Section 4.8.8). Each of the trombone coils has 19 turns, and it is mounted separately from the rest of the trap outside the bucket. It has its own supporting structure, a semi circular aluminum channel bolted onto the chamber using the extended nuts welded around the bucket. Length per coil is 13.4 m.

Mounting the coils together. The cloverleaf coils were arranged to fit in the space between the inner diameter of the anti-bias coil and a 1.32" OD rod at the center, simulating the penny window. The coils were glued together using Epoxy Glue from GC Electronics, a 24 h curing grey glue (as opposed to five-minute clear Quik Stik). Once cured, this type of epoxy provides a much stronger bond than five-minute epoxy. Wherever it was possible, we put a phenolic prototype board to provide additional support for the joints cloverleaf-anti-bias coils. To this phenolic board three nuts were also glued with three 1/4-20, 3" long threaded rods attached for mounting purposes. The rods and the nuts were made from brass, a non magnetic material.

Right on top, where the cloverleaves join at the center, the curvature coil was placed and glued. Up to this point all the coils are in close fit together, with windings from one coil touching windings from another. The quadrupole coil was next, but we regard this coil not as critical as the previous three. Therefore, it was glued around the curvature coil, on top of the phenolic board and also on top of the leads coming out from the cloverleaves. Once all coils were in place, additional grey epoxy was used to fill most of the voids. At the end we had a monolithic structure with 16 leads coming out.

To mount the coils onto the chamber we attached a 1/2" thick lexane board to the three 1/4-20 brass rods. Layers of sorbothane were laid in between coils and lexane to gain some uniformity in pressing. A second lexane board was attached to the first one, with slotted arcs coinciding with the positions of the 1/4-20 long nuts welded onto the chamber around the bucket. These slots allowed for small necessary rotations to align the two halves of the trap. Prior to mounting the trap onto the chamber, a 25 μm thick layer of kapton film was adhered to the front end of the trap, covering both cloverleaves and anti-bias coils. This prevents the development of any possible electrical shorts between the coils and the chamber.

The lexane was firmly bolted onto the chamber using 9 1/4-20 screws. This type of mounting, together with the mount of the leads for electrical connections and the water lines, made the trap insensitive to small vibrations from the water booster pumps or the turbo pump in the oven chamber.

4.8.7 Connections and cooling

Electrical connections. The cloverleaf coils were interconnected by extend-

ing the leads of the coils about 20 cm away from the chamber, and towards the center. This was done to minimize stray fields along the axial direction that could change the bias field B_0 as a function of current in the cloverleaves. To each lead a small copper bracket was soldered. The copper bracket is a rectangular piece 1" long by 0.5" wide, and 0.25" thick. It has a 1/8" slot on the side, and two through holes for mounting. Insulation at the end of the leads was removed, and the bare tubing placed in the slot of the bracket, where it was soldered. This transition from the square-shaped hollow tube to a copper tab was very effective. In this way we connect leads with one another. To connect the leads with cable going to the power supplies we use slightly wider copper pieces, to accommodate a through hole for a 1/2" bolt.

All the leads going to cables are gathered in two aluminum structures that firmly support plexiglass squares, to which the copper tabs are bolted using two 1/4" screws. The cables used to connect the coils to the power supply are 3/0 welding cable (Graybar 2003/02), with 600-24 AWG stranded wire. The insulation for the cables we used was either rubber with fiber glass, or simply rubber. Because these wires are not cooled, after a few hours of use at high currents (500 A) they can get very hot (50 °C). We had to double the wires on each connection for the cloverleaves only, as they carry the highest currents.

Water connections. The end of the current carrying copper tubing leads were shaped round using a lathe tool mounted on a regular hand held drill. To this round-shaped ends swagelock connectors were attached to connect them to the water lines. Tubing 1/4" OD was used only for small sections (30 cm) to avoid further pressure drop, and then all sections joined in a manifold that

Coil	Resistance [mΩ]	Flow [ml/min]	Number	Power [kW]
Cloverleaf	4	900	8	7.5
Curvature	26	375	2	0.6
Anti-Bias	23	425	2	0.5
Trombone	37	400	2	0.8
Quadrupole	40	400	2	0.02

Table 4.1: A summary of properties for the magnetic trap coils. The resistance refers to each individual coil, while the total dissipated power takes into account all of the same type.

connected to a 3/8" OD tubing. Two such manifolds were used on each half of the trap, for incoming and outgoing water. Using large diameter tubing is important to minimize pressure drops along the lines.

The water cooling of the coils is done by a closed loop heat exchanger, together with booster pumps to increase the flow. Distilled water must be used. The heat exchanger (Affinity, EWA-04AA-CE56CB) has a cooling capacity of 20 kW, but the flow is not very high due its low pressure pump (50 psi). The pumps added (Tuthill, TXS2.6PPPT3WN1C000) help in increasing the flow considerably, but they produce a lot of mechanical vibrations. Therefore, the motors of the pumps are used only at about one third of its maximum speed, and pulsation dampers (FlowGuard) are placed immediately after the pumps. For cooling purposes each of the individual coils of the trap are connected in parallel. We use one booster pump for each half of the trap. The pressure of the running water is about 125 psi; the corresponding flow rates are found in Table 4.1. The total power dissipated in the trap is about 12 kW (coils plus switching IGBT's and diodes). At the quoted flow rates, the temperature of the water goes from 17 to 37 degrees Celsius after 30 s of maximum current.

The final parameters of the trap were determined by using a gaussmeter

probe, and also by measuring the radial trapping frequency by displacing the atomic cloud (see Section 5.5.1). The parameters found with the probe are:

$$\begin{aligned} B'_\rho &= 0.6\,\mathrm{G/cm} \\ B''_z &= 1.2\,\mathrm{G/cm^2}. \end{aligned} \tag{4.26}$$

4.8.8 Control electronics

The electronics controlling the magnetic trap can be divided in two parts: high and low current. The high current elements carry up to 500 A, dissipating up to 2 kW of power, therefore needing water cooling and special care. The low current circuitry involves interfacing between the computer and the high current side.

High current. The beginning of the design for the high current circuit was the choice for the required power supplies. While there is more than one company that quotes specifications of less than 0.5% ripple noise, our choice was based on previous experience from two different BEC projects [116, 143]. We use two models from Lambda EMI: the ESS30-500-2-D, and the ESS20-500-2-D. The first supply is used to drive the cloverleaves only, while the second one drives the rest of the magnetic trap coils. The rms ripple noise quoted is about 0.1%. We note, however, that there seems to be switching noise in the output, as we observe a strong signal at 250 kHz that can be seen even with a pickup coil a meter away form the power supply. This was of some concern at first, and we tried to minimize this signal without much success. Because it is a frequency outside the spectrum of relevant frequencies for the magnetic trap, we left the problem unsolved. The achievement of a healthy BEC in our experiment is proof enough to ignore the oscillations.

The controlling circuit for the cloverleaves is the simplest, and is shown in Fig. 4.11 (a). The output of the power supply goes to a forward biased diode (POWEREX CS641230) connected in series with the coils. After the coil an IGBT is used as a switch, and its emitter connects back to the power supply. The diode (in reality two diodes in parallel) is used to protect the power supply at the current switch off. The diodes also help in reducing the turn-off times by suppressing the loop of current flowing back into the power supply direction. Additional protection is given by using varistors (300 V rms) in several places, not only across coils but also between coils and ground. We use two IGBT's (POWEREX CM600HA-24H) in parallel, to avoid overheating and burning of a single element. When purchasing the IGBT's they must be matched for use in parallel. For cooling we mount the pair of diodes or IGBT's in a single copper plate, with 1/4" OD copper tube brazed in and silver soldered at the bottom. The tubing forms several loops, and carries water at 8 °C. The diodes or IGBT's are mounted and bolted onto the copper plates, using conductive paste in between. During regular use their temperature never exceeds 40 °C.

The circuit for the curvature, anti-bias, and trombone coils (ABCT) also uses forward biased diodes, and an IGBT for switching purposes (Fig. 4.11 (b)). All three coils are in series, and there is a MOSFET bank in parallel with the trombone coil that acts as a variable shunt resistor, used to adjust the bias field (B_0). The bank has twenty MOSFET's (International Rectifier IRFP054N) in parallel, mounted on a water cooled copper plate. In the past, we have used exclusively such banks as a switch for high currents, but we decided to change to IGBT's because they are much simpler to handle.

Low current. The current in the cloverleaves, curvature, and anti-bias coils

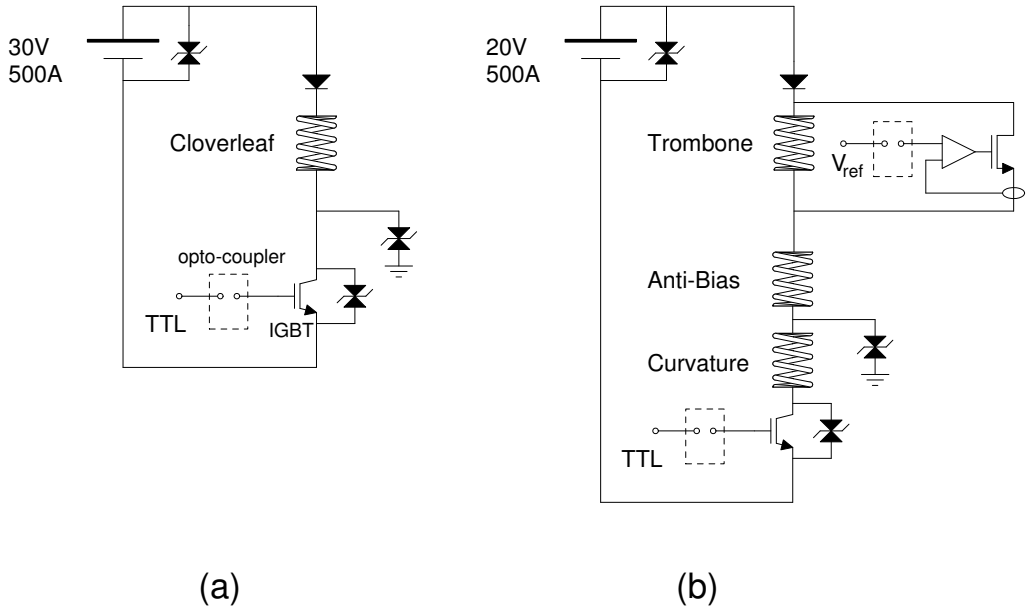

Figure 4.11: A schematic of the electrical circuit used for the magnetic trap coils. (a) The circuit for the cloverleaf is the simplest. The power supply is operated in the constant current mode, and an IGBT is used for switching purposes. During switch-off a forward-biased diode prevents current loops, and varistors are located at various places to absorb the power and prevent possible shorts. (b) The circuit used for the ABCT system is very similar. The current across the trombone is regulated by using a feedback loop on a shunt 'resistor'. See the text for details.

can be controlled directly by the power supplies in the constant current mode. The supplies have two analog inputs, for current and voltage. The driving voltages are provided by an analog output board controlled by the computer. Between any of the computer controlled analog or digital outputs, and power supplies or circuits controlling the magnetic trap, there is a stage of opto-isolators. The use of the opto-isolation avoids ground loops and prevents damaging of the analog and digital output electronics, and even the computer, due to voltage spikes at currents switch off. The analog opto-isolator circuit, together with its digital counterpart was developed by Todd Meyrath for our neighbor rubidium BEC experiment. We were fortunate to have his design ready and fool proof. The shunt MOSFET in parallel with the trombone coil is controlled by a feedback loop that measures the current across the MOSFET bank using a Hall sensor (CLN-300 FW Bell), and compares the corresponding voltage to a reference provided by a computer controlled analog output.

While originally the circuits for each power supply were designed to be floating with respect to each other, we now have a short between one gradient and one of the anti-bias coils that voids this. The short effectively clamps a voltage reference between the circuits. Other than that, the short (determined to be at a single point) does not affect the performance of the magnetic trap. We also produced involuntary sparks between the magnetic trap and the vacuum chamber when turning the trap off. This happened because of extreme proximity between some of the coils with the chamber. Wherever possible, we inserted layers of electric insulating material. When this was not possible, installing a varistor between the coil in question and a good ground solved the problem.

4.9 The transfer of atoms to the magnetic trap

During the transfer of atoms from the MOT to the magnetic trap, the curvature of the potential has to match the corresponding size of the atomic distribution. An incorrect match will either heat the atoms or decrease the density, which is detrimental to the most important parameter during evaporative cooling, namely, the elastic collision rate [140]. After the transfer, the atomic cloud is compressed to increase collisions. In Fig. 4.12 we plot the magnitude of the field for an IP trap in the two configurations. We notice that, while the potential is not exactly symmetric along the radial direction (X axis), radial symmetry becomes an excellent approximation for very cold clouds.

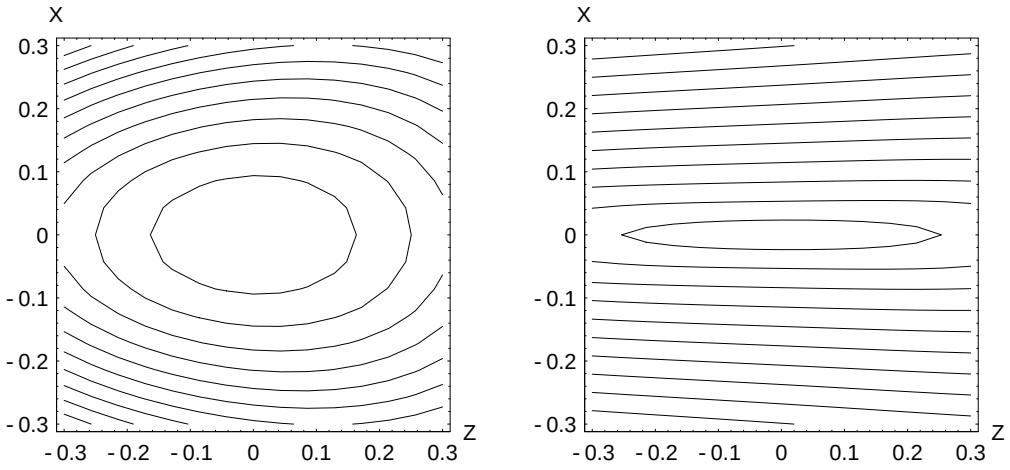

Figure 4.12: A contour plot for the magnitude of the trap magnetic field. (a) During transfer of atoms from the MOT to the trap the currents are adjusted to match the atomic size. (b) After the transfer the cloud is compressed to increase the collision rate. The units for both axes are cm.

The compression of the cloud after transfer has to be adiabatic, to ensure conservation of phase space density. The basic condition to be satisfied

is:

$$\frac{1}{\omega^2}\frac{d\omega}{dt} \ll 1. \tag{4.27}$$

In our experiment we increase the radial frequency from $\omega_\rho = 2\pi$ 35 to $\omega_\rho = 2\pi$ 334 Hz over 1 s, by ramping various currents up linearly (Section 5.4). The frequency change is not linear, but the calculated coefficient on the left of Eq. (4.27) never exceeds the value 0.01.

4.10 Evaporative cooling

On July 7 2003 we tested the magnetic trap for the first time. Shortly thereafter, we found lifetimes in the trap slightly under 1 min, sufficient to begin evaporation. This technique was first demonstrated by Kleppner and Greytak using atomic hydrogen in a magnetic trap [144]. Cooling was achieved by lowering the trapping fields. In a refined version of the technique, Ketterle and coworkers implemented evaporation by using radio frequency (rf) fields on magnetically trapped atoms [135]. Evaporative cooling can also be realized in an optical trap [145], a technique that allowed the achievement of Bose–Einstein condensation by all-optical means [132]. Recently, another method has also been discovered to work, by using surfaces adsorbing high energetic atoms from a magnetic trap [146].

A good review of evaporative cooling can be found in reference [147]. The basic idea of any kind of evaporation is simple. A collection of particles confined in a trap has some velocity distribution. If it is possible to eject out some of the most energetic particles from the trap, the total energy of the ensemble would be lowered. After removal, the system is allowed to reach equilibrium through inter-particle collisions. The repeated execution of these

steps effectively lowers the temperature of the sample, at the expense of lowering the particle number. It is the balance of the fraction of atoms removed per step and the time it takes afterwards for equilibration that determines the success in the goal of increasing phase space density. Phase space density is defined as the product $n\lambda_{\mathrm{dB}}^3$, where n is the density and $\lambda_{\mathrm{dB}} = \sqrt{2\pi\hbar^2/Mk_{\mathrm{B}}T}$ the de Broglie thermal wavelength for an atom with mass M.

Different models have been proposed to optimize evaporation [135, 148, 149, 150]. In a piecewise picture, from an atomic distribution at temperature T, all the atoms with energies higher than $\eta k_{\mathrm{B}}T$ are removed. The truncation parameter is optimum around the value $\eta = 6$ for a 3D harmonic potential [147]. The remaining atoms will collide with each other to redistribute the energy until thermal equilibrium is achieved. The time it takes for this to happen is about 4 elastic collision times [151]. The elastic collision rate is given by

$$\gamma = n\sigma_c\langle v\rangle, \tag{4.28}$$

where n is the density, $\langle v\rangle$ is the relative velocity between atoms, and σ_c is the s-wave collision cross section. For estimating purposes in this thesis we always use the peak density, and the rms velocity of the distribution. In the case of sodium atoms in the $(F = 1, m_F = -1)$ state the collision cross section is equal to $\sigma_c = 8\pi\,(2.75\,\mathrm{nm})^2 = 1.9 \times 10^{-12}\mathrm{cm}^2$ [152]. For evaporation to work, the elastic collision rate has to be high enough to neglect the intrinsic, background gas limited lifetime of the atoms in the magnetic trap. The limitation for evaporation is the ratio of the so called 'good collisions' (elastic, s-wave interactions that leave the atoms in unchanged spin states) to 'bad collisions'. The latter kind of interactions includes background collisions, spin exchange

and dipolar relaxation [147]. A third source for heating comes from three-body recombination, which is generally important only at very high densities ($> 10^{13}\mathrm{cm}^{-3}$).

Clearly, if the lifetimes are orders of magnitude longer than the collision time, the evaporation will be very efficient. In order to have sustained evaporation, the collision rate has to remain the same or increase, and this is called 'runaway evaporation'. To be in the runaway regime, it is necessary to have at least 200 collisions per trapping lifetime [147].

4.10.1 RF evaporation

In rf evaporation, atoms are ejected from the magnetic trap by imposing a radio frequency. In the unperturbed trap, atoms are in a particular low field seeking state, the $m_F = -1$ in the case of sodium. The frequency of the rf is tuned to be in resonance with the adjacent hyperfine sublevels, therefore changing the state of the atom from a trapped to an anti-trapped state. In an harmonic trap, position is correlated with the energy, so this rf 'knife' can eject hot atoms very selectively by changing the frequency. In practice the method works very well and is robust.

The atom in the presence of rf radiation inside a magnetic trap is nicely described in terms of dressed states, as we now proceed to show. The discussion will be based on reference [91], and on notes from an Atomic and Molecular Physics course by Prof. Dan Heinzen.

The dressed atom picture considers the radiation field not as a perturbation, but as part of the system. The Hamiltonian H consists of an atomic part H_{A}, a light field H_{L}, and the interaction term H_{AL}. Solutions for H are

found using a particular basis. We consider an atom with total angular momentum $F = 1$, and Landé factor $g_F = -1/2$. Therefore, the low field seeking state has $m_F = -1$. The basis for the atomic states $|F, m_F\rangle$ are those of an angular momentum system, eigenstates of the dimensionless operator F_z:

$$F_z|F, m_F\rangle = m_F|F, m_F\rangle. \tag{4.29}$$

Because the magnetic field due to the trap is static, it can be treated classically. It is incorporated into the atomic structure of the m_F sublevels:

$$H_{\rm A} = -\hbar\omega_0(\mathbf{r})F_z, \tag{4.30}$$

where $\omega_0(\mathbf{r}) = \mu_B|g_F||B(\mathbf{r})|/\hbar$ reflects the frequency shift of the levels due to the trapping field.

The basis of the radiation field is formed by the eigenstates of the number operator $N = a^\dagger a$:

$$H_{\rm L} = \hbar\omega a^\dagger a|n\rangle = n|n\rangle. \tag{4.31}$$

Therefore, we use the set of states $|m_F, n\rangle$ as our basis for the combined problem. The rf field of frequency ω, and polarization along $\hat{x}$ can be expressed in quantized form:

$$\mathbf{B}_{rf} = \hat{x}\left[ba + b^* a^\dagger\right], \tag{4.32}$$

using the Schrödinger picture. The interaction term is again dipolar in nature:

$$\begin{aligned} H_{\rm AL} &= -\bar{\mu}\cdot\mathbf{B}_{rf} \\ &= \mu_B|g_F|F_x\left[ba + b^* a^\dagger\right]. \end{aligned} \tag{4.33}$$

It is possible to write $F_x = \frac{1}{2}(F_+ + F_-)$, using the ladder operators $F_\pm = F_x \pm F_y$. The matrix elements of the interaction Hamiltonian are:

$$\begin{aligned}\langle m_F, n|H_{AL}|m'_F, n'\rangle &= \frac{1}{2}\mu_B|g_F|\langle m_F, n|(F_+ + F_-)(ba + b^*a^\dagger)|m'_F, n'\rangle \\ &= \frac{1}{2}\mu_B|g_F|\left(\langle m_F, n|F_-ba|m'_F, n'\rangle + \langle m_F, n|F_+b^*a^\dagger|m'_F, n'\rangle\right) \quad (4.34) \\ = \frac{1}{2}\mu_B|g_F|&\left(b\sqrt{n'}\delta_{n,n'-1}\langle m_F|F_-|m'_F\rangle + b^*\sqrt{n'+1}\delta_{n,n'+1}\langle m_F|F_+|m'_F\rangle\right),\end{aligned}$$

where we have used the rotating wave approximation [91]. The ladder operators increase or decrease the angular momentum by one unit. We therefore have kept only those terms in which the m_F number decreases (increases) by one unit while an rf photon is created (annihilated). Using the basis $|F, m_F\rangle$, the ladder operators for a spin 1 system are

$$F_+ = \sqrt{2}\hbar\begin{pmatrix} 0 & 1 & 0 \\ 0 & 0 & 1 \\ 0 & 0 & 0 \end{pmatrix}, \; F_- = F_+^T. \quad (4.35)$$

In the case where the rf field strength is large, we can take $\sqrt{n+1} \simeq \sqrt{n}$. An arbitrary choice of time origin sets b to be real. Finally, we put the interaction energy in terms of the Rabi frequency: $\mu_B|g_F|b\sqrt{n} = \hbar\Omega$. The final matrix form of the total hamiltonian $H = H_A + H_L + H_{AL}$ will have blocks of 3×3 elements along the diagonal, and zeros everywhere else. Using all the previous substitutions, from Eqs. (4.29), and (4.35), we obtain for the n$^{\text{th}}$ block:

$$H = \hbar \begin{array}{r} \\ \langle -1, n-1| \\ \langle 0, n| \\ \langle 1, n+1| \end{array} \begin{array}{c} \begin{array}{ccc} |-1, n-1\rangle & |0, n\rangle & |1, n+1\rangle \end{array} \\ \begin{pmatrix} \omega_0 + \omega(n-1) & \Omega/\sqrt{2} & 0 \\ \Omega/\sqrt{2} & \omega n & \Omega/\sqrt{2} \\ 0 & \Omega/\sqrt{2} & -\omega_0 + \omega(n+1) \end{pmatrix} \end{array}. \quad (4.36)$$

Finally, the eigen-energies of the dressed states become:

$$E = \begin{cases} \hbar n\omega \\ \hbar n\omega \pm \sqrt{(\omega_0 - \omega)^2 + \Omega^2}. \end{cases} \quad (4.37)$$

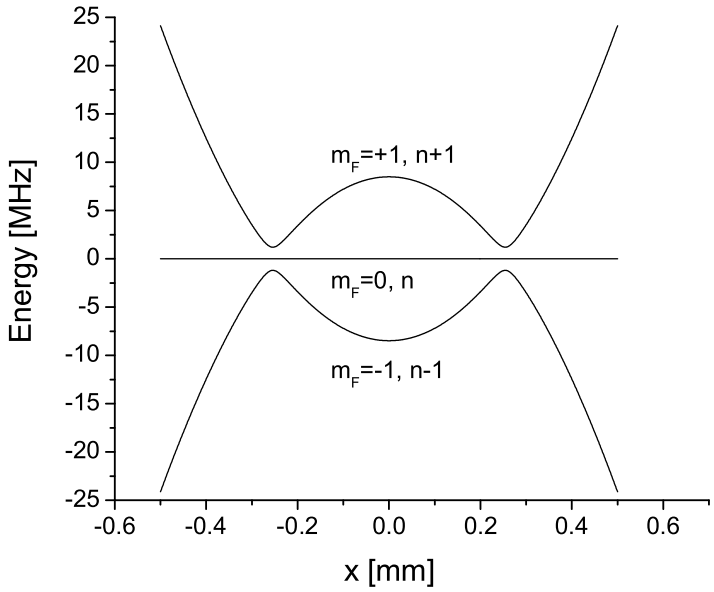

Figure 4.13: The dressed-picture of the potential experienced by a sodium atom in a magnetic trap under the presence of a rf field. For this figure $B_0 = 2.3$ G, and the radial frequency is 338 Hz. The rf frequency is $\omega = 2\pi\, 10$ MHz, and the amplitude has been adjusted to make the avoided level crossing clear. The quantum numbers shown at the center correspond to the limit where there is no interaction with the rf field.

In Fig. 4.13 we show a plot of the energy levels for actual parameters of the magnetic trap (only the rf field amplitude is adjusted to make the effects clear). Without the interaction term the levels are degenerate exactly at the point where $\omega = \omega_0$. The middle sublevel has n rf photons and $m_F = 0$, while the other sublevels have $n \pm 1$ photons with $m_F = \pm 1$, respectively. In the complete, dressed atom picture the degeneracy is lifted, and the levels avoid crossing each other. The separation of the levels at that position is equal to $\hbar\Omega$. This indicates that the reduction of the well depth due to the rf radiation is more or less linearly dependent on the strength of the field. However, the probability for tunneling through the energy gap is exponentially dependent on

the separation of the levels (Landau-Zener tunneling [20, 19]). The adiabatic following from trapped to anti-trapped states is therefore easy to achieve, and that is why rf evaporation works so well.

In our experiment we use an rf coil inside vacuum. The coil, described in Section 4.4, consists of two individual windings separated by 1". Each turn has an independent connection to the outside via an electrical feed-through. The coils are connected in series using copper connectors. Each turn is 6" long, 1" wide, and is located only 0.5" away from the atoms. We drive the coil using a digital synthesizer (SRS-DS345), followed by a 24 dB rf amplifier (MiniCircuits ZHL-3A) and a -2 dB attenuator to prevent damaging of the amplifier due to reflected power. During evaporation, the amplitude of the wave at the generator corresponds to +2 dBm. We have observed wide resonances of the coils between 25 and 13 MHz. These resonances are so strong that they affect some of the electronics close to the chamber; specially thermocouples. The problem is solved with various stages of rf filtering, and low-noise pre-amplification for thermocouple systems.

4.10.2 Gravitational sag

An effect to have in mind is the sag of the trap minimum due to gravity. For an atom in a harmonic trap with potential energy $1/2\, m\omega^2 x^2$, the addition of the term $-mgx$ shifts the potential by an amount

$$\Delta x = \frac{g}{\omega^2}, \tag{4.38}$$

where g is the acceleration due to gravity. This would not be a problem, except that rf evaporation relies on the fact that the most energetic atoms will be at the same distance from the minimum of the *magnetic field*, not

of the potential. If the sag is significant, the evaporation will start ejecting atoms which are not necessarily the hottest, and the cooling process will be extremely inefficient. The solution is to orient the coils of the IP trap in such a way that the long axis (Z) is horizontal, such that the strong radial confinement minimizes the potential minimum shift. The vertical cloverleaf arrangement automatically satisfies this condition. The trapping frequency during evaporation is $\omega = \omega_\rho = 2\pi\, 334$ Hz, which makes $\Delta x = 2.2\,\mu$m, much smaller than the thermal clouds undergoing evaporative cooling.

Chapter 5

Bose-Einstein condensation of sodium

In our experiment for quantum reflection we need ultracold atomic samples, and we produce them by evaporative cooling in a magnetic trap. For this experiment a Bose-Einstein Condensate (BEC) is not needed. In fact, having a high density cloud of atoms at the surfaces may have deleterious effects for quantum reflection, due to electric field gradients produced by the adsorbed atoms [103]. However, if forced rf evaporation works in the magnetic trap, it automatically leads to the attainment of BEC. We expected to produce a BEC and transport it close to the surfaces, where it would be decompressed to decrease its density and mean field effects. Afterwards it could be launched towards the surfaces. Although technical problems prevented us from doing this, and we currently transport non-condensed samples, we are still able to produce condensates routinely. In this chapter we describe how the condensate is formed, and a few interesting effects we have observed while working with it.

5.1 A brief introduction to Bose-Einstein condensation

In this section we give a brief introduction to Bose-Einstein condensation in dilute atomic gases. A proper treatment of the subject can be found in several excellent reviews, like the 2001 Nobel Lectures by E. Cornell, W. Ketterle, and C. Weiman [153, 154], or the *Reviews of Modern Physics* issues of April 1999

and April 2001 [155, 156].

The field of Bose-Einstein condensation is one of the most active areas of research today. Its origins trace back to the early days of quantum mechanics, when a clear distinction between statistics for fermions and bosons was established. After the photon statistics was introduced by S. N. Bose [157], A. Einstein worked on the hypotheses that an ideal gas of N bosonic particles confined in a volume V could have a finite fraction occupying the lowest energy state, that is, with momentum equal to zero [158, 159]. The condition for Bose condensation can be stated as [160]

$$\lambda_{\mathrm{dB}}^3 n > \zeta(3/2) = 2.612..., \tag{5.1}$$

where $\zeta(z)$ is the Riemann zeta function of z, and $n = N/V$ the density. The de Broglie wavelength is equal to

$$\lambda_{\mathrm{dB}} = \sqrt{\frac{2\pi\hbar^2}{Mk_{\mathrm{B}}T}}. \tag{5.2}$$

Thus, the condition can be interpreted as the thermal wavelength of individual atoms extending to the point of reaching interatomic distances. As the BEC is formed, it emerges as a macroscopic quantum object with coherent properties.

The case of superfluid helium is considered the first experimental manifestation of BEC observed. In the case of dilute gases, the first series of experiments aimed at the production of BEC were done using hydrogen ([144] and references therein), efforts which finally succeeded in 1998 [161]. However, the first observation of condensation in dilute gases was achieved by the JILA group in 1995 using rubidium [137], followed closely by the MIT group with a sodium BEC [135], and by the Rice group reaching quantum degeneracy using

lithium [162]. The number of BEC experiments today reaches close to 100, most of them using rubidium. It is our pride that we produced the fourth condensate in sodium, the other three obtained at MIT, Harvard and NIST [135, 163, 164].

5.2 Absorption Imaging

Before we show actual images of the condensate, and how it is formed, we begin by describing how the imaging of the samples is made. After we observed atoms in the magnetic trap for the first time, we started the optimization of loading and compressing the atomic cloud. Studies of lifetimes of the samples under different conditions in our vacuum system were also under way. All this was done by imaging the atomic fluorescence in optical molasses few milliseconds after releasing the atoms from the magnetic trap. While this worked well for hot atoms, it became difficult to have a good understanding of the rf evaporation process as the atom number decreased. At this point we abandoned fluorescence, and implemented an absorption imaging setup. In this method, a resonant probe beam is sent to the atoms, and the shadow cast by the cloud is imaged directly onto a CCD camera.

For a beam of intensity $I_0(x, y)$ incident on an atomic distribution of density $n(\mathbf{r})$, the intensity after absorption is:

$$I(x, y) = I_0(x, y) \exp(-\sigma \int n(\mathbf{r}) dz), \tag{5.3}$$

where $\sigma = \sigma_0(\Gamma/2)^2/(\Delta^2 + (\Gamma/2)^2)$ is the near resonance absorption cross section (we have neglected Doppler broadening). Because an integration along z is performed, from the absorption picture we cannot obtain the atomic density

directly. It is convenient to work with the optical density D:

$$D = -ln\left(\frac{I(x,y)}{I_0(x,y)}\right) = \sigma \int n(\mathbf{r})dz. \tag{5.4}$$

From this quantity properties relevant to the atomic cloud can be extracted. The atom number is obtained then after integration of D/σ along x and y. The temperature can be obtained by the time of flight method (Section 5.5.2), or by imaging the cloud inside the magnetic trap and relating size with temperature within the harmonic approximation. The latter technique can only be applied for small enough clouds, when the magnetic field does not shift the energy levels in a greater amount compared to the detuning used; alternatively, negligible time of flights could be used. For large clouds the analysis must take into account the full potential, beyond the harmonic approximation.

For absorption imaging, we use a beam which has the same detuning with respect to the ($F = 2 \longrightarrow F' = 3$) transition as the MOT light, that is $\Delta = -2\pi \times 20$ MHz. The beam is obtained by using the zero order from the AOM that produces the MOT light, which is passed through another AOM for intensity control. The polarization is linear, and the intensity used is maximum without saturating the CCD picture for exposure times of few hundred microseconds. The presence of repump light is necessary during imaging, because atoms are initially in the dark state ($F = 1$), and need to be pumped into the cycling transition. For a calculation of the atom number we use $\sigma_0 = 3f\lambda^2/2\pi$, where $f = 0.7$ is the oscillator strength for the cycling transition.

The probe beam is sent to the chamber making a 30° angle with the horizontal plane, and it images one radial and the axial directions. The repump

light is the same as the one used for the MOT, but with reduced intensity. After going through the imaging optics the beam reaches the camera, an Apogee AP7P peltier-air cooled CCD.

5.3 Computer control system

The experiment is run by using two computers, one controlling the timing of all devices and analog/digital outputs/inputs, and the other controlling the data acquisition. The software we use has been developed specifically for ultracold atom physics experiments by our postdoc Florian Schreck. As for the hardware, Florian and fellow graduate student Todd Meyrath have developed an inexpensive analog/digital output system. Florian has worked mainly on the neighbor rubidium BEC experiment with Todd, and they have built with great care and patience tools which the lab as a whole has benefitted from. We now describe each system schematically, detailed information can be found in reference [165].

Software. We use the program *Control*, written by Florian based on an earlier version he wrote while working on the lithium BEC experiment at the École Normale Supérieure [116]. It is written in Visual C++, and allows for very easy implementation of an experimental sequence with end commands of the type:

```
SwitchAbsorptionBeamShutter(On);
SetMOTLightAmplitude(MotMolLight);
SwitchAbsorptionBeam(Off);
```

All the programming of the digital and analog input/output boards is taken care of deep inside the guts of the code. However, it is easy to add new boards and devices. In our experiment, the program controls instruments using both serial and (TCP/IP) ports. All GPIB instruments are addressed using a National Instruments GPIB interface card. In Control, adding variables, the code of a sequence, a new digital or analog channel is no problem. It allows for series of measurements, randomization of parameters, etc., and is available at no charge [165].

For data acquisition we run Vision, another program developed by Florian. It is written in Borland C++, and has the capability to communicate with a host of CCD cameras. The front panel allows for automatic data fitting, zoom, and data manipulation. We are currently using Vision with two low noise CCD cameras, the 16-bit AP7P by Apogee, and an old 14-bit PI-ST135 by Princeton Instruments (Roper Scientific).

Control, responsible for timing of the experiment, communicates with Vision via (TCP/IP), sending not only the trigger commands, but all the current values of the variables in the experiment. Vision saves all these variables for every single experimental run, which facilitates tremendously a systematic search of 'random' or seemingly irreproducible effects.

Other software. In our old experiment we used the LabWindows/CVI environment to program our sequences, but now Control and Vision run the experiment entirely. However, we still use a few routines written within LabWindows, mainly to align our MOT daily in a reproducible way. The routines control a few digital and analog outputs necessary to create a MOT, and keep taking continuous frames with an 8-bit Pulnix CCD camera.

Hardware. In a regular BEC experiment a large number of digital and analog inputs and outputs are needed, and they are never enough. When we got our first BEC we had only an 8 channel 16-bit analog output board (NI-6533) and a 32 channel digital output board (PCI-DIO-32HS) from National Instruments (NI). As soon as we started the construction of the optical elevator we realized that we needed many more outputs than expected. The NI boards are very good, but expensive. An alternative was developed by Florian and Todd, using their electronics and computational expertise. They have designed a system that can house up to 256 analog (4096 digital) outputs, with an update rate of up to 500 kHz. According to their estimate, the cost per analog output (16-bit DAC's) is about $25, while for digital ouputs is $5. The system is based on a parallel bus which distributes data from the central computer to the boards, and is linked via a NI-6533 32-bit digital output board. We have now built a box containing 32 analog, and 40 digital outputs, with the capability of expanding this very easily. The boards have noise characteristics similar to those from National Instruments, with the advantage that they are cheaper, and integrated by design in the Control program. Another big advantage is the fact that all outputs are buffered, and can drive up to 0.25 A per channel, while for a NI board an additional buffer box has to be constructed.

5.4 A summary of the experimental sequence

In this section we give a summary of the experimental sequence followed to reach Bose-Einstein condensation. With the oven at 270 ^{o}C, the base pressures at the oven chamber, Zeeman Slower, and main chamber are: 8×10^{-9} Torr,

2.5×10^{-11} Torr, and 1.2×10^{-11} Torr, respectively. At $t = 0$ the Zeeman slower light is turned on, the oven shutter is opened, and the MOT is switched on. The MOT uses a 6 independent beam configuration, each beam with peak intensity of 10 mW/cm^2. A total of 70 mW of repump light is used (of which only 1/3 corresponds to the relevant sideband). The quadrupole MOT coils produce a gradient of 18 G/cm. After 4 s the MOT captures 2×10^9 atoms in a bright MOT. At this point the slower light is turned off and the oven shutter closed. The coils of the slower are left continuously on. To increase phase space density, the MOT is compressed in a CMOT stage during 7.5 ms by ramping up the fields and reducing the intensity of the repump light to 8% of its nominal value. After this, the magnetic field of the MOT is turned off, and a 2 ms period of polarization gradient cooling follows. This produces atomic samples with a peak density of about 8×10^{10} cm^{-3}, with an rms velocity of $\sigma = 8\, v_{\rm r}$ (= 24.0 cm/s, corresponding to 135 μK). Finally, the repump light is turned off and the MOT light stays for 500 μs longer, optically pumping the atoms into the dark state $F = 1$.

To transfer atoms into the magnetic trap, all resonant light is turned off, and there is a safety gap of 100 μs where the atoms are not confined. Then, the magnetic trap is switched on, with the power supplies in the constant voltage mode. The catching currents in the coils are listed in Table 5.1.

Switch-on times for the coils are 1 ms for the cloverleaves and bias, and about 5 ms for all other coils. To decrease the turn on time of the slow coils an extra voltage is applied to the power supply during the first millisecond of operation, and then put back to normal. This reduces the switch-on time down to 2 ms. During the transfer stage the bias field is $B_0 = 80$ G, and the

Coil	Current [A]	
	Transfer	Evaporation
Cloverleaf	320	485
Curvature	104	103
Anti-Bias	104	103
Trombone	10	103
Bias	0	3.6

Table 5.1: Currents in the magnetic trap coils during transfer and evaporation

trapping frequencies are $\omega_\rho = 2\pi$ 34 Hz, and $\omega_z = 2\pi$ 20 Hz. About 25% of the atoms form the MOT are captured in the magnetic trap.

After the transfer atoms are left for 300 ms to equilibrate, and then the cloud is compressed by ramping up the current in the cloverleaves while decreasing the value of the bias field. The change is linear during 1 s, to avoid introducing additional heating due to non adiabatic effects (Section 4.9). After compression the bias field is $B_0 = 2.3$ G, and the radial frequency is $\omega_\rho = 2\pi$ 338 Hz, while the axial frequency remains unchanged. Care is taken so that the unstable points (see Section 4.8.3) are far away from the limits of the cloud during the compression. Typical values for these distances are greater than 8 mm.

At the end of compression the atomic sample suffers an initial loss of about 30% of the atoms during the first five seconds. This may be due to incomplete optical pumping, and the residual spin relaxation of atoms in states other than the Zeeman sublevel with $m_F = -1$. After this initial loss the cloud has a lifetime of 45 s, which is enough for efficient rf evaporation. Before implementing evaporative cooling, we had estimated the value of the collision rate to be $\gamma = 5$ Hz. This value is an underestimation as we found evaporation to work really well. The evaporation lasts for 25 s, and has two

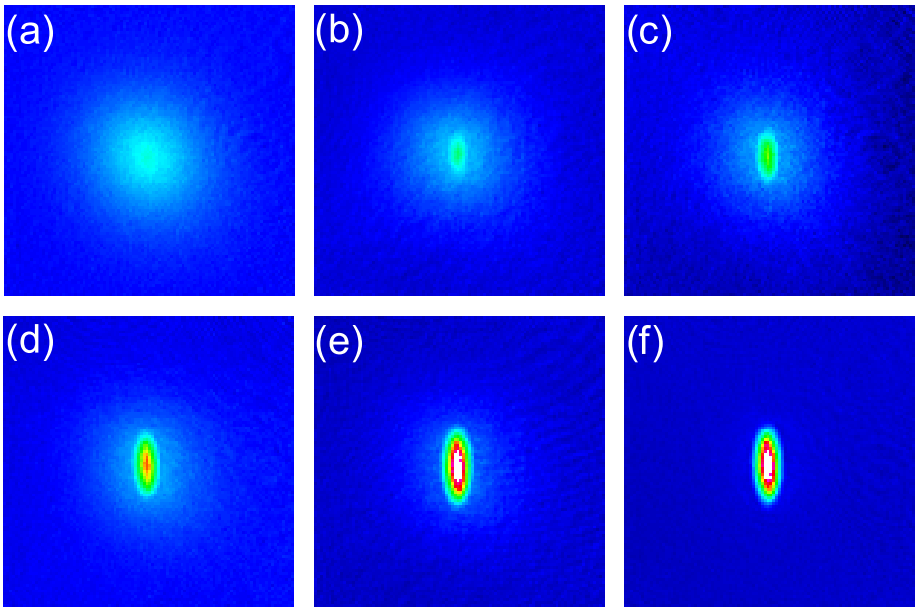

Figure 5.1: Absorption imaging pictures of the atomic density distribution show the formation of a Bose-Einstein condensate. The final rf frequency was changed across the point of critical temperature: (a) 1.89, (b) 1.88, (c) 1.87, (d) 1.85, (e) 1.80, and (f) 1.65 MHz. The pictures were taken 30 msec after the atoms were released from the magnetic trap. A pure BEC is shown in (f), containing 7×10^6 atoms. The field of view is 3.2×3.2 mm.

stages. During the first stage the rf frequency sweeps linearly from 30 MHz to 5 MHz over 20 s. The second stage is also a linear, with 5 s of duration that takes the frequency from 5 MHz down to 1.78 MHz.

Few days after we tried evaporation for the first time, we got really good pictures at the end of evaporation, with atoms very cold but not quite forming a BEC. After some investigation we found that the power in the repump during imaging was too high. Once its intensity was adjusted things

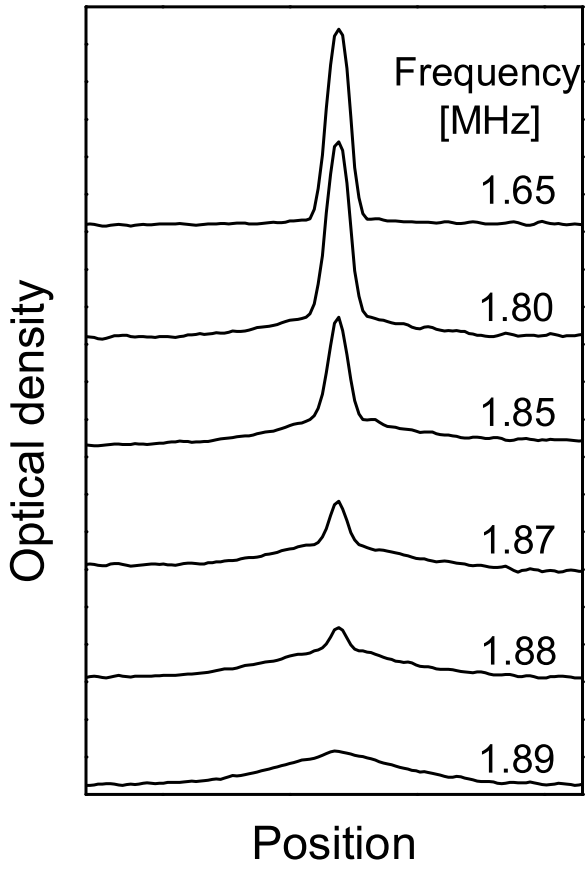

Figure 5.2: A horizontal cross section of the column density distributions of Fig. 5.1. The lineshapes show the characteristic bimodal distribution due to the emergence of a BEC. The values corresponds to the final frequency of evaporation.

were on track. A few minutes after midnight, on November the 14^{th} 2003 our first Bose-Einstein condensate was born. The signature was the well known emergence of a bimodal distribution in the atomic density distribution, after a few milliseconds of time of flight once the atoms were released from the magnetic trap, Figs. 5.1 and 5.2. The other signature was the dramatic asymmetric expansion of the cloud due to mean field repulsion in an almost pure BEC. The achievement of condensation was the end of a quest and the beginning of another one.

5.5 Characterization of the magnetic trap and BEC

Shortly before, and then after the achievement of BEC, we made a series of measurements to characterize the trap and the trapped cloud of atoms. Initially, all these numbers were important for an estimation of the collision rate. Later, they were used as a check for consistency among all the components. This section describes some of these measurements and its relevance for the experiment.

5.5.1 Frequency

The trap frequency in the radial direction was measured by observing the slosh of the atomic distribution center of mass inside the trap. The oscillations were induced by imposing a magnetic field pulse in the radial direction that displaced the atoms momentarily. The measurement was done with atoms having rms velocity of $\sigma_{\text{v}} = 1 v_{\text{r}}$, enough to be in the harmonic approximation at the bottom of the trap. In Fig. 5.3 we observe the result of the measurement, together with a sinusoidal fit.

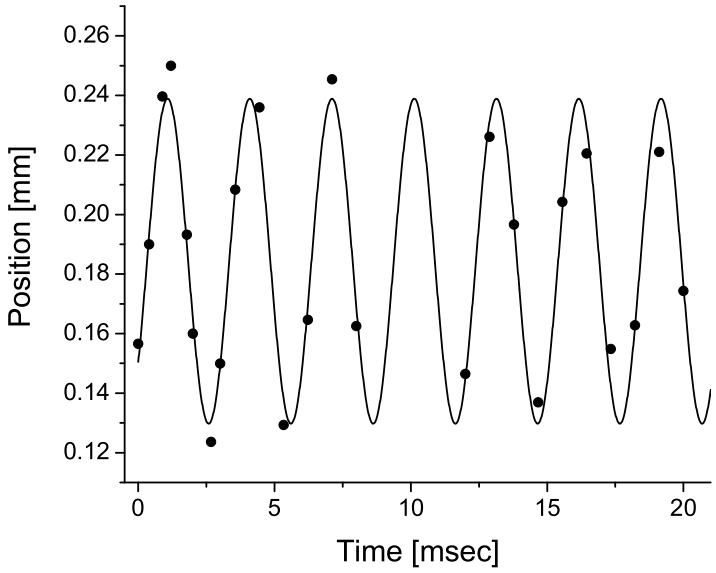

Figure 5.3: Measurement of the magnetic trap radial frequency. A small cloud of atoms is set to slosh inside the trap, and the center of mass motion recorded. The reported frequency is $\omega_\rho = 2\pi\, 331.5$ Hz.

The result of the sinusoidal fit is $\omega_\rho = 2\pi$ 331.5 Hz. This must be compared to the expected frequency based on the currents on the coils, and previous Hall probe measurements: $\omega_\rho = 2\pi$ 338 Hz. This gives us confidence in the validity of the magnetic trap field calculations, useful later when we transfer the atoms from the magnetic trap to optical potentials.

The measurement of the frequency can be refined, to measure for as many cycles as possible, gaining in sensitivity. Indeed, this sensitivity has been used to measure the transverse breathing mode of a condensate with a high quality factor [166]. More relevant to our experiment, the sloshing of the atomic distribution center of mass has been used to study the interaction of a condensate with atoms deposited on a surface [103].

5.5.2 The Bose distribution

In order to extract the temperature of a trapped gas we typically use the time of flight method (TOF). After the atoms have been released from the trap, they are left to expand ballistically, and a picture of the distribution is taken after a given time of flight. For atoms in a MOT, the atomic distribution can be fit very well by a spherically symmetric gaussian function. The initial density distribution is given by

$$n(\mathbf{r}) = \frac{N}{\sigma_0^3 (2\pi)^{3/2}} \exp\left(-\frac{\mathbf{r}^2}{2\sigma_0^2}\right), \tag{5.5}$$

where N is the total number of atoms. After a time of flight t, the density is given by a convolution of a gaussian in momentum space with a gaussian in position space. The result is

$$n(\mathbf{r}(t)) = \frac{N}{\sigma^3(t) (2\pi)^{3/2}} \exp\left(-\frac{\mathbf{r}^2}{2\sigma^2(t)}\right), \tag{5.6}$$

where $\sigma^2(t) = \sigma_0^2 + (\sigma_v t)^2$. The rms velocity of the distribution is σ_v, and can be found easily by the appropriate fittings.

This simple picture changes when dealing with atoms close to quantum degeneracy, where the statistics of the particles determine the density distribution. We now proceed to study the correct fitting function for time of flight pictures of atoms close to the BEC transition. Form this, a determination of the critical temperature will be given.

For a gas of bosons in thermal equilibrium, the mean occupation number in the single particle state of energy ϵ_i is:

$$f(\epsilon_i) = \frac{1}{z^{-1} e^{\beta \epsilon_i} - 1}, \tag{5.7}$$

where μ is the chemical potential, $z = e^{\beta\mu}$ is the *fugacity*, and $\beta = k_{\rm B}T$. Using a semiclassical approach, Bagnato and coworkers have shown that for particles of mass M under the influence of an external potential of the form $U(\mathbf{r}) = (1/2)M\sum_i \omega_i^2 r_i^2$, the density of particles is [167]:

$$n(\mathbf{r}) = \frac{1}{\lambda_{\rm dB}^3}\, g_{3/2}(z\exp(-\beta\frac{1}{2}M\sum_i \omega_i^2 r_i^2)). \tag{5.8}$$

The function $g_{3/2}$ belongs to the class of functions $g_n(z) \equiv \sum_{l=1}^{\infty} z^l/l^n$. In the experiment, we measure the integrated column density along one of the radial directions. Therefore, integrating the last expression along y, we obtain:

$$D(x,z) = \frac{\sqrt{\pi}\sigma_y}{\lambda_{\rm dB}^3}\, g_2(z\exp(-\beta\frac{1}{2}M(\omega_x^2 x^2 + \omega_z^2 z^2))). \tag{5.9}$$

The last equation is valid only for a gas inside the magnetic trap (or immediately released, $t = 0$). The integrated column density after a time of flight will be the convolution of the distribution at the trap and the free expansion of the particles. For times longer than any of the oscillation periods the result is:

$$D(x,z,t) = \frac{\sqrt{\pi}\sigma_y(t)}{\lambda_{\rm dB}^3}\, g_2\left(z\exp\left(-\beta\frac{M(x^2+z^2)}{2t^2}\right)\right). \tag{5.10}$$

In Fig. 5.4 we show the results of a fit using both Gauss and Bose distribution functions to the horizontal cross section of a typical time of flight absorption picture. The time of flight after release from the magnetic trap is 30 ms, and the temperature of the cloud is slightly below T_c. An emerging peak of condensed atoms can be seen. In order to neglect the contribution of the condensed atoms to the measurement of temperature, only those points at the wings are considered for the fit, Fig. 5.5. While the choice of the cutoff point is arbitrary, it is clearly in the region where both gaussian and Bose fits coincide.

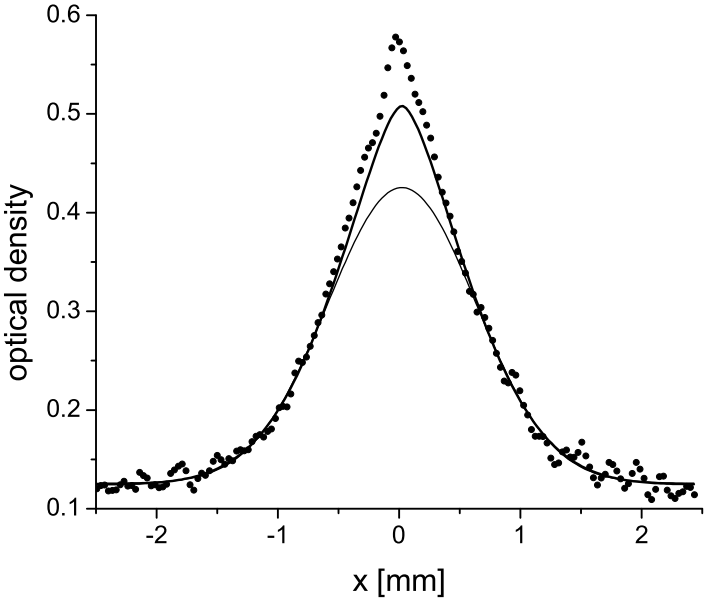

Figure 5.4: Fit to the horizontal cross section of a typical absorption imaging picture after time of flight. The temperature of the distribution is slightly below T_c, as a small fraction of condensed atoms is visible in the peak at the center. The Bose (thick line) distribution describes the data much better than a Gauss fit (thin line).

The gaussian fit gave for the distribution an rms velocity of $\sigma_{\rm v} = 2.04$ cm/s, which corresponds to a temperature of $T = M\sigma_{\rm v}^2/k_{\rm B} = 1.16\,\mu$K. The Bose fit gave slightly different results: $\sigma_{\rm v} = 2.19$ cm/s, so the temperature is $T = 1.32\,\mu$K. For comparison we calculate the critical temperature T_c. In an Ioffe-Pritchard trap, with mean trapping frequency $\bar{f}$, and N atoms, the critical temperature is [168]

$$T_c \simeq 4.5 \left(\frac{\bar{f}}{100\text{Hz}} \right) N^{1/3}\,\text{nK}. \tag{5.11}$$

For the particular data of Fig. 5.5, the number of atoms is $N = 1.2 \times 10^7$, and the mean trap frequency $\bar{f} = (331.5^2 \times 20)^{1/3}\,\text{Hz} = 130.0$ Hz. This gives

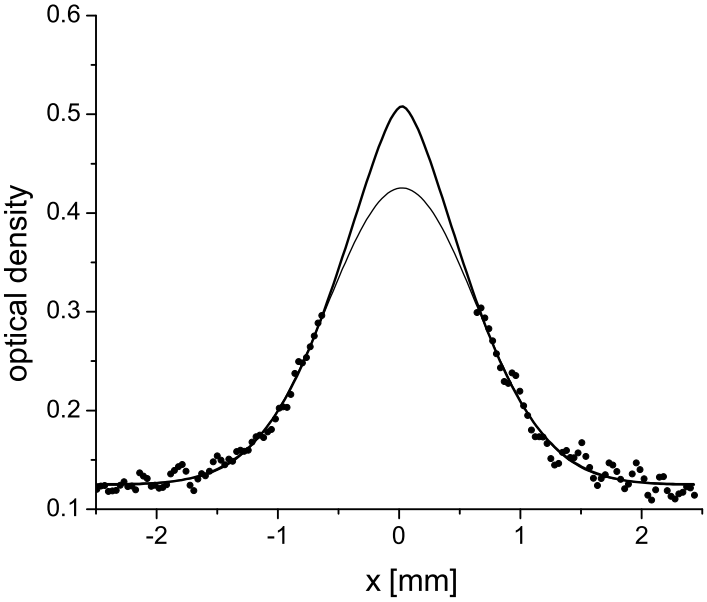

Figure 5.5: Bose (thick line) and Gauss (thin line) fits for the data of Fig. 5.4. Only the points taken to perform the fittings are shown.

$T_c = 1.34\,\mu$K. The result is remarkable close to what the Bose fit gives. The main uncertainty occurs in the determination of the number of atoms, but the dependence of the critical temperature on this parameter is weak (an error of 20% in the atom number gives an error in the estimation of T_c of only 6%).

5.5.3 The BEC distribution

As evaporation proceeds and the critical temperature is reached, the condensate peak starts to appear. During this stage the density distribution is composed by the BEC component and a thermal cloud with a Bose distribution. When the thermal component disappears, the pure BEC has a completely different behavior that can be dominated by mean field effects.

Many body effects in the density distribution can be taken into account

by considering the effect of the interactions due to pairs of particles. When summing over all particles, it is found that there is a net effect for the energy of the system. The result is the so called Gross-Pitaevskii equation, that describes the wavefunction of a dilute gas BEC [155]:

$$-\frac{\hbar^2}{2M}\nabla^2\psi(\mathbf{r}) + U(\mathbf{r})\psi(\mathbf{r}) + U_0|\psi(\mathbf{r})|^2\psi(\mathbf{r}) = \mu\psi(\mathbf{r}), \tag{5.12}$$

where μ is the chemical potential. The atomic interaction is given by $U_0 = 4\pi\hbar^2 a/m$, with a equal to the scattering length. For a pure BEC with a large number of atoms the kinetic energy term is small compared to the interaction term. In this case the kinetic term can be neglected, and the resulting equation is algebraic for the density. The procedure is known as the Thomas-Fermi approximation (TF). In this approximation, the solution for the density is remarkably simple:

$$n(\mathbf{r}) = |\psi(\mathbf{r})|^2 = (\mu - U(\mathbf{r}))/U_0. \tag{5.13}$$

In a harmonic trap, the resulting density profile is an inverted parabola that follows the shape of the trapping potential:

$$n(\mathbf{r}) = (\mu/U_0)(1 - \sum_i \frac{r_i^2}{R_i^2}), \tag{5.14}$$

where the typical size of the cloud is called the Thomas-Fermi radius:

$$R_i = \sqrt{\frac{2\mu}{M w_i^2}}. \tag{5.15}$$

In terms of the number of condensed atoms N_0, the chemical potential is [168],

$$\mu = \frac{1}{2}\hbar\bar{\omega}\left[15\frac{N_0 a}{(\hbar/M\bar{\omega})^{1/2}}\right]^{2/5}, \tag{5.16}$$

where $\bar{\omega}$ is the geometric mean of the trapping frequencies $\bar{\omega} = (\omega_x\omega_y\omega_z)^{1/3}$. The scattering length for sodium in the ($F = 1$, $m_F = -1$) state is $a = 2.75$ nm.

As mentioned before, in the experiment sometimes is more convenient to study the cloud after a time of flight. During free expansion the mean field energy is released in the form of kinetic energy, but the parabolic profile remains, only rescaled [169]. The size of the cloud changes as a function of time in the form:

$$\begin{aligned} R_{x,y}(\tau) &= R_{x,y}(0)\sqrt{1+\tau^2} \\ R_z(\tau) &= R_z(1+\lambda^2(\tau\arctan\tau - \ln\sqrt{1+\tau^2})), \end{aligned} \tag{5.17}$$

where $\tau = \omega_\rho t$, and $\lambda = \omega_z/\omega_\rho$. Integrating along y, we obtain the column density recorded on the CCD:

$$D(x,z,\tau) = \frac{2\mu R_y(\tau)}{U_0}\left(\frac{2}{3} - \frac{x^2}{R_x^2(\tau)} - \frac{z^2}{R_z^2(\tau)}\right). \tag{5.18}$$

5.5.4 Adiabatic decompression

When the atomic cloud reaches the BEC transition the density increases considerably inside the trap as the atoms fall into a single macroscopic quantum state. If the number of atoms is large the density is so high that three-body interactions occur, with subsequent heating of the sample. For the alkalis, the rate for three body recombination is on the order of 10^{-28} cm^3/sec. In practice, this limits the lifetime of the condensate to a few hundred milliseconds. Two alternatives can be followed to extend the lifetime of a trapped BEC. The first one is to keep the rf knife on to continuously eject the hottest atoms. That is known as 'rf shielding', and extends the lifetime of the BEC to the point where

is limited by the noise in the trapping potential and background collisions. Of course, the continuous evaporation keeps ejecting atoms. In our experiment, without rf shield the lifetime of the BEC is about 1 s. With rf shielding the $1/e$ decay time of the BEC is 15 s.

The second alternative to prevent heating is to decrease the density of the cloud by decreasing the trapping frequencies. In order to avoid heating, the process must be adiabatic. The decompression of the BEC reduces the mean field repulsion, avoiding expansion of the cloud upon release form the trap. In the case of a thermal cloud, the adiabatic decompression decreases the temperature even further. In the Thomas Fermi regime, the rms velocity of the adiabatically released BEC decreases as $\omega^{3/5}$ [164].

We implement adiabatic decompression by ramping down various currents in the trap, linearly over 500 ms. Final values for the currents are as follows: cloverleaves 350 A, anti-bias and curvature 94 A, bias 0 A, and trombone 5 A. The final trap frequencies are $\omega_\rho = 2\pi$ 40 Hz, and $\omega_z = 2\pi$ 19 Hz. After a condensate is decompressed it expands very little during ballistic expansion, making difficult to measure its momentum distribution. An estimate for the rms velocity along the radial and axial directions is $\sigma_{\rm v}^{\rho} = 2.5$ mm/s, and $\sigma_{\rm v}^{z} = 1.5$ mm/s, respectively.

After decompression, the geometric mean of the frequencies is $\bar{\omega} = 2\pi\, 31.2$ Hz, and the number of atoms in a pure condensate $N_0 = 1 \times 10^6$. Inserting these numbers into Eq. (5.16), yields the value $\mu/h = 645$ Hz for the chemical potential. This implies Thomas-Fermi radii equal to $R_{x,y} = 19\,\mu$m, and $R_z = 40\,\mu$m. During time of flight, the cloud changes size in the form given by Eq. (5.17). In the limit of long expansion times compared to the

frequency of oscillation: $R_{x,y}(t) \simeq R_{x,y}(0)\omega_{x,y}t$, which gives the equivalent of a 'velocity' of order $R_{x,y}(0)\omega_{x,y}$. For the parameters quoted, this value is equal to 4.8 mm/s, about a factor of 2 higher than our estimated rms velocity in the radial direction. Even in the decompressed trap mean field interactions dominate the dynamics of the condensate.

The decompression of the BEC is a necessary step for the loading of atoms into an optical lattice used for transport, a subject of study in next chapter. When we first implemented decompression, we tested whether the effect was adiabatic on the condensate by re-compressing the cloud and observing its expansion during time of flight after release from the magnetic trap. The re-compression was done by simply reversing the sequence used for decompression. The result was that decompression was indeed adiabatic, with the addition of a small heating of the cloud that changed the fraction of condensed atoms from nearly 100% to about 85%.

Similar procedures for decompression using sodium BEC's report rms velocity distributions of about $0.06\, v_{\rm r} = 1.8$ mm/s [164]. The combination of adiabatic decompression with small densities have produced sub-nanokelvin temperatures [170].

5.5.5 An interesting effect

While testing the decompression sequence we noticed that, when the atom number loaded in the magnetic trap was small, the final decompressed condensate contained a 'hole' in the middle. Typically, we produce nearly pure BEC's containing about 5×10^6 atoms. Upon decompression, such clouds are so dense that the absorption imaging signal is saturated and no inner struc-

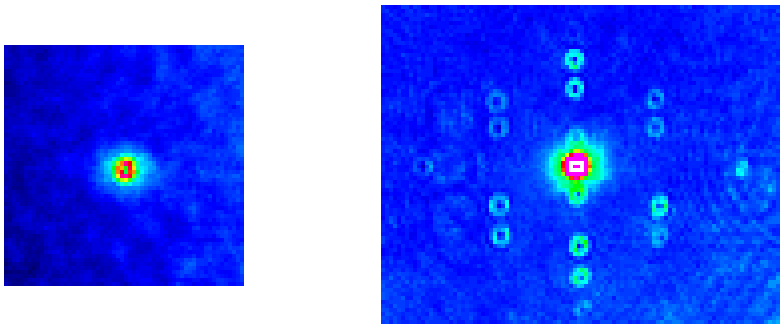

Figure 5.6: Topological effects in the decompressed BEC. (a) An atomic cloud containing about 10^6 atoms is shown after 25 ms in time of flight. The estimated BEC fraction is only 30%. (b) A nearly pure condensate was decompressed and subsequently illuminated with weak MOT light coming from six independent beams. The resulting distribution is shown after 28 ms in time of flight. While the origin of the donuts remains unknown, we believe the resulting array of atoms is due to superradiant Rayleigh scattering. Field of view is 1.92×1.92 mm and 3.20×2.56 mm for (a) and (b), respectively.

ture can be revealed even after 32 ms in time of flight. However, when the atom number in the final decompressed BEC is on the order of only 5×10^5 atoms, we observe the peculiar 'donut-shaped' cloud shown in Fig. 5.6(a). Initially, these rings were thought to be an artifact due to an optical effect or limited resolution of the absorption imaging setup. As we proceeded with the experiment however, we found these rings to appear consistently when the atom number was small *and* when the decompression sequence was run. We never observe these shapes when we do not decompress the cloud. Several tests have been performed to determine what is the origin of such clouds but it still remains a mystery.

Over the course of building our experiment we discovered accidentally another interesting effect that involves the decompressed BEC. During evapo-

ration and absorption imaging, the AOM that controls the MOT light intensity is disabled by using a rf switch. Because the switch does not extinguish the light completely, one mechanical shutter blocks residual MOT light coming from the AOM. It happened that one day this shutter did not work properly, and opened for a few milliseconds before the absorption picture was taken. As a result, the decompressed BEC was subject to leakage light coming from the six independent beams of the MOT for about 4 ms. The absorption imaging pictures revealed a beautiful symmetric array of ring-shaped BEC's, shown in Fig. 5.6(b).

After we found the cause of the effect, we implemented a sequence to induce it in a reproducible way. In order to do this, a pulse of MOT light illuminates the BEC after it has been decompressed. Then, a variable time of ballistic expansion follows and the absorption picture is taken. The duration of the light pulses are on the order of 10 μs, and the intensity of each MOT beam is about 0.6 mW/cm^2. We think that the resulting array after interaction with the MOT light is due to superradiant Rayleigh scattering, a phenomenon first observed in a Bose-Einstein condensate by the group of Ketterle [171]. In that experiment, an non-decompressed sodium BEC was illuminated with a pulse of light that was red-detuned by 1.7 MHz from the $3S_{1/2}(F = 1) \longrightarrow 3P_{3/2}(F' = 0, 1, 2)$ transition. It turns out we are using the same detuning; also, the parameters of the light pulses are similar in both experiments. However, the MIT group used light linearly polarized, and observed a strong dependence of the number of scattered atoms on the polarization direction relative to the long axis of the cigar-shaped condensate. Our case is different. First, we do not have linearly circularly polarized light,

but a superposition of three pairs of beams orthogonal to each other, each pair having two beams in the $\sigma^+ - \sigma^-$ configuration. Second, we have an almost spherical BEC. In fact, when we tried to induce scattering in a non-decompressed BEC we observed only small traces of scattered atoms, a signal by no means as clear compared to the case when the cloud is decompressed.

We have simplified the system by blocking one or more MOT beams at a time, and have observed a dependence of certain spots within the array on particular beams. We must mention the fact that our camera (which images one radial and the axial direction of the BEC) is located at an arbitrary angle respect to the MOT beams; therefore, it is most probable that the array occurs in three dimensions, and that each 'donut' is in reality a shell. There are multiple questions to be investigated, regarding the process of scattering under the mentioned conditions. Most intriguing is the fact that the donut-shaped BEC's created, we believe, during decompression, replicate themselves as atoms undergo scattering. These are open questions that we plan to study.

Chapter 6

An optical elevator for ultracold atoms

6.1 Introduction

The success of implemented runaway evaporation in a magnetic trap, and subsequent observation of Bose-Einstein condensation, provided us with cold enough atomic samples to begin its transport towards the surfaces. Atomic motion for distances over 10 cm is realized using an optical lattice. In contrast to our previous work on quantum transport, here tunneling effects are negligible. We employ a moving lattice to carry atoms over macroscopic distances, from one place to another inside the vacuum chamber. It is important to note that this method of atomic transportation is very general and can be used for a variety of purposes

In this chapter we revisit the origin and characteristics of the optical potentials in the very far from resonance limit, and the details of its use for the transport of sub-recoil atoms. Finally, the current status of the Casimir-Polder experiment is reported.

6.2 The dipole force revisited

We have previously reviewed relevant issues concerning two type of interactions between light and matter: in the regime where spontaneous processes dominate the dynamics, and when light is far detuned from resonance, mak-

ing spontaneous scattering negligible. We now come back to the study of the dipole force. An important difference with respect to the regime used before is that the light used to create the optical potentials of this section is very far from resonance. While the experiments for quantum transport used detunings on the order of $\Delta_{\rm L} = 2\pi\, 100$ GHz, we now use lasers whose wavelength is detuned from resonance by as much as to 475 nm, that is $\Delta_{\rm L} \simeq 2\pi\, 10^5$ GHz. In the case of the alkalis, this implies involvement of both D lines in the creation of the potential.

The net effect on an atom under the presence of far off resonance light is a shift of the atomic energy levels, due to the interaction between the electric field of the light and an induced electric dipole (Section 1.1.1). This effect is known as the AC Stark shift, for its resemblance to the static case. For an AC field the energy shift is proportional to the square of the electric field:

$$\Delta W = -\frac{1}{2}\alpha E^2, \tag{6.1}$$

where the proportionality constant $\alpha(\nu)$ is the electric dipole dynamic polarizability, Eq. (3.19). The factor of 1/2 accounts for the fact that the electric dipole moment $\alpha(\nu)E$ is induced. For frequencies corresponding to energies smaller than the first allowed dipole transition at energy E_0, an approximate expression is obtained in terms of the static polarizability, Eq. (3.10) [172]:

$$\alpha(\nu) = \frac{\alpha E_0^2}{E_0^2 - (h\nu)^2}. \tag{6.2}$$

As mentioned before, the static polarizability α has the value 24.08×10^{-24} cm^3 for sodium in the ground state.

An atom with main dipole transition at frequency ω_0 illuminated by a

beam of intensity $I(\mathbf{r})$ and frequency ω, experiences the potential [173]:

$$U(\mathbf{r}) = -\frac{3\pi c^2}{2\omega_0^3}\left(\frac{\Gamma}{\omega_0-\omega}+\frac{\Gamma}{\omega_0+\omega}\right)I(\mathbf{r}), \tag{6.3}$$

where Γ is the natural linewidth of the atomic transition. This formula takes into account both D lines of the alkalis, and assumes that the light is so far detuned respect to any of these transitions that the effective detuning is the same. The second term of Eq. (6.3) can be neglected in the rotating wave approximation [173]. With the following definition for the detuning: $\Delta_{\mathrm{L}} = \omega - \omega_0$, the potential becomes:

$$U(\mathbf{r}) = \frac{3\pi c^2}{2\omega_0^3}\frac{\Gamma}{\Delta_{\mathrm{L}}}I(\mathbf{r}). \tag{6.4}$$

It is important to note that the scattering rate in this regime is equal to:

$$\Gamma_{\mathrm{sc}}(\mathbf{r}) = \frac{3\pi c^2}{2\hbar\omega_0^3}\left(\frac{\Gamma}{\Delta_{\mathrm{L}}}\right)^2 I(\mathbf{r}). \tag{6.5}$$

The above formulas do not consider the effect of multiple level atoms. In the case of alkalis, a general formula for the dipole potential experienced by a particular hyperfine state m_F is given by [174]:

$$U(\mathbf{r}) = \frac{\hbar\Gamma}{24 I_{\mathrm{S}}}\left[\left(\frac{1}{\Delta_{1/2}}+\frac{2}{\Delta_{3/2}}\right) - g_F m_F\sqrt{1-\epsilon^2}\left(\frac{1}{\Delta_{1/2}}-\frac{2}{\Delta_{3/2}}\right)\right]I(\mathbf{r}), \tag{6.6}$$

where the ϵ is the ellipticity in the polarization of the light $\hat{\varepsilon} = 1/\sqrt{2}(\hat{x}\sqrt{1+\epsilon}+ i\hat{y}\sqrt{1-\epsilon})$. The detunings respect to the D1 and the D2 transitions in units of Γ are $\Delta_{1/2}$, and $\Delta_{3/2}$, respectively. The saturation intensity is $I_{\mathrm{S}} = 2\pi^2\hbar c\Gamma/(3\lambda_0^3)$, equal to $6.26\,\mathrm{mW/cm^2}$ in the case of sodium.

6.3 Optical potentials: A single focused beam

The simplest form of dipole trap is created with a red detuned, single, gaussian focused beam. Assuming linear polarization and wavelength λ, the potential

is given by:

$$U(\mathbf{r}) = U_0 e^{-2(x^2+y^2)/w^2(z)} \left(1 + (z/z_{\rm R})^2\right)^{-1}, \tag{6.7}$$

where $w(z) = w_0\sqrt{1+(z/z_{\rm R})^2}$, and $z_{\rm R} = \pi w_0^2/\lambda$ is the Rayleigh length. The potential maximum, from Eq. (6.4) is

$$U_0 = \frac{3\pi c^2}{2\omega_0^3}\frac{\Gamma}{\Delta_{\rm L}}\frac{2P}{\pi w_0^2}, \tag{6.8}$$

where we have set the peak intensity in terms of the incident power P: $I_0 = 2P/(\pi w_0^2)$. In a red detuned trap ($\Delta_{\rm L} < 0$) atoms can be trapped at the center of the focused beam. The oscillation frequencies of such a trap are found by expanding the potential around the minimum, keeping terms within the harmonic approximation. The resulting frequencies in terms of the total incident power and the waist are:

$$\omega_{\rm rad} = \sqrt{\frac{4|U_0|}{Mw_0^2}}, \tag{6.9}$$

$$\omega_{\rm ax} = \sqrt{\frac{z|U_0|}{Mz_R^2}} = \frac{\lambda}{\sqrt{2}\pi w_0} w_{\rm rad}, \tag{6.10}$$

where M is the atomic mass. One or more of such focused beams can be used to trap atoms and change the strength of confinement.

In the case of blue detunings ($\Delta_{\rm L} > 0$), very tightly focused beams can be used to trap atoms in a minimum of the intensity. Such arrangements can be used for various effects, including holding atoms against gravity [175], and studying chaotic dynamics [176]. In our experiment we use both type of detunings.

6.4 Optical potentials: A moving lattice

The potential created by two counter-propagating beams was reviewed extensively at the beginning of this dissertation. We now consider the case of a single beam retro-reflected on itself, configuration that will lead us to the optical elevator. We write the formula for the potential, following Eq. (1.10):

$$U(z,t) = \hat{U}_0 \cos^2(k_{\rm L} z - \phi(t)), \tag{6.11}$$

where we have allowed for the possibility of a moving lattice due to motion in the retro-reflecting mirror. As before, we have neglected beam divergence, and assumed that the typical size of the atomic cloud is much less than the beam waist w_0. The well depth is four times as large compared to the single beam depth[1]: $\hat{U}_0 = 4|U_0|$. With the potential written in the form of Eq. (6.11), we identify $\hat{U}_0$ as the well depth, as opposed to the amplitude V_0 used in Chapter 1.

One important quantity is the oscillation frequency characteristic of the trap. This can be found by approximating the potential at the minima by a harmonic potential. The result is

$$\omega_{\rm lat} = \sqrt{\frac{2\hat{U}_0}{M}} k_{\rm L}, \tag{6.12}$$

for a stationary lattice. For atoms trapped in a vertical lattice, another quantity of interest is the ratio of the optical gradient force to the gravitational pull. Because we want to hold the atoms and then transport them vertically

[1]It is important to stress the fact that, for a given set of variables of the beam, the lattice well depth in this Chapter is a factor of 3/2 larger than the one presented in Chapter 1, Eq. (1.18). The reason being, as stated before, that we now take into account both D lines in the calculation of the AC Stark shift.

(see Fig. 6.1), we have to make sure that this ratio is large. In an optical lattice this is not difficult to obtain, but it can become critical in the case of a sheet of light. For a lattice the ratio is on the order of

$$\eta = \frac{2\hat{U}_0}{mg\lambda}. \tag{6.13}$$

In the retro-reflecting configuration for an optical standing wave, the reflecting mirror determines the dynamics of the potential. The phase of the reflected beam relative to the incoming one ($\phi(t)$) is given entirely by the longitudinal displacement $\Delta z(t)$ of the mirror relative to some initial value. In terms of the displacement, the potential of Eq. (6.11) can be written as

$$U(z,t) = \hat{U}_0 \cos^2[k_{\mathrm{L}}(z - \Delta z(t))]. \tag{6.14}$$

We would like to trap atoms in a lattice and transport them vertically for distances of several centimeters. A piezoelectric transducer can be used to displace the mirror, but its dynamic range is extremely small. Another option to have a moving lattice is to abandon the retro-reflecting configuration altogether, and come back to the use of independent beams controlled by AOM's (as in the experiments of Chapter 1). This of course can be done, at the expense of losing optical power due to limited diffraction efficiencies of the AOM's. Our solution was to keep the retro-reflecting arrangement, and move the mirror using a motorized linear translation stage.

6.5 The atomic elevator and its experimental implementation

The optical elevator consists of trapped atoms in a vertical optical lattice which are moved upwards. If the lattice beams are red detuned and tightly focused,

the atoms not only will be confined longitudinally by the optical gradients due to interference, but also transversely because of the attractive nature of the dipole force. Indeed, using such configuration, single atoms have been trapped and moved over distances of 10 mm, with efficiencies of 80% [177]. In that case the orientation of the lattice was horizontal, reason for which the setup was termed 'an optical conveyor belt' for single atoms.

In our case, when deciding over which laser to use for our elevator, we had to take into account that we wanted to transport vertically, not horizontally, and not one but a few million atoms, over distances of 15 cm. The requirements are much different as those from the cited reference. Given a certain number, density, and temperature of the atomic cloud produced by evaporation in the magnetic trap, the lattice beams have to be much larger in spot size than the cloud diameter. A second requirement is that the well depth must be much larger than the typical atomic temperature. Also, the required moving distances prevent tight focusing, unless a combined method of a moving lattice plus a moving lens is used. Finally, we had in our lab available lasers at $\lambda_{\mathrm{L}} = 532$ nm, and $\lambda_{\mathrm{L}} = 1064$ nm. The static polarizability given in Eq. (6.2), implies a resonance enhancement factor of

$$\frac{\lambda_{532}}{\lambda_{1064}} \frac{\lambda_{1064} - \lambda_0}{\lambda_0 - \lambda_{532}} \simeq 4, \tag{6.15}$$

gained for the well depth when using $\lambda_{\mathrm{L}} = 532$ nm (blue detuned) as opposed to $\lambda_{\mathrm{L}} = 1064$ nm (red detuned), for the case of sodium ($\lambda_0 = 589$ nm).

The factors listed above lead us to choose 532 nm light for our optical lattice. One more advantage of using blue detuned light is that atoms concentrate in regions void of light, which helps reducing the spontaneous emission

rate. A clear disadvantage is that there is no transversal confinement. To prevent this, our elevator uses a red detuned beam that co-propagates with the lattice.

6.5.1 A 'stationary' lattice

The optical lattice is formed by a single, retro-reflected beam than enters the chamber form the lowest viewport of the main vacuum chamber (see Fig. 4.7). The light is derived form a 10 W Verdi laser (Coherent), located 10 m away from the BEC chamber[2]. Typical power used is in the lattice is 2.3 W, controlled by an AOM. The beam is spatially filtered, and has a beam waist of $w_0 = 500\,\mu$m, measured about 65 cm away from the atoms. The well depth is $\hat{U}_0/h = 83$ kHz, and the oscillation frequency $\omega_{\rm lat} = 2\pi$ 101 kHz. Gravitational sag is negligible, as the optical gradient generated by the lattice corresponds to about 700 times the gravitational force.

For the red detuned trap, we use a 10 W Nd:Yag fiber laser (IPG Photonics, #YLD-10). The intensity is controlled by an AOM; a typical power of 6 W is used. The beam has a waist at the magnetic trap center of $w =$

[2]Having the interaction laser so far away poses a serious challenge, and a lot of care had to be taken to minimize pointing instability, thermal drifts, and diffraction of the gaussian beam. The reason for the laser being so far from us is that it is shared with another BEC experiment. Our colleagues in the rubidium experiment need all 10 W to create the optical potentials necessary for the manipulation of their BEC. In our case, we also need all the power available from the laser to increase the well depths of the potentials that will transport the atoms towards the surfaces and beyond. The implemented solution is to have a half-waveplate in front of the laser before the beam reaches a polarization cube beam splitter (PBS). The waveplate is mounted on a linear motorized translation stage, and is computer controlled. One of the two experiments is in charge of the waveplate; when needed it is moved such that all the power goes to that experiment. At the end of the particular run the waveplate is set back to its original position, so all the power goes to the other experiment. A typical experimental run uses the Verdi light for 5 s after 25 s of evaporation. Then, on the average 1 out of 6 shots will be lost because of this reason. In practice, because of other reasons, we lose about 1 shot in 10.

350 μm, and it converges close to the surfaces, where it reaches $w = 275\,\mu$m. The corresponding well depth at the start of transport is $U_0/h = 27$ kHz, and the oscillation frequency $\omega_{\rm rad} = 2\pi$ 20 Hz. The beam co-propagates with the lattice beam by means of a dichroic mirror placed above the glass cell, Fig. 6.1.

With a beam waist of $w_0 = 500\,\mu$m, the Rayleigh length for the lattice beam is 1.5 m. Therefore, the beam spot size remains constant through the interaction region, from the center of the magnetic trap to the location of the surfaces, or about 11 cm. However, the divergence of the beam is significant for distances over 0.5 m. Because of space constraints, the closest position of the retro-reflecting mirror respect to the atoms is 50 cm. Then, a simple mirror cannot be used for reflection, as the return beam will not match the mode of the incoming beam, creating transversal fringes which the atoms can use to escape.

The implemented solution to the problem of mode-matching consists in expanding and collimating the beam as it exits the chamber, before reaching the retro-reflecting mirror (see Fig. 6.1). A telescope magnifies the beam by a factor of 5, which decreases the divergence by a factor of 25. One of the telescope lenses is placed on a translation stage. With proper adjustment, the retro-reflected beam matches the incoming wavefront to a very high degree. We verify this by observing the contrast of interference fringes on a Michelson interferometer, shown in Fig. 6.1. The actual position of the interferometer is 2 m away from the atoms, and about 3 m away from the retro-reflecting mirror.

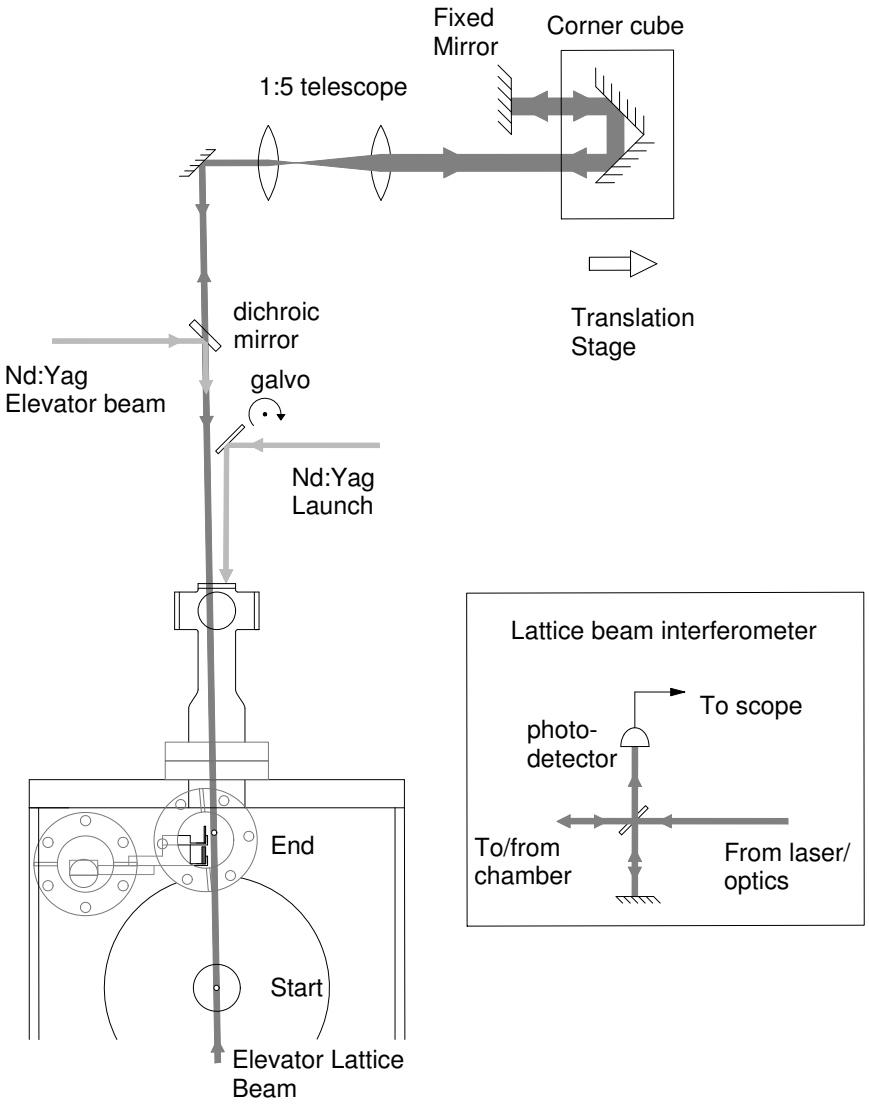

Figure 6.1: A schematic of the setup used for the optical elevator. The lattice beam enters the chamber going up, passes the dichroic mirror and is expanded to minimize divergence. A corner cube mirror is used to minimize lateral displacement during elevation. The cube is mounted on a translation stage. Lateral confinement is provided by a co-propagating Nd:Yag beam, coupled in the dichroic mirror. Atoms start at the center of the magnetic trap and end in front of the surfaces. The interferometer output monitors the fringe visibility.

6.5.2 Loading

The procedure for loading atoms in the stationary lattice is as follows. Atoms are evaporatively cooled for 25 s in the magnetic trap, after which time the rf is switched off, and the atomic cloud decompressed as described in Section 5.5.4. The purpose of the decompression is twofold: in the case of condensed atoms it decreases mean field repulsion, and reduces the density to avoid three-body collisions. In the case of thermal clouds, adiabatic decompression effectively lowers the temperature. Thermal clouds after decompression have typical rms velocities of $\sigma_{\rm v} = 2$ mm/s.

After decompression, the values of the currents in the magnetic trap coils are kept constant for transfer. The red detuned trap is introduced first, and its power ramped from zero to maximum during 30 ms. Then it is left on for about 200 ms. The idea is to introduce a dimple in the combined magnetic trap plus dipole potential that collects atoms around the region of the elevator. Finally, the lattice beam is turned on by ramping its power linearly from zero up to 2.3 W in 30 ms. The combined potential remains for 100 ms more before the magnetic trap is suddenly switched off. At this point the atoms are in the pure optical trap.

After loading a decompressed BEC from the magnetic trap into the elevator, we found it becomes a thermal cloud after a few hundred milliseconds, due to heating. The measured heating rate in the pure optical trap is about 100 nK/s. Therefore, instead of using a BEC, we transfer thermal clouds in order to increase the total atom number. We load 2.5×10^6 atoms in the elevator (limited by the capture volume), resulting in an almost spherical cloud with an rms size of $\sigma_{\rm x} = 85\,\mu$m. Lifetime in the trap is 10 s, limited mainly

by mechanical fluctuations in the retro-reflecting mirror. After 1 s of holding time in the lattice, the the atomic distribution has a geometric average of the rms velocity equal to 12.8 mm/s $= 0.43\, v_{\rm r}$.

A pure BEC loaded into a lattice is expected to show an accelerated free expansion of the cloud in the horizontal direction due to an increase of mean field repulsion. This has been observed before with a rubidium BEC [178]. We did not study this behavior.

6.5.3 Bloch oscillations in the vertical lattice

A vertical lattice where the phase of the two component beams is the same does not result in a truly stationary potential, but one being accelerated at $g = 9.81$ m/s^2. In the lab frame we are under the influence of the same acceleration, and that is why we can write directly Eq. (1.34) as the effective Hamiltonian describing the atomic motion:

$$H = \frac{p^2}{2M} + U_0 \cos^2(k_{\rm L} z) + M g\, z, \tag{6.16}$$

which gives rise to the coherent phenomena described in Chapter 1.

In our system we observed Bloch oscillations with a pure condensate inside the vertical lattice, without the transverse confinement of the Nd:Yag beam. A BEC was decompressed and loaded into the lattice as just described, and atoms were held inside the potential for a variable time, before turning the lattice beam off in less than 1 μs. The time of flight pictures revealed the coherent evolution of the atomic wave-packet, Fig. 6.2.

We have already mentioned in Section 1.2.3 that during Bloch oscillations both velocity and position of the atomic distribution center of mass

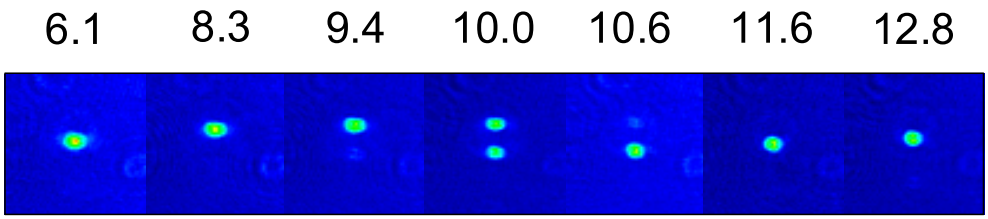

Figure 6.2: Bloch oscillations in a vertical standing wave. A decompressed BEC was loaded into the lattice for a variable amount of time and suddenly released. Pictures are shown after 10 ms in time of flight, and numbers on top correspond to the time in the lattice, in milliseconds. The period of the oscillations is 6.65 ms. The field of view for each frame is 1.92×1.92 mm.

follow an oscillatory motion inside the lattice, with a period τ_{B} given by Eq. (1.39). When the lattice is turned off, the atoms follow ballistic trajectories during time of flight, therefore translating their values of velocity at switch-off into position space. As atoms move in reciprocal space due to acceleration, they reach points where the velocity of the center of mass is zero. These points occur for values of the quasi-momentum k_0 where the condition

$$v(k_0) = \frac{1}{\hbar}\frac{\partial E(k)}{\partial k}\bigg|_{k=k_0} = 0,$$

is satisfied. In Fig. 6.2 we observe that these points correspond to lattice holding times equal to 6.1, 10.0 and 12.8 ms. In particular, the distribution resulting after $t = 10.0$ ms inside the lattice reflects the fact that atoms have reached the edge of the first Brillouin zone (where the quasi-momentum is equal to $k_0 = +k_{\mathrm{L}}$), and discontinued their motion at that point to reappear at the opposite edge of the zone, with quasi-momentum $k_0 = -k_{\mathrm{L}}$, (see also Fig. 1.2). A thorough description regarding the observation of Bloch oscillations by cold atoms in an accelerating lattice can be found in references [12, 17, 179].

The Bloch period for atoms inside the elevator lattice is equal to

$$\tau_{\mathrm{B}} = \frac{2v_{\mathrm{r}}}{g}\frac{\lambda_0}{\lambda_{\mathrm{L}}} = 6.65\,\mathrm{ms}, \tag{6.17}$$

which is what we measure. The effect constitutes a beautiful demonstration of the subject presented in Section 1.2.3.

During the first days of alignment of the lattice we worked with low well depths, due to misalignment and poor quality of the verdi beam, which lead to substantial tunneling. In an accelerated lattice, each time atoms reach the edge of the Brillouin zone during Bloch oscillations they will tunnel from the first to the second band, and successively into the continuum. As a result, atoms leave the potential as a train of pulses, separated in time by the Bloch period (Fig. 6.3). One of the first (pulsed) atom lasers was created using this method [180].

We also imaged the collision of two coherent matter waves (Fig. 6.4), created when the BEC reached the edge of the Brilluoin zone during Bloch oscillations. At this point the wavepacket splits into two distributions with momenta $p = \pm\hbar k_{\mathrm{L}}$. A similar example of elastic collision with matter waves was observed at the MIT group, when Bragg diffracted atoms collided with the original condensate [141].

We note that in our system we do not observe Bragg diffraction [164], because the lattice is turned on adiabatically. This loads the atomic wavepacket into the ground state of the potential, namely, a Bloch state. The state has a well defined quasi momentum, located within the first energy band.

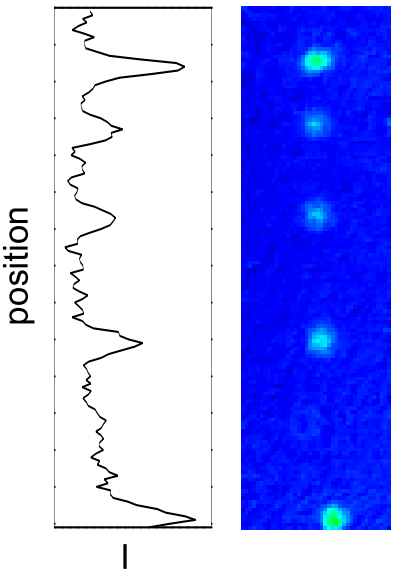

Figure 6.3: A pulsed atom laser resulting from tunneling during Bloch oscillations in a weak vertical optical lattice. When atoms reach the edge of the Brillouin zone they tunnel to higher energy bands, and are quickly lost from the potential. A decompressed BEC was held for 25 ms inside the lattice. A picture is shown after 10 ms in time of flight. The field of view is 1.28×4.48 mm. To the left it is shown the integrated optical density along the horizontal direction (I).

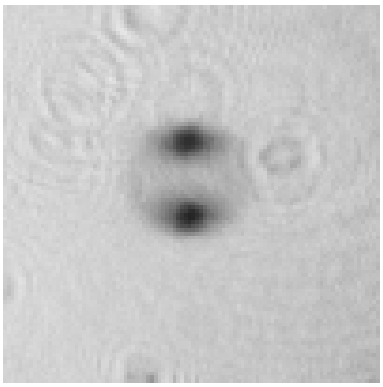

Figure 6.4: The elastic collision of two coherent atomic matter waves. The distributions have momentum $p = \pm\hbar k_{\mathrm{L}}$, and were obtained by interrupting Bloch oscillations at the edge of the Brillouin zone. The picture presents results of the collision after 17 ms in time of flight. Field of view is 3.2×3.2 mm

6.5.4 The moving lattice

After the observation of tunneling during Bloch oscillations, we fixed several problems in our optical setup, and the quoted lifetimes of 10 s were obtained in the full optical trap. In order to move the atoms upwards, we first used the retro-reflecting mirror mounted directly on a linear translation stage (Velmex Unislide #MA1515K2S1.5), driven by a stepper motor. The slide consists of an aluminum dovetail driven by a lead screw attached to the motor. Due to the inherent nature of stepper motors, a lot of vibrations are produced during operation. We tried to damp all possible noise by using several layers of sorbothane between the stage and the optical table, and between the reflecting mirror and the stage as well. We observed atoms transported over distances of a few millimiters only, before losing all the atoms.

To remedy the poor efficiencies of the elevator, two improvements were implemented. First, we noticed that the fringe visibility on the monitoring interferometer decreased considerably as the mirror on the translation stage moved. This was due to slight changes in the angle between the mirror and the lattice beam, which caused a poor overlap when transport took place. The solution was to remove the mirror from the slide and replace it by a corner cube mirror, as shown schematically in Fig. 6.1. As the lattice beam enters the cube, it bounces off the three faces, and exits parallel to the incoming beam. Right after the cube, fixed onto the optical table, we placed the retro-reflecting mirror. We verify that during displacement of the stage the fringe visibility remains constant.

The corner cube mounted on the translation stage not only ensures proper alignment of the lattice during transport, but decreases the total travel

time and distance by half. The reason is the double path followed by the beam as it reflects first off the cube and then from the retro-reflector, as opposed to using the retro-reflector exclusively. It may be possible that by adding a number of similar stages of reflection, the total travel distance of the slide could be decreased even more.

A second problem involved residual noise caused by the stepper motor driving the slide. We replaced it by a brushless DC motor (Galil, #BLM-N23-50-1000), controlled by a servo driver (Galil, DMC-1416-brushless). The motor is fitted with hall sensors and has a 1000 points-per-revolution encoder. After optimization, we found that the best transfer efficiencies were obtained when both velocity and acceleration were maximum without exerting excessive torque on the motor. For transporting atoms over a distance of 10 cm (i.e. 5 cm of slide translation), we use a trapezoidal waveform for the velocity. The magnitude of initial and final accelerations is 1000 mm/s^2, and the final travel velocity is 160 mm/s. A diagram of the timing for atomic motion in the lattice during transport is found in Fig. 6.5.

During motion, we monitor the actual velocity of the atomic cloud in the optical lattice. This is done by simply counting the rate at which fringes appear in the interferometer signal. From this signal not only the velocity but also acceleration and position can be determined. In principle, with a proper feedback using the fringe signal it should be possible to achieve a precision during transport of $\lambda_L/2$. In our application this is not necessary because the atomic cloud itself is about 150 μm in diameter.

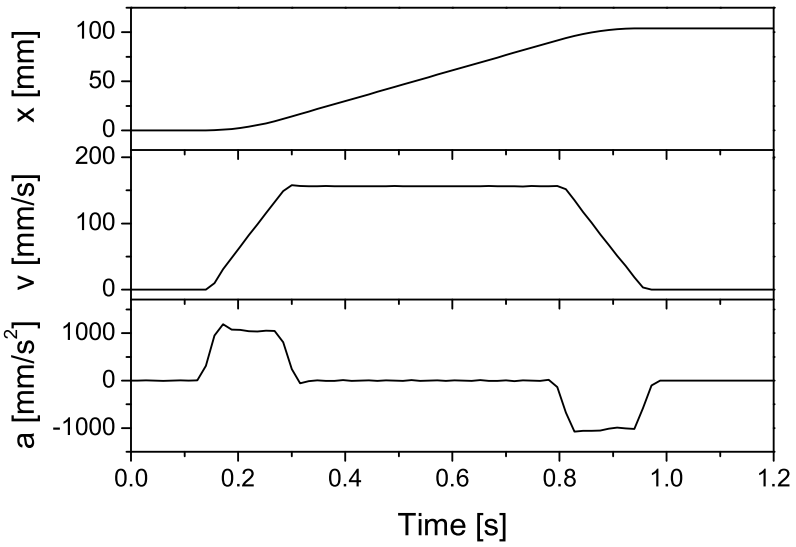

Figure 6.5: Timing of atomic motion inside the optical elevator as the motorized slide moves. The above traces were obtained from a monitor signal provided by the motor servo driver, and are identical to the ones obtained by analyzing the fringes from the Michelson interferometer signal. The labels correspond to position (x), velocity (v), and acceleration (a).

6.5.5 Results

Using the setup just described, we move routinely 1.5×10^6 atoms over a distance of 10.5 cm (Fig. 6.6). The time for transport is under 1 s, and the efficiency is 60%. We define efficiency as the number of atoms transported over the number initially loaded into the elevator. The density, however decreases during transport almost by a factor of 10, mainly due to a small divergence and misalignment of the red detuned beam respect to the optical lattice.

The velocity spread of the atomic distribution changes from $\bar{\sigma}_{\rm v} = 12.8$ mm/s at the beginning of elevation, to $\bar{\sigma}_{\rm v} = 18.0$ mm/s at the end of the sequence. We should note that this value corresponds to the geometric mean of the rms velocities. After 1 s of transport time in the lattice, we measure $\sigma_{\rm v}^{\rm T} = 12$ mm/s and $\sigma_{\rm v}^{\rm L} = 27$ mm/s along the transverse and longitudinal

directions, respectively. We believe this asymmetry in the temperature is due to Bloch oscillations inside the lattice, as the center of mass of the atomic distribution is constantly undergoing change in momentum. Atoms transfer some of their potential energy due to oscillations into mean kinetic energy, because of the non-harmonic character of the potential. A similar behavior has been observed recently in the Florence group, where rubidium atoms were held in a vertical optical lattice and the contrast between momentum states due to Bloch oscillations degraded after a few oscillations [181].

The lifetime of the atomic sample inside the elevator after transport over 10 cm is 10 s, which is equal to the value obtained when atoms are loaded in the elevator without motion.

6.6 Towards a measurement of the Casimir-Polder interaction

Surfaces. The surfaces installed under vacuum to be studied consist of gold deposited on mica, and graphite. Both samples satisfy the requirement of being good electrical conductors at the frequencies involved. From the study of quantum reflection, the 'reflection length' given by Eq. (3.35) characterizes the distance of closest approach to the surfaces. We estimated this distance to be $x_4 = 628$ nm for sodium atoms incident at $v_i = 1$ cm/sec. The reflectivity of gold is almost unity ($R \geq 0.98$) for wavelengths above 620 nm [182], while for graphite $R \geq 0.5$ in the range of infrared frequencies up to 1.2 eV (corresponding to $\lambda = 1\,\mu$m) [183].

The gold surface is of a 150 nm thick layer of Au(111) evaporated onto cleaved mica (Molecular Imaging). It has a size of 1.0×1.1 cm, and presents

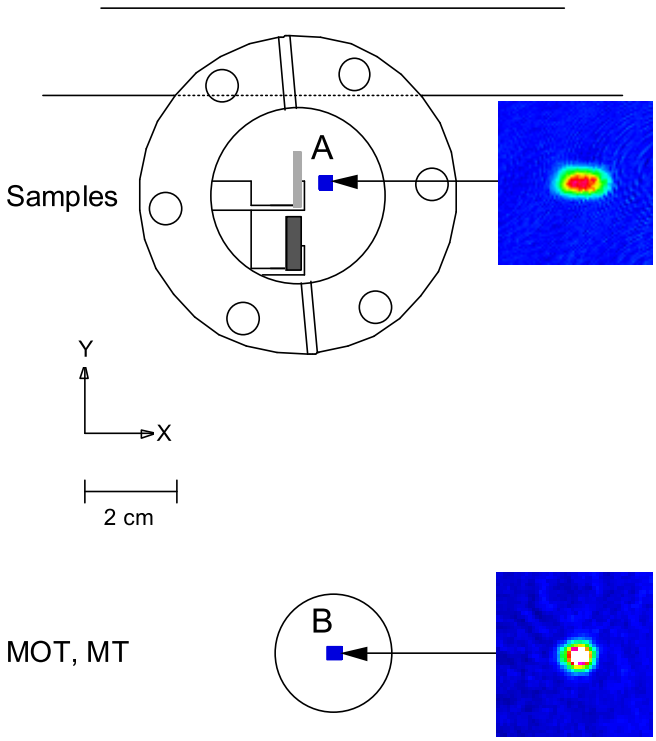

Figure 6.6: Atoms are transported over a distance of 10.4 cm by the optical elevator, from the magnetic trap center (MT) towards the surfaces. The initial number of atoms is 2.5×10^6, and 60% of them reach the top. At the end of transport the atomic cloud is 4.5 mm away from the upper sample. Further manipulation will decrease this distance prior to launching. Upon quantum reflection, atoms will be recaptured in a MOT and counted. The upper frame images atoms in the XY plane, while for the lower one a perpendicular plane to XY was used (see Fig. 4.6). Field of view is 1.28×1.92 mm and 1.47×1.47 mm for the upper and lower pictures, respectively.

atomically flat terraces measuring up to 500×500 nm^2, according to the manufacturer. The substrate was shipped to us in a nitrogen environment. We did not anneal the surface prior to placement under vacuum, and exposure to air was restricted to the time it took for mounting inside the chamber (2.5 hours). After that, it was baked along with the vacuum chamber at a temperature of 220 °C for several days (see Section 4.5).

Graphite was chosen because of its semi-metallic character, and also because it contains relatively big atomically flat areas (200×200 nm^2) [184]. We use Highly Ordered Pyrolytic Graphite (HOPG) (grade ZYA from Advanced Ceramics Corp.), which is routinely used to calibrate Scanning Tunneling Microscopy (STM) machines. Prior to mounting under vacuum, the sample was cleaved by using "scotch brand" double sided tape [184]. Carbon in the form of graphite consists of a layered structure, where the distance between two neighbor layers is 3.35 Å, and atoms in each layer are 1.42 Å from each other [185]. While atomic bonds inside a given plane are covalent, bonds between planes arise from weak van der Waals forces. This is why graphite is used as a lubricant, and explains why cleaving is simply done by removing an atomic layer with scotch tape.

Current status. The optical elevator allows us to place 1.5×10^6 atoms in front of the surfaces we want to study, 4.5 mm away from them. In order to observe quantum reflection, we require atomic samples with a velocity spread on the order of the smallest incident velocity we plan to use. We consider practical to have launch velocities as small as 3 mm/s, that is $v_{\rm r}/10$. As stated before, the elevator provides us with samples having $\bar{\sigma}_{\rm v} = 0.6\, v_{\rm r}$, and $\sigma_{\rm v}^{\rm T} = 0.4\, v_{\rm r}$ along the direction of incidence. It is therefore necessary to cool

the atomic sample further.

We plan to implement evaporative cooling in a pure optical potential. A small collision rate inside the optical elevator currently prevents evaporation. We can estimate the collision rate of the sample after elevation by noting its final size: $\sigma_{\rm x}^{\rm L} = 140\,\mu$m, and $\sigma_{\rm x}^{\rm T} = 130\,\mu$m. This implies a peak density of $n_0 = 4 \times 10^{10}$ cm^{-3}. Substitution of n_0 and $\langle v \rangle = 0.6\,v_{\rm r} = 1.8$ cm/s into Eq. (4.28) yields for the elastic collision rate: $\gamma = 0.12$ Hz. To increase this number we plan to transfer the atoms into another horizontal optical lattice, formed by the interference of two beams superimposed at an angle of $\theta = 4^{\rm o}$. The lattice beams will be created by using a beam splitter mounted on a monolithic structure. Such a configuration will eliminate residual vibrations, and the large lattice spacing (7.6 μm) will minimize the effects of Bloch oscillations. In order to increase the collision rate, a Nd:Yag beam will be tightly focused onto the atoms, providing trapping frequencies in the horizontal direction which we expect will yield the necessary collision rate for evaporative cooling.

We plan to perform the launching towards the surfaces by using the tightly focused Nd:Yag beam as an optical tweezers. Motion of the beam will be controlled by a mirror mounted on a closed-loop galvo, Fig. 6.1. After atoms are reflected, they will be recaptured in a MOT. The atom number can then be counted by measuring fluorescence, and compared with the incident number, obtained from a destructive measurement prior to the launching. This method for measuring the reflection probability clearly relies on small statistical fluctuations of the initial atom number, and averaging is needed. A signal to noise on the level of 1% or better is expected.

Bibliography

[1] M. C. Fischer, B. Gutiérrez-Medina, and M. G. Raizen, "Observation of the Quantum Zeno and Anti-Zeno effects in an unstable system," *Phys. Rev. Lett.* **87**, 040402 (2001).

[2] M. C. Fischer, A. M. Dudarev, B. Gutiérrez-Medina, and M. G. Raizen, "FM spectroscopy in recoil-induced resonances," *J. Opt. B: Quantum Semiclass. Opt.* **3**, 279 (2001).

[3] James Clerk Maxwell, *A Treatise on Electricity and Magnetism*, vol. 2 (Dover, New York, 1954), 3rd ed.

[4] E. Arimondo, W. D. Phillips, and F. Strumia, eds., *Laser Manipulation of Atoms and Ions* (North-Holland, Amsterdam, 1992).

[5] R. Graham, M. Schlautmann, and P. Zoller, "Dynamical localization of atomic-beam deflection by a modulated standing light wave," *Phys. Rev. A* **45**, R19 (1992).

[6] Kirk W. Madison, *Quantum transport in optical lattices*, Ph.D. thesis, The University of Texas at Austin (1998).

[7] U. Volz, M. Majerus, H. Liebel, A. Schmitt, and H. Schmoranzer, "Precision lifetime measurements on NaI $3p\,^2p_{1/2}$ and $3p\,^2p_{3/2}$ by beam-gas-laser spectroscopy," *Phys. Rev. Lett.* **76**, 2862 (1996).

[8] C. W. Oates, K. R. Vogel, and J. L. Hall, "High precision linewidth measurement of laser-cooled atoms: Resolution of the Na $3p\,^2p_{3/2}$ lifetime discrepancy," *Phys. Rev. Lett.* **76**, 2866 (1996).

[9] Rodney Loudon, *The Quantum Theory of Light* (Clarendon, Oxford, 1983), 2nd ed.

[10] Neil W. Ashcroft and N. David Mermin, *Solid State Physics* (Saunders College, Philadelphia, 1976).

[11] Mark Raizen, Qian Niu, and Christophe Salomon, "New light on quantum transport," *Physics Today* **50**, 30 (1997).

[12] M. Ben Dahan, E. Peik, J. Reichel, Y. Castin, and C. Salomon, "Bloch oscillations of atoms in an optical potential," *Phys. Rev. Lett.* **76**, 4508 (1996).

[13] S. R. Wilkinson, C. F. Bharucha, K. W. Madison, Q. Niu, and M. G. Raizen, "Observation of atomic Wannier-Stark ladders in an accelerating optical potential," *Phys. Rev. Lett.* **76**, 4512 (1996).

[14] Michael P. Marder, *Condensed Matter Physics* (Wiley-Interscience, New York, 2000).

[15] M. C. Fischer, *Atomic motion in otpical potentials*, Ph.D. thesis, The University of Texas at Austin (2001).

[16] Milton Abramowitz and Irene A. Stegun, eds., *Handbook of Mathematical Functions* (Dover, New York, 1965).

[17] Ekkehard Peik, Maxime Ben Dahan, Isabelle Bouchoule, Yvan Castin, and Christophe Salomon, "Bloch oscillations of atoms, adiabatic rapid passage, and monokinetic atomic beams," *Phys. Rev. A* **55**, 2989 (1997).

[18] Q. Niu, X. Zhao, G. A. Georgakis, and M. G. Raizen, "Atomic Landau-Zener tunneling and Wannier-Stark ladders in optical potentials," *Phys. Rev. Lett.* **76**, 4504 (1996).

[19] C. Zener, "A theory of the electrical breakdown of solid dielectrics," *Proc. R. Soc. London A* **145**, 523 (1934).

[20] C. Zener, "Non-adiabatic crossing of energy levels," *Proc. R. Soc. London A* **137**, 696 (1932).

[21] C. F. Bharucha, K. W. Madison, P. R. Morrow, S. R. Wilkinson, B. Sundaram, and M. G. Raizen, "Observation of atomic tunneling from an accelerating optical potential," *Phys. Rev. A* **55**, R857 (1997).

[22] K. W. Madison, C. F. Bharucha, P. R. Morrow, S. R. Wilkinson, Q. Niu, B. Sundaram, and M. G. Raizen, "Quantum transport of ultracold atoms in an accelerating optical potential," *Appl. Phys. B* **65**, 693 (1997).

[23] Eugen Merzbacher, *Quantum Mechanics* (Wiley, 1970), 2nd ed.

[24] J. J. Sakurai, *Modern Quantum Mechanics* (Addison Wesley, 1994), revised ed.

[25] L. A. Khalfin, "Contribution to the decay theory of a quasi-stationary state," *JETP* **6**, 1053 (1958).

[26] R. G. Winter, "Evolution of a quasi-stationary state," *Phys. Rev.* **123**, 1503 (1961).

[27] L. Fonda, G. C. Ghirardi, and A. Rimini, "Decay theory of unstable quantum systems," *Rep. Prog. Phys.* **41**, 587 (1978).

[28] P. T. Greenland and A. M. Lane, "Exposure of decay at non-constant rate by rapid fluctuations," *Phys. Lett. A* **117**, 181 (1986).

[29] Eric B. Norman, Stuart B. Gazes, Stephanie G. Crane, and Dianne A. Bennett, "Tests of the exponential decay law at short and long times," *Phys. Rev. Lett.* **60**, 2246 (1988).

[30] Q. Niu and M. G. Raizen, "How Landau-Zener tunneling takes time," *Phys. Rev. Lett.* **80**, 3491 (1998).

[31] S. R. Wilkinson, C. F. Bharucha, M. C. Fischer, K. W. Madison, P. R. Morrow, Q. Niu, B. Sundaram, and M. G. Raizen, "Experimental evidence for non-exponential decay in quantum tunnelling," *Nature* **387**, 575 (1997).

[32] B. Misra and E. C. G. Sudarshan, "The Zeno's paradox in quantum theory," *J. Math. Phys.* **18**, 756 (1977).

[33] C. B. Chiu, E. C. G. Sudarshan, and B. Misra, "Time evolution of unstable quantum states and a resolution of Zeno's paradox," *Phys. Rev. D* **16**, 520 (1977).

[34] W. C. Schieve, L. P. Horwitz, and J. Levitan, "Numerical study of Zeno and Anti-Zeno effects in a local potential model," *Phys. Lett. A* **136**, 264 (1989).

[35] A. G. Kofman and G. Kurizki, "Acceleration of quantum decay processes by frequent observations," *Nature* **405**, 546 (2000).

[36] P. Facchi, H. Nakazato, and S. Pascazio, "From the Quantum Zeno to the Inverse Quantum Zeno effect," *Phys. Rev. Lett.* **86**, 2699 (2001).

[37] K. Grotz and H. V. Klapdor, "Time scale of short time deviations from exponential decay," *Phys. Rev. C* **30**, 2098 (1984).

[38] W. M. Itano, D. J. Heinzen, J. J. Bollinger, and D. J. Wineland, "Quantum Zeno effect," *Phys. Rev. A* **41**, 2295 (1990).

[39] P. Kwiat, H. Weinfurter, T. Herzog, A. Zeilinger, and M. A. Kasevich, "Interaction-free measurement," *Phys. Rev. Lett.* **74**, 4763 (1995).

[40] C. V. Raman and S. Bhagavantam, "Experimental proof of the spin of the photon," *Nature* **129**, 22 (1932).

[41] Richard A. Beth, "Mechanical detection and measurement of the angular momentum of light," *Phys. Rev.* **50**, 115 (1936).

[42] S. Chu, L. Hollberg, J. Bjorkholm, A. Cable, and A. Ashkin, "Three-dimensional viscous confinement and cooling of atoms by resonance radiation pressure," *Phys. Rev. Lett.* **55**, 48 (1985).

[43] Harold J. Metcalf and Peter van der Straten, *Laser Cooling and Trapping*, Graduate Texts in Contemporary Physics (Springer, New York, 1999).

[44] J. Dalibard and C. Cohen-Tannoudji, "Laser cooling below the Doppler limit by polarization gradients: simple theoretical models," *J. Opt. Soc. Am. B* **6**, 2023 (1989).

[45] C. N. Cohen-Tannoudji, "Nobel lecture. Manipulating atoms with photons," *Rev. Mod. Phys.* **70**, 707 (1998).

[46] S. Chu, "Nobel lecture. The manipulation of neutral particles," *Rev. Mod. Phys.* **70**, 685 (1998).

[47] W. D. Phillips, "Nobel lecture. Laser cooling and trapping of neutral atoms," *Rev. Mod. Phys.* **70**, 721 (1998).

[48] A. Migdall, J. Prodan, W. Phillips, T. Bergeman, and H. Metcalf, "High densities of cold atoms in a dark spontaneous–force optical trap," *Phys. Rev. Lett.* **54**, 2596 (1985).

[49] E. L. Raab, M. Prentiss, Alex Cable, Steven Chu, and D. E. Pritchard, "Trapping of neutral sodium atoms with radiation pressure," *Phys. Rev. Lett.* **59**, 2631 (1987).

[50] J. R. Robinson, *Atom optics: A new testing ground for quantum chaos*, Ph.D. thesis, The University of Texas at Austin (1995).

[51] Braulio Gutiérrez Medina, Martin C. Fischer, and Mark G. Raizen, "Observation of the quantum Zeno and Anti-Zeno effects in an unstable system," in *Proceedings of the XXII Solvay Conference in Physics. The Physics of Communication*, I. Antoniou, V. A. Sadovnichy, and H. Walter, eds. (World Scientific, Singapore, 2003).

[52] C. J. Myatt, *Bose-Einstein condensation experiments in a dilute vapor of rubidium*, Ph.D. thesis, University of Colorado (1997).

[53] Wolfgang Ketterle, Kendall B. Davis, Michael A. Joffe, Alex Martin, and David E. Pritchard, "High densities of cold atoms in a dark spontaneous-force optical trap," *Phys. Rev. Lett.* **70**, 2253 (1993).

[54] M. Prentiss, A. Cable, J. E. Bjorkhlom, Steven Chu, E. L. Raab, and D. E. Pritchard, "Atomic-density-dependent losses in an optical trap," *Optics Letters* **13**, 452 (1988).

[55] A. Kastberg, W. D. Phillips, S. L. Rolston, R. J. C. Spreeuw, and P. S. Jessen, "Adiabatic cooling of cesium to 700 nK in an optical lattice," *Phys. Rev. Lett.* **74**, 1542 (1995).

[56] Steffen Wolf, Steven J. Oliver, and David S. Weiss, "Supression of recoil heating by an optical lattice," *Phys. Rev. Lett.* **85**, 04249 (2000).

[57] Daniel A. Steck, *Quantum chaos, transport, and decoherence in atom optics*, Ph.D. thesis, The University of Texas at Austin (2001).

[58] Erling Riis, David S. Weiss, Kathryn A. Moler, and Steven Chu, "Atom funnel for the production of a slow, high-density atomic beam," *Phys. Rev. Lett.* **64**, 1658 (1990).

[59] M. Walhout, J. Dalibard, S. L. Rolston, and W. D. Phillips, "σ^+-σ^- optical molasses in a longitudinal magnetic field," *J. Opt. Soc. A* **9**, 1997 (1992).

[60] Kihwan Kim, Heung-Ryoul Noh, Young-Hee Yeon, V. G. Minogin, and Wonho Jhe, "Cold rubidium atomic beam produced by Zeeman-imbalanced radiation pressures," *Phys. Rev. A* **65**, 055404 (2002).

[61] W. Wholleben, F. Chevy, K. W. Madison, and J. Dalibard, "An atom faucet," *The European Physical Journal D* **15**, 237 (2001).

[62] C. J. Myatt, N. R. Newbury, R.W. Ghirst, S. Loutzenhiser, and C. E. Wieman, "Multiply loaded magneto-optical trap," *Opt. Lett.* **21**, 290 (1996).

[63] D. van der Waals, "Die Kontinuität des gasförmigenund flüssigen Zustandes," (Amsterdam, 1881).

[64] H. Margenau, "Van der Waals forces," *Rev. Mod. Phys.* **11**, 1 (1939).

[65] J. D. Jackson, *Classical Electrodynamics* (Wiley, 1975), 2nd ed.

[66] L. Pauling and E. B. Wilson Jr., *Introduction to Quantum Mechanics* (McGraw-Hill, New York, 1935).

[67] B. H. Brandsen and C. H. Joachain, *Physics of Atoms and Molecules* (Longman, Essex, 1983).

[68] R. Eisenschitz and F. London*Zeits. f. Physik* **60**, 491 (1930).

[69] F. London*Zeits. f. Physik* **63**, 245 (1930).

[70] F. London*Zeits. f. physik. Chemie (B)* **11**, 222 (1930).

[71] H. B. G. Casimir, "On the attraction of two perfectly conducting plates," *Proc. Kon. Ned. Akad. Wetenschap* **51**, 793 (1948).

[72] Barry R. Holstein, "The van der Waals interaction," *Am. J. Phys.* **64**, 441 (2001).

[73] Ludwig Bergmann and Clemens Schaefer, *Constituents of Matter* (Walter de Gruyter, Berlin, 1997).

[74] J. E. Lennard-Jones *Trans. Faraday Soc.* **28**, 334 (1932).

[75] H. Margenau and W. G. Pollard, "The forces between neutral molecules and metallic surfaces," *Phys. Rev.* **60**, 128 (1941).

[76] J. Bardeen, "The image and van der Waals forces at a metallic surface," *Phys. Rev.* **58**, 727 (1940).

[77] A. Dalgarno and W. D. Davidson, *Adv. At. Mol. Phys.*, vol. 2 (1966).

[78] A. Derevianko, W. R. Johnson, M. S. Safronova, and J. F. Babb, "High-precision calculations of dispersion coefficients, static dipole polarizabilities, and atom-wall interaction constants for alkali-metal atoms," *Phys. Rev. Lett.* 3589 (1999).

[79] P. Kharchenko, J. F.Babb, and A. Dalgarno, "Long-range interactions of sodium atoms," *Phys. Rev. A* **55**, 3566 (1997).

[80] B. Segev, R. Côté, and M. G. Raizen, "Quantum reflection from an atomic mirror," *Phys. Rev. A* **56**, R3350 (1997).

[81] Arthur W. Adamson, *Physical Chemistry of Surfaces* (Wiley, 1982), 4th ed.

[82] Andrew Zangwill, *Physics at Surfaces* (Cambridge University Press, Cambridge, 1988).

[83] H. B. G. Casimir and D. Polder, "The influence of retardation on the London-van der Waals forces," *Phys. Rev.* **73**, 360 (1948).

[84] S.K. Lamoreaux, "Resource letter CF-1: Casimir force," *Am. J. Phys.* **67**, 850 (1999).

[85] S.K. Lamoreaux, "Demonstration of the Casimir force in the 0.6 to 6 μm range," *Phys. Rev. Lett.* **78**, 5 (1997).

[86] S.K. Lamoreaux, "Erratum: Demonstration of the Casimir force in the 0.6 to 6 μm range [Phys. Rev. Lett. 78, 5 (1997)]," *Phys. Rev. Lett.* **81**, 5475 (1998).

[87] M. Marinescu, A. Dalgarno, and J. F. Babb, "Retarded long-range potentials for the alkali-metal atoms and a perfectly conducting wall," *Phys. Rev. A* **55**, 1530 (1997).

[88] C. R. Ekstrom, J. Schmiedmayer, M. S. Chapman, T. D. Hammond, and D. E. Pritchard, "Measurement of the electric polarizability of sodium with an atom interferometer," *Phys. Rev. A* **51**, 3883 (1995).

[89] Alain Aspect and Jean Dalibard, "Measurement of the atom-wall interaction: from London to Casimir–Polder," *Séminaire Poincaré* **1**, 67 (2002).

[90] S. Haroche, *Fundamental systems in quantum optics*, Les Houches LIII (Amsterdam, 1992).

[91] Claude Cohen-Tannoudji, Jacques Dupont-Roc, and Gilbert Grynberg, *Atom–Photon Interactions*, Science Paperback (Wiley, 1998).

[92] D. Meschede, W. Jhe, and E. A. Hinds, "Radiative properties of atoms near a conducting plane: An old problem in a new light," *Phys. Rev. A* **41**, 1587 (1990).

[93] F. Shimizu, "Specular reflection of very slow metastable neon atoms from a solid surface," *Phys. Rev. Lett.* **86**, 987 (2001).

[94] D. O. Edwards, P. Fatouros, G. G. Ihas, P. Mrozinski, S. Y. Shen, F. M. Gasparini, , and C. P. Tam, "Specular reflection of ^{4}He atoms from the surface of liquid ^{4}He," *Phys. Rev. Lett.* **34**, 1153 (1975).

[95] V. U. Nayak, D. O. Edwards, and N. Masuhara, "Scattering of ^{4}He atoms grazing the liquid-^{4}He surface," *Phys. Rev. Lett.* **50**, 990 (1983).

[96] J. J. Berkhout, O. J. Luiten, I. D. Setija, T. W. Hijmans, T. Mizusaki, and J. T. M. Walraven, "Quantum reflection: Focusing of hydrogen atoms with a concave mirror," *Phys. Rev. Lett.* **63**, 1689 (1989).

[97] I. A. Yu, J. M. Doyle, J. C. Sandberg, C. L. Cesar, D. Kleppner, and T. J. Greytak, "Evidence for universal quantum reflection of hydrogen from liquid ^{4}He," *Phys. Rev. Lett.* **71**, 1589 (1993).

[98] A. Anderson, S. Haroche, E. A. Hinds, W. Jhe, D. Meschede, and L. Moi, "Reflection of thermal Cs atoms grazing a polished glass surface," *Phys. Rev. A* **34**, 3513 (1986).

[99] V. Sandoghdar, C. I. Sukenik, E. A. Hinds, and S. Haroche, "Direct measurement of the van der Waals interaction between an atom and its images in a micron-sized cavity," *Phys. Rev. Lett.* **68**, 3432 (1992).

[100] C. I. Sukenik, M. G. Boshier, D. Cho, V. Sandoghdar, and E. A. Hinds, "Measurement of the Casimir–Polder force," *Phys. Rev. Lett.* **70**, 560 (1993).

[101] Mark Kasevich, Kathryn Moler, Erling Riis, Elizabeth Sunderman, David Weiss, and Steven Chu, *Atomic Physics*, vol. 12 (AIP, New York, 1991).

[102] A. Landragin, J.-Y. Courtois, G. Labeyrie, N. Vansteenkiste, C. I. Westbrook, and A. Aspect, "Measurement of the van der Waals force in an atomic mirror," *Phys. Rev. Lett.* **77**, 1464 (1996).

[103] J.M. McGuirk, D.M. Harber, J.M. Obrecht, and E.A. Cornell, "Alkali adsorbate polarization on conducting and insulating surfaces probed with Bose-Einstein condensates," *Phys. Rev. A* **69**, 062905 (2004).

[104] Fujio Shimizu and Jun ichi Fujita, "Giant quantum reflection of neon atoms from a ridged silicon surface," *J. Phys. Soc. Jpn.* **71**, 5 (2002).

[105] Fujio Shimizu and Jun ichi Fujita, "Reflection-Type hologram for atoms," *Phys. Rev. Lett.* **88**, 123201 (2002).

[106] Hilmar Oberst, Shigenori Kasashima, Victor I. Balykin, and Fujio Shimizu, "Atomic-matter-wave scanner," *Phys. Rev. A* **68**, 013606 (2003).

[107] V. Druzhinina and M. DeKieviet, "Experimental observation of quantum reflection far from threshold," *Phys. Rev. Lett.* **91**, 193202 (2003).

[108] Thomas A. Pasquini, Yong-Il Shin, Christian Sanner, Michele Saba, Andre Schirotzek, David E. Pritchard, and Wolfgang Ketterle, "Quantum reflection of atoms from a solid surface at normal incidence," *cond-mat/0405530* (2004).

[109] H. Friedrich, G. Jacoby, and C. G. Meister, "Quantum reflection by Casimirvan der Waals potential tails," *Phys. Rev. A* **65**, 032902 (2002).

[110] R. Côté, H. Friedrich, and J. Trost, "Reflection above potential steps," *Phys. Rev. A* **56**, 1781 (1997).

[111] A. Derevianko, W. R. Johnson, and Stephan Fritzsche, "Many-body calculations of the static atom-wall interaction potential for alkali-metal atoms," *Phys. Rev. A* 2629 (1998).

[112] W. H. Press, S. A. Teukolsky, W. T. Vetterling, and B. P. Flannery, *Numerical Recipies in C* (Cambridge University Press, Cambridge, 1992).

[113] H. Schlichting, D. Menzel, T. Brunner, W. Brenig, and J. C. Tully, "Quantum effects in the sticking of Ne on a flat metal surface," *Phys. Rev. Lett.* **60**, 2515 (1988).

[114] E. G. Lima, M. Chevrollier, O. Di Lorenzo, P. C. Segundo, and M. Oriá, "Long-range atom-surface bound states," *Phys. Rev. A* **62**, 013410 (2000).

[115] Lene Vestergaard Hau, J. A. Golovchenko, and Michael M. Burns, "A new atomic beam source: The "Candlestick"," *Rev. Sc. Inst.* **65**, 3746 (1994).

[116] Florian Schreck, *Mixtures of ultracold gases*, Ph.D. thesis, École Normale Supérieure (2002).

[117] C. B. Alcock, *CRC Handbook of Chemistry and Physics. Vapor pressure of the metallic elements* (CRC Press, Boca Raton, 2003), 84th ed.

[118] J. Prodan, W. Phillips, and H. Metcalf, "Laser production of a very slow monoenergetic atomic beam," *Phys. Rev. Lett.* **49**, 1149 (1982).

[119] J. Prodan and W. Phillips, "Chirping the light fantastic: Recent NBS Atomic cooling experiments," *Prog. Quant. Elect.* **8**, 231 (1984).

[120] R. Gaggl, L. Windholz, C. Umfer, , and C. Neureiter, "Laser cooling of a sodium atomic beam using the Stark effect," *Phys. Rev. A* **49**, 1119 (1994).

[121] Brian David Busch, *Bose–Einstein condensation and atomic interactions in a sodium gas*, Ph.D. thesis, Harvard University (2000).

[122] Dallin S. Durfee, *Dynam properties of dilute Bose–Einstein condensates*, Ph.D. thesis, Massachusetts Institute of Technology (1999).

[123] Artur Widera, *Design and construction of a modular Spin-Flip Zeeman slower*, Master's thesis, The University of Texas at Austin (2001).

[124] Zhu M., Oates C. W., and Hall J. L., "Continuous high–flux monovelocity atomic beam based on a broadband laser–cooling technique," *Phys. Rev. Lett.* **67**, 46 (1991).

[125] Kenji Odaka and Shinjiro Ueda, "Outgassing reduction of type 304 stainless steel by surface oxidation in air," *J. Vac. Sci. Technol. A* **13**, 520 (1995).

[126] B. P. Anderson and M. A. Kasevich, "Enhanced loading of a magneto-optic trap from an atomic beam," *Phys. Rev. A* **50**, R3581 (1994).

[127] Shin Inouye, *Manipulating Bose-Einstein condensates with laser light*, Ph.D. thesis, Massachusetts Institute of Technology (2001).

[128] M. H. Anderson, W. Petrich, J. R. Ensher, and E. A. Cornell, "Reduction of light-assisted collisional loss rate from a low-pressure vapor-cell trap," *Phys. Rev. A* **50**, R3597 (1994).

[129] Mark Kasevich and Steven Chu, "Laser cooling below a photon recoil with three-level atoms," *Phys. Rev. Lett.* **69**, 1741 (1992).

[130] J. Lawall, S. Kulin, B. Saubamea, N. Bigelow, M. Leduc, and C. Cohen-Tannoudji, "Three-Dimensional laser cooling of helium beyond the single-photon recoil limit," *Phys. Rev. Lett.* **75**, 4194 (1995).

[131] J. D. Miller, R. A. Cline, and D. J. Heinzen, "Far-off-resonance optical trapping of atoms," *Phys. Rev. A* **47**, R4567 (1993).

[132] M. D. Barrett, J. A. Sauer, and M. S. Chapman, "All–Optical formation of an atomic Bose–Einstein condensate," *Phys. Rev. Lett.* **87**, 010404 (2001).

[133] W. H. Wing, "On neutral particle trapping in quasistatic electromagnetic fields," *Prog. Quant. Elect.* **8**, 181 (1984).

[134] Z. Hadzibabic, S. Gupta, C. A. Stan, C. H. Schunck, M. W. Zwierlein, K. Dieckmann, and W. Ketterle, "Fifty–fold improvement in the number of quantum degenerate fermionic atoms," *Phys. Rev. Lett.* **91**, 160401 (2003).

[135] Kendall B. Davis, Marc-Oliver Mewes, Michael A. Joffe, Michael R. Andrews, and Wolfgang Ketterle, "Evaporative cooling of sodium atoms," *Phys. Rev. Lett.* **74**, 5202 (1995).

[136] D. S. Naik and C. Raman, "An optically plugged quadrupole trap for Bose-Einstein condensates," *cond-mat/0406341* (2004).

[137] Anderson M. H., Ensher J. R., Matthews M. R., Wieman C. E., and Cornell E. A., "Observation of Bose–Einstein condensation in a dilute atomic vapor," *Science* **269**, 198 (1995).

[138] M.-O. Mewes, M.R. Andrews, N.J. van Druten, D.M. Kurn, D.S. Durfee, and W. Ketterle, "Bose–Einstein condensation in a tightly confining dc magnetic trap," *Phys. Rev. Lett.* **77**, 416 (1996).

[139] David E. Pritchard, "Cooling neutral atoms in a magnetic trap for precision spectroscopy," *Phys. Rev. Lett.* **51**, 1336 (1983).

[140] W. Ketterle, D. S. Durfee, and D. M. Stamper-Kurn, *Proceedings of the International School of Physics "Enrico Fermi"*, vol. CXL, 176 (Italian Physical Society, Bologna, 1999).

[141] Ananth P. Chikkatur, *Colliding and moving Bose-Einstein condensates: a study of superfluidity and optical tweezers for condensate transport*, Ph.D. thesis, Massachusetts Institute of Technology (2002).

[142] Dan M. Stamper-Kurn, *Peeking and poking at a new quantum fluid: Studies of gaseous Bose-Einstein condensates in magnetic and optical traps*, Ph.D. thesis, Massachusetts Institute of Technology (2000).

[143] Changhyun Ryu, *Photoassociation experiments on ultracold and quantum gases in optical lattices*, Ph.D. thesis, The University of Texas at Austin (2004).

[144] John M. Doyle, Jon C. Sandberg, Daniel Kleppner, Thomas J. Greytak, Harald F. Hess, and Greg P. Kochanski, "Evaporative cooling of spin–polarized atomic hydrogen," *Phys. Rev. Lett.* **61**, 935 (1988).

[145] Charles S. Adams, Heun Jin Lee, Nir Davidson, Mark Kasevich, and Steven Chu, "Evaporative cooling in a crossed dipole trap," *Phys. Rev. Lett.* **74**, 3577 (1995).

[146] D.M. Harber, J.M. McGuirk, J.M. Obrecht, and E.A. Cornell, "Thermally induced losses in ultra–cold atoms magnetically trapped near room–temperature surfaces," *J. Low Temp. Phys.* **133**, 229 (2003).

[147] W. Ketterle and N. J. van Druten, *Advances in Atomic, Molecular and Optical Physics*, no. 36 (Academic Press, San Diego, 1996).

[148] Huang Wu and Christopher J. Foot, "Direct simulation of evaporative cooling," *J. Phys. B: At. Mol. Opt. Phys.* **29**, L321 (1996).

[149] O. J. Luiten, M. W. Reynolds, and J. T. M. Walraven, "Kinetic theory of the evaporative cooling of a trapped gas," *Phys. Rev. A* **53**, 381 (1997).

[150] C. A. Sackett, C. C. Bradley, and R. G. Hulet, "Optimization of evaporative cooling," *Phys. Rev. A* **55**, 3797 (1997).

[151] D.W. Snoke and J.P. Wolfe, "Optimization of evaporative cooling," *Phys. Rev. B* **39**, 4030 (1989).

[152] Eite Tiesinga, Carl J. Williams, Paul S. Julienne, Kevin M. Jones, Paul D. Lett, and William D. Phillips, "A spectroscopic determination of scattering lengths for sodium atom collisions," *J. Res. Natl. Inst. Stand. Technol.* **101**, 505 (1996).

[153] E. A. Cornell and C. E. Wieman, "Nobel lecture. Bose–Einstein condensation in a dilute gas, the first 70 years and some recent experiments," *Rev. Mod. Phys.* **74**, 875 (2002).

[154] W. Ketterle, "Nobel lecture. When atoms behave as waves: Bose–Einstein condensation and the atom laser," *Rev. Mod. Phys.* **74**, 1131 (2002).

[155] F. Dalfovo, S. Giorgini, L. P. Pitaevskii, and S. Stringari, "Theory of Bose–Einstein condensation in trapped gases," *Rev. Mod. Phys.* **71**, 463 (1999).

[156] A. J. Leggett, "Bose–Einstein condensation in the alkali gases: Some fundamental concepts," *Rev. Mod. Phys.* **73**, 307 (2001).

[157] S. N. Bose, "Planck's law and the hypothesis of light quanta," *Z. Phys.* **26**, 178 (1924).

[158] A. Einstein*Sitzber. Kgl. Preuss. Akad. Wiss.* 261 (1924).

[159] A. Einstein*Sitzber. Kgl. Preuss. Akad. Wiss.* 3 (1925).

[160] Kerson Huang, *Statistical Mechanics* (Wiley, 1987), 2nd ed.

[161] Dale G. Fried, Thomas C. Killian, Lorenz Willmann, David Landhuis, Stephen C. Moss, Daniel Kleppner, and Thomas J. Greytak, "Bose–

Einstein condensation of atomic hydrogen," *Phys. Rev. Lett.* **81**, 3811 (1998).

[162] C. C. Bradley, C. A. Sackett, J. J. Tollett, and R. G. Hulet, "Evidence of Bose–Einstein condensation in an atomic gas with attractive interactions," *Phys. Rev. Lett.* **75**, 1687 (1995).

[163] L. Vestergaard Hau, B. D. Busch, C. Liu, Z. Dutton, M. M. Burns, and J. A. Golovchenko, "Near–resonant spatial images of confined Bose–Einstein condensates in a 4–Dee magnetic bottle," *Phys. Rev. A* **58**, R54 (1998).

[164] M. Kozuma, L. Deng, E. W. Hagley, J. Wen, R. Lutwak, K. Helmerson, S. L. Rolston, and W. D. Phillips, "Coherent splitting of Bose–Einstein condensed atoms with optically induced Bragg diffraction," *Phys. Rev. Lett.* **82**, 871 (1999).

[165] Florian Schreck and Todd Meyrath, "A laboratory control system for cold atom experiments: Hardware and software," (2004). http://george.ph.utexas.edu/~control/.

[166] F. Chevy, V. Bretin, P. Rosenbusch, K. W. Madison, and J. Dalibard, "Transverse breathing mode of an elongated Bose–Einstein condensate," *Phys. Rev. Lett.* **88**, 250402 (2002).

[167] V. Bagnato, D. E. Pritchard, and D. Kleppner, "Bose–Einstein condensation in an external potential," *Phys. Rev. A* **35**, 4354 (1987).

[168] C. J. Pethick and H. Smith, *Bose–Einstein condensation in dilute gases* (Cambridge University Press, Cambridge, 2002).

[169] Y. Castin and R. Dum, "Bose–Einstein condensates in time dependent traps," *Phys. Rev. Lett.* **77**, 5315 (1996).

[170] A. E. Leanhardt, T. A. Pasquini, M. Saba, A. Schirotzek, Y. Shin, D. Kielpinski, D. E. Pritchard, and W. Ketterle, "Adiabatic and evaporative cooling of Bose–Einstein condensates below 500 Picokelvin," *Science* **301**, 1513 (2003).

[171] S. Inouye, A. P. Chikkatur, D. M. Stamper-Kurn, J. Stenger, D. E. Pritchard, and W. Ketterle, "Superradiant Rayleigh scattering from a Bose-Einstein condensate," *Science* **285**, 571 (1999).

[172] Thomas M. Miller, *CRC Handbook of Chemistry and Physics. Atomic and molecular polarizabilities* (CRC Press, Boca Raton, 2003), 84th ed.

[173] Rudolf Grimm, Matthias Weidemller, and Yurii B. Ovchinnikov, *Advances in Atomic, Molecular and Optical Physics*, vol. 42 (2000).

[174] K. L. Corwin, S. J. M. Kuppens, D. Cho, and C. E. Wieman, "Spin-Polarized atoms in a circularly polarized optical dipole trap," *Phys. Rev. Lett.* **83**, 1311 (1999).

[175] D. Rychtarik, B. Engeser, H.-C. Nägerl, and R. Grimm, "Two-dimensional Bose-Einstein condensate in an optical surface trap," *Phys. Rev. Lett.* **92**, 173003 (2004).

[176] V. Milner, J. L. Hanssen, W. C. Campbell, and M. G. Raizen, "Optical billiards for atoms," *Phys. Rev. Lett.* **86**, 1514 (2001).

[177] Dominik Schrader, Stefan Kuhr, Wolfgang Alt, Martin Mueller, Victor Gomer, and Dieter Meschede, "An optical conveyor belt for single neutral atoms," *Appl. Phys. B* **73**, 819 (2001).

[178] O. Morsch, M. Cristiani, J. H. Mller, D. Ciampini, and E. Arimondo, "Free expansion of a Bose-Einstein condensate in a one-dimensional optical lattice," *Phys. Rev. A* **66**, 021601 (2002).

[179] O. Morsch, J. H. Mller, M. Cristiani, D. Ciampini, and E. Arimondo, "Bloch oscillations and mean-field effects of Bose-Einstein condensates in 1D optical lattices," *Phys. Rev. Lett.* **87**, 140402 (2001).

[180] B. P. Anderson and M. A. Kasevich, "Macroscopic quantum interference from atomic tunnel arrays," *Science* **282**, 1686 (1998).

[181] G. Roati, E. de Mirandes, H. Ott F. Ferlaino, G. Modugno, and M. Inguscio, "Atom interferometry with trapped Fermi gases," *Phys. Rev. Lett.* **92**, 230402 (2004).

[182] J. H. Weaver and H. P. R. Frederikse, *CRC Handbook of Chemistry and Physics. Optical properties of selected elements* (CRC Press, Boca Raton, 2003), 84th ed.

[183] G. Bellodi, A. Borghesi, L. Nosenzo G. Guizzetti, E. Reguzzoni, and G. Samoggia, "Analysis of infrared optical transitions in graphite," *Phys. Rev. B.* **12**, 5951 (1975).

[184] SPI, "Highly Ordered Pyrolytic Graphite," (2004). http://www.2spi.com.

[185] N. B. Brandt, S. M. Chudinov, and Ya. G. Ponomarev, *Semimetals 1. Graphite and its compounds* (North–Holland, Amsterdam, 1988).

Vita

Braulio Gutiérrez Medina was born on March 26, 1974 to Francisca Medina Ramírez and Joel Gutiérrez Plata in Mexico City, Mexico. After graduating from Colegio de Ciencias y Humanidades Azcapotzalco in 1993, he started studying physics at the National Autonomous University of Mexico (UNAM). He obtained his Bachelor's degree in 1997, and that same year he entered the Graduate School at The University of Texas at Austin. In the summer of 1998 he joined the group of Mark G. Raizen, where he began working on the investigations presented in this dissertation.

Permanent address: Física # 66 P. B. Col. El Rosario C.P. 02100
Del. Azcapotzalco. México, D. F. Mexico

This dissertation was typeset with LaTeX[†] by the author.

[†]LaTeX is a document preparation system developed by Leslie Lamport as a special version of Donald Knuth's TeX Program.